Structural Insights into the Regulation of Retinal Guanylyl Cyclase by Retinal Degeneration 3 (RD3) Protein and Guanylyl Cyclase Activating Protein 5 (GCAP5)

By

DIANA LEIGH CUDIA

DISSERTATION

Submitted in partial satisfaction of the requirements for the degree of

DOCTOR OF PHILOSOPHY

in

Chemistry

in the

OFFICE OF GRADUATE STUDIES

of the

UNIVERSITY OF CALIFORNIA

DAVIS

Approved:

_____

Dr. James B. Ames, Chair

_____

Dr. Andrew J. Fisher

_____

Dr. David B. Goodin

Committee in Charge

2021

ABSTRACT

Ca^{2+}-dependent regulation of retinal guanylyl cyclase (RetGC), controlled by the sensor proteins GCAP5 and RD3, is important for promoting the visual recovery phase of phototransduction in retinal photoreceptor cells. Particular point mutations in either RetGC, GCAPs or RD3 each disrupt the Ca^{2+}-dependent cyclase activity and are genetically linked to various retinal degenerative diseases, including autosomal cone dystrophy and Leber's congenital amaurosis. In this thesis, I will present atomic-level structural analyses of both GCAP5 and RD3. Before solving the structure of RD3, I first developed an elaborate procedure to prepare enough RD3 protein required for NMR that involved refolding functional protein from inclusion bodies. The NMR structure of the RD3 protein (described in Chapter 2) reveals a novel fold with a non-canonical 4-helix bundle, which identified key amino acid residues on the RD3 surface that make intermolecular contacts with RetGC. Mutation of these hot spot residues weaken RD3 binding to RetGC. This work on the RD3 protein was published in J. Biol. Chem (2019) 294:2318. In a separate project described in Chapter 3, I used both NMR and EPR-DEER to solve the dimeric structure of GCAP5, which provides insights into the Ca^{2+}/Fe^{2+}-dependent conformational changes in GCAP5 that control the activation of RetGC. GCAP5 contains two non-conserved cysteine residues (Cys15 and Cys17) that are essential for the binding of Fe^{2+} to GCAP5 that are not observed in GCAP1. In vivo functional studies show that Fe^{2+} binding to GCAP5 inhibits RetGC activity and GCAP5 is suggested to be a redox sensor in visual phototransduction. Binding and mutagenesis studies reveal that GCAP5 forms a dimer, which binds to a single Fe^{2+}. In essence, a total of four sulfhydryl groups (from Cys15 and Cys17) from each molecule of the GCAP5 dimer chelate the bound Fe^{2+} with a tetrahedral geometry, and the bound Fe^{2+} bridges two molecules of GCAP5 in a 1:2 complex. I solved the NMR structure of the Fe^{2+}-free activator state of GCAP5,

which is like the structure of GCAP1 except for differences in the N-terminal region that binds to Fe^{2+} in GCAP5. The N-terminal helix in GCAP5 is one turn longer to stabilize the exposure of Cys15 and Cys17, which are both essential for Fe^{2+} binding in GCAP5. I used EPR-DEER to measure intermolecular distances in the Fe^{2+}-free GCAP5 dimer that were used to elucidate the dimeric structure. The GCAP5 dimer interface is comprised of mostly hydrophobic residues (H18, Y21, M25, F72, V76 and W93) that are conserved in GCAP1. In addition, the GCAP5 dimer contains an intermolecular salt bridge (between R22 and D71) that is not conserved in GCAP1. The double mutation H18E/Y21E and single mutations (R22D and M25E) both disrupt GCAP5 dimerization and the corresponding mutations in GCAP1 each abolish cyclase activation. Also, a mutation in GCAP1 (H19E) was found in a human patient that has autosomal dominant cone dystrophy. I conclude that Fe^{2+} binding and dimerization of GCAP5 is critical for the regulation of RetGC and the residues identified at the dimer interface (H18, Y21, M25, F72, V76 and W93) are important targets for future drug design.

Abbreviations

GPCR	G-Protein Coupled-Receptor
PDE6	Phosphodiesterase-6
RetGC	Retinal membrane guanylyl cyclase
GDP	Guanosine Diphosphate
GTP	Guanosine Triphosphate
cGMP	Cyclic Guanosine Monophosphate
CNG	Cyclic Nucleotide-Gated Ion Channels
GCAPs	Guanylyl Cyclase Activating Proteins
NCS	Neuronal Calcium Sensor Proteins
CaM	Calmodulin
NMR	Nuclear Magnetic Resonance
DSC	Differential Scanning Calorimetry
RD3	Retinal Degeneration-3 Protein
LCA	Leber's Congenital Amaurosis
ER	Endoplasmic Reticulum
CORD6	Cone-Rod Dystrophy type 6
EPR-DEER	Electron Paramagnetic Resonance Double Electron-Electron Resonance
RD3-d	Deletion construct RD3 (residues 18-160)
PCR	Polymerase Chain Reaction
LB	Luria Broth
M9	Minimal 9 Media
IPTG	Isopropyl-1-β-D-1-thiogalactopyranoside
EDTA	Ethylenediaminetetraacetic Acid
BME	2-Mercaptoethanol
DTT	Dithiothreitol
TCI	Triple Resonance Cryogenic Probe
TEM buffer	10 mM Tris-HCl (pH 7.5), 0.1 mM EDTA and 14 mM BME
FPLC	Fast Protein Liquid Chromatography
SDS-PAGE	Sodium Dodecyl Sulfate Polyacrylamide Gel Electrophoresis
HIC	Hydrophobic Interaction Column
IEC	Ion Exchange Column
SEC	Size Exclusion Column
HSQC	Heteronuclear Single Quantum Correlation
RMSD	Root-Mean-Square Deviation'
zGCs	Zebrafish Guanylyl Cyclase
zGCAP1-5	Zebrafish Guanylyl Cyclase Activating Protein 1-5
WT	Wild-type
NMT	*N*-myristoyl CoA Transferase
AMD	Age-related Macular Degeneration
CSI	Chemical Shift Index
HADDOCK	High Ambiguity Driven Protein-Protein Docking
ITC	Isothermal Titration Calorimetry
EGTA	Ethylene Glycol-bis(β-aminoethyl ether)-N,N,N′,N′-Tetraacetic acid
RDC	Residual Dipolar Coupling

IPAP	Inphase/Antiphase
NOE	Nuclear Overhauser Effect
TOCSY	Total Correlation Spectroscopy
NOESY	Nuclear Overhauser Effect Spectroscopy
LC-MS	Liquid Chromatography Mass Spectroscopy
TCEP	Tris(2-Carboxyethyl)phosphine
MTSSL	*S*-(1-oxyl-2,2,5,5-tetramethyl-2,5-dihydro-1H-pyrrol-3-yl)methyl Methanesulfonothioate
DMSO	Dimethylsulfoxide
UV-vis	Ultraviolet-visible Absorption Spectroscopy
SEC-MALS	Size Exclusion Chromatography Multi-Angle Light Scattering
RP	Retinitis Pigmentosa

Table of Contents

Chapter 1

Introduction

1.1 Visual System and Phototransduction

Vision is one of the five sensory systems that are responsible in bridging the communication between our minds and the world around us. Vision begins in the eye, where light is focused onto the retina and is then converted into electrical signals involved in a sensory transduction called phototransduction [1-3]. This sensory transduction is a process by which the electrical responses are then transmitted to the brain to comprehend and generate a visual perception. The retina is located in the back of the eye comprised of layers of neurons that are all interconnected to transduce light signals into electrical information processed by the brain. It is highly conserved across all vertebrates and composed of different cell types including, photoreceptor cells, bipolar cells, and ganglion cells important for signal transduction (fig. 1.1.1) [2-4].

The first layer in the retina is made up of two classical types of photosensitive photoreceptor cells known as rod and cone receptor cells. Rods and cone cells are responsible for mediating different levels of vision, where rod cells function in low light and peripheral vision whereas cone cells function in high light and color vision [1-3, 5]. There are two important phases in phototransduction that are tightly regulated in the visual system: (1) visual excitation and (2) visual recovery.

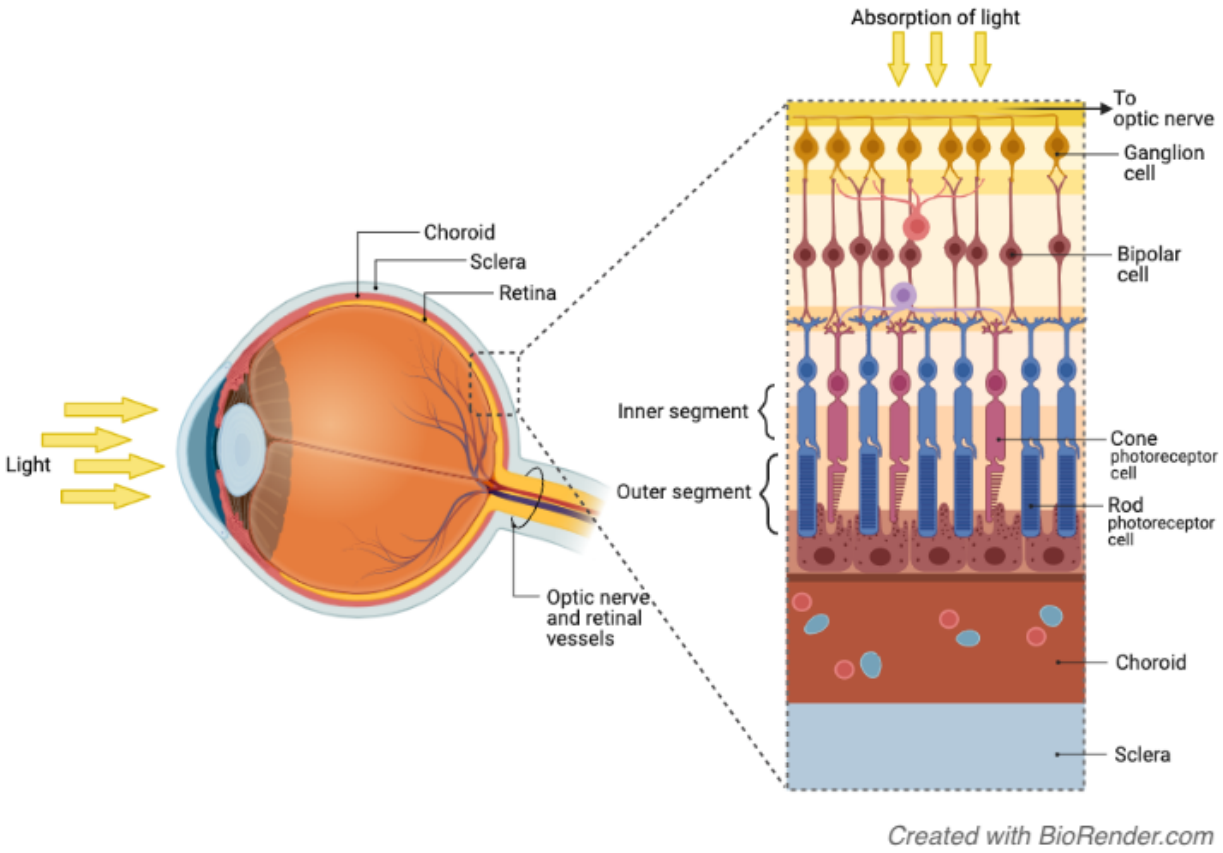

Fig. 1.1.1. Anatomy of the eye and visual phototransduction. Light is passed through the eye and is directed onto the retina, where it is absorbed in the photoreceptor cells. Light pathway in the retina goes from photoreceptors' outer segments to optic nerve for conversion into electrical signals for interpretation in the brain.

Visual excitation begins with light-induced activation of the visual pigment called rhodopsin. Vertebrate photoreceptor cells contain a conjugated chromophore, 11-cis retinal, that is covalently bound to a cell membrane protein called an opsin [1]. The absorption of an incident photon facilitates the isomerization of 11-cis retinal to 11-trans retinal, which thereby triggers the phototransduction cascade. This biochemical cascade is a G-protein coupled-receptor (GPCR) cascade comprising of opsin, transducin, phosphodiesterase (PDE6), and retinal membrane guanylyl cyclase (RetGC) [3-8]. The induced configuration of the conjugated chromophore causes a conformational change in opsin to an activated opsin R* or metarhodopsin II. From there, metarhodopsin II interacts with transducin to activate its catalysis. Transducin (G) is a

heterotimermeric protein that comprises of alpha, beta, and gamma subunits [1, 9]. The interaction of R* and G allows the exchange of a bound guanosine diphosphate (GDP) for a cytosolic guanosine triphosphate (GTP) and the release of its beta and gamma subunits. The GTP-bound alpha subunit G* is then able to bind to phosphodiesterase (PDE6) for activation [10].

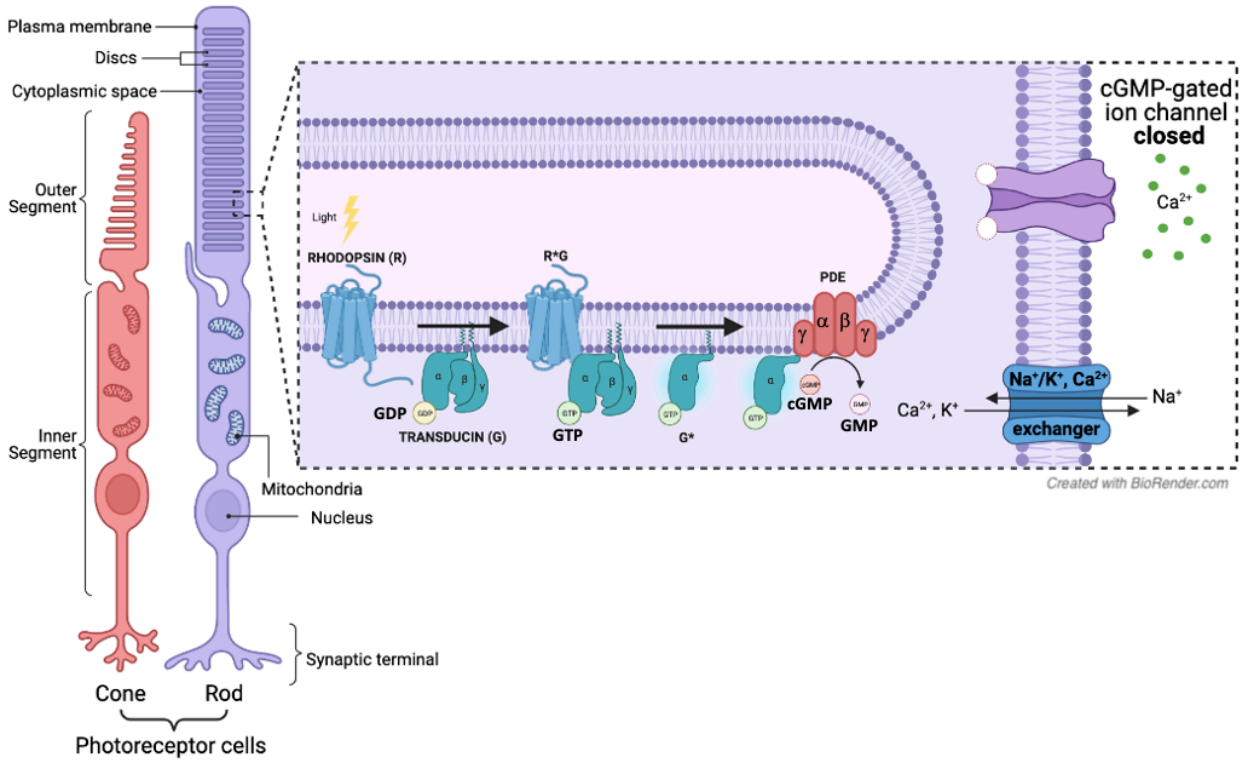

Fig 1.1.2. Visual phototransduction excitation. The incident photon triggers the activation of opsin (rhodopsin for rods), transducin, and phosphodiesterase. Light-activated PDE6 lowers key second messenger cGMP and results in CNG-gated ion channels closure.

1.2 Regulation of Visual Excitation by Phosphodiesterase (PDE6)

PDE6 is a key enzyme in visual excitation that catalyzes the hydrolysis of cyclic guanosine monophosphate (cGMP), a second messenger that gates the cyclic nucleotide gated ion channels (CNG) along the plasma membrane, to GMP. Light activation of a photoreceptor cell generates the formation of light-activated transducin (G*) that binds to the gamma inhibitory subunits of PDE6, allowing the activation of its alpha and beta subunits. From there, light-activated PDE6 catalyzes the hydrolysis of cGMP to form GMP and lowers the cytosolic concentration of cGMP

in photoreceptor cells. The light-induced decrease in cGMP causes the closure of the cGMP-gated ion channels and therefore, blocks the entry of both Na^+ and Ca^{2+}, which lowers the cytosolic concentration of these ions. The light-induced drop in cytosolic concentration of Na+ and Ca^{2+} ions cause a hyperpolarization of the plasma membrane that travels to the photoreceptor synaptic terminal, which triggers a reduction in the release of neurotransmitter, and generates a neural signal [2, 5, 6, 8, 11-15]. In contrast, dark-adapted photoreceptor cells are depolarized due to the Ca^{2+} and Na^+ influx through cGMP-gated ion channels that are kept open in the dark. As a result, the dark-adapted depolarized photoreceptors allow the continuous release of neurotransmitter glutamate that causes a constant dark current in the absence of light [5, 9, 16-18]. In essence, light activation of photoreceptor cells causes a decrease in current output. A key difference between the light-activated versus dark-adapted photoreceptor cell is that the cytosolic Ca^{2+} concentration is maintained to be relatively high (500 nM) in dark-adapted photoreceptor cells, whereas the Ca^{2+} level is ten-fold lower in light-activated cells. The light-induced decrease in cytosolic Ca^{2+} level is a key coordinating signal for promoting the re-opening of CNG channels during visual recovery, because the drop in Ca^{2+} level activates the re-synthesis of cGMP that is catalyzed by the enzyme, retinal guanylate cyclase (RetGC) described below in section 1.3.

1.3 Visual Recovery Regulated by Retinal Membrane Guanylyl Cyclase (RetGC)

The light-induced depletion of Ca^{2+} ions in photoreceptor cells trigger the visual recovery phase of phototransduction, which involves the re-opening of cGMP-gated (CNG) channels and restoration of the dark-state. The re-opening of CNG channels requires the re-synthesis of cGMP catalyzed by an important enzyme called retinal guanylyl cyclase (RetGC). RetGC catalyzes the resynthesis of cGMP from cytosolic guanosine triphosphate (GTP) and the cyclase catalytic

activity is regulated by calcium sensor proteins called guanylyl cyclase activating proteins (GCAPs). The Ca^{2+}-free state of GCAP proteins bind to RetGC and activate cyclase activity in light-activated photoreceptor cells when Ca^{2+} levels are decreased below 50 nM [1, 19-23]. By contrast, the Ca^{2+}-bound form of GCAPs inhibit the cyclase activity in dark-adapted photoreceptor cells when Ca^{2+} levels are increased above 500 nM [1, 19-23]. GCAPs are ~200-residue neuronal calcium sensor (NCS) proteins that regulate sensory transduction in the brain and retina. GCAPs contain four EF-hand motifs that allow binding to ions such as Ca^{2+} and Mg^{2+}, which is critical for its function in visual recovery.

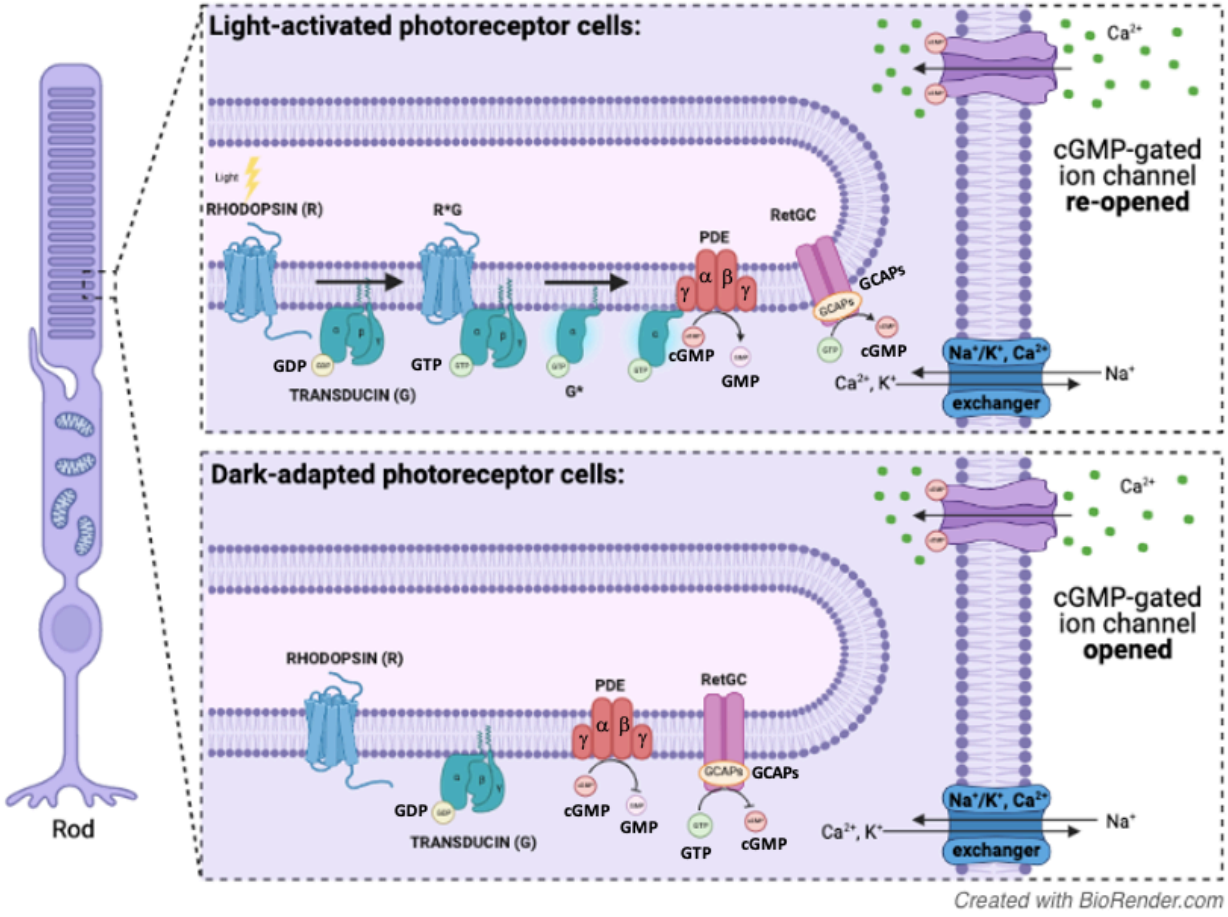

Fig. 1.2.1. Visual recovery phase. In light-activated photoreceptor cells, GCAP protein binds to RetGC at high levels of Ca^{2+} to activate cGMP resynthesis to reopen CNG-gated ion channels. In contrast, GCAP protein binds to RetGC at low Ca^{2+} levels to inhibit cGMP resynthesis.

The light-induced depletion of cGMP and closure of the CNG-gated channels result in the decrease in Ca^{2+} concentrations from 500 to 50 nM [1, 9, 19-25]. This light-induced drop in Ca^{2+} concentration triggers the activation of RetGC by its binding to Ca^{2+}-free GCAP. As a result, cGMP levels are replenished for CNG-gated channels to reopen during visual recovery [19-23, 26, 27]. In contrast, Ca^{2+}-bound GCAP binds to RetGC to inhibit its catalysis at the high Ca^{2+} and cGMP concentrations that exist in dark-adapted photoreceptor cells. Thus, RetGC undergoes a calcium-dependent regulation mediated by GCAP proteins, which activates the cyclase when it is needed during visual recovery and inactivates the cyclase when not needed in the dark. Mutations disrupting the interaction between GCAP proteins and RetGC disable the regulation of the visual recovery phase and are genetically linked to retinal generative diseases that may result in blindness or vision impairment [2, 6, 8, 28-31].

1.4 Structure and Function of GCAPs

The ability of GCAP proteins to activate and inhibit RetGC depends on the Ca^{2+}-dependent conformational changes in the GCAP proteins. GCAP proteins contain four EF-hand Ca^{2+}-binding motifs that are highly conserved in NCS proteins [6, 13, 32-36]. An EF-hand motif was first identified in the E and F helices of the crystal structure of parvalbumin (PDB: 1B8C) and observed 29 residues in a helix-loop-helix topology, exhibiting a similar shape to the spread from forefinger (E helix) to the thumb (F helix) [6, 9, 16, 17, 37-40]. The two EF-hand helices are linked by a flexible loop linker that follow a consensus sequence to allow Ca^{2+} and other biologically active metals to bind [37, 39-43].

There are two classes of EF-hands observed in NCS proteins: (1) canonical and (2) pseudo-EF-hands [7, 9, 33, 39-41, 44, 45]. Calcium binding proteins, like calmodulin (CaM) and GCAPs, comprise of 4 canonical EF-hand motifs with 12 amino acid residue loop that bind to Ca^{2+} in a pentagonal

bipyramidal coordination [13, 39, 42, 43]. The binding loop have highly conserved polar residues with sidechains containing carboxylate and carbonyls at strategic positions along the loop sequence to adapt to its correct configuration, providing oxygen ligands to the calcium ion.

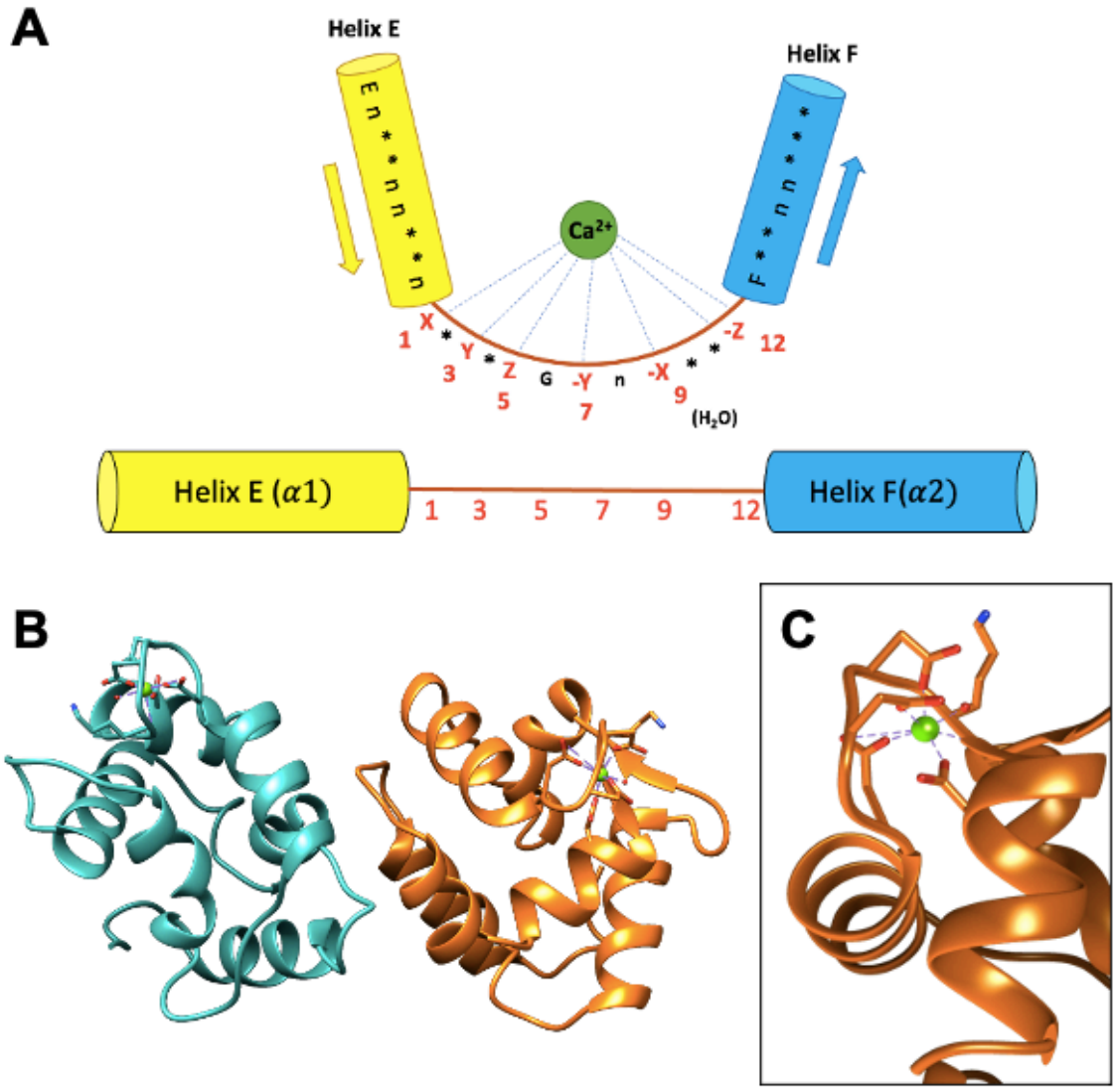

Fig. 1.4.1. EF-hand consensus (A) Consensus sequence of EF-hand motif. Sequence shows pattern of highly conserved residues, where N represents hydrophobic residues and asterisk (*) represent any residue. Loop positions 1, 3,5, 7, 9, and 12 contain oxygen atoms in their backbone and sidechains that ligate Ca^{2+} ion. (B) Parvalbumin crystal structure (PDB: 1B8C) containing EF-hand topology. (C) Ca^{2+} pentagonal bipyramidal coordination in EF-hand binding loop of parvalbumin (PDB: 1B8C) [6, 39, 43].

In fig. 1.4.1A, N residues are hydrophobic and asterisk (*) are classified as any amino acid. Among the 12 amino residues in the binding loop, only positions 1 (X), 3 (Y), 5 (Z), 7 (-Y), 9 (-X), and 12 (-Z) are directly involved in chelating Ca^{2+} (fig. 1.4.1A). Residues like aspartate (Asp, D), glutamate (Glu, E), asparagine (Asn, G), and glutamine (Gln, Q) contain oxygen atoms in its backbone and sidechains that are preferred as ligands to bind to Ca^{2+} [18, 33, 40, 44, 46]. Sidechain oxygens at positions 1 (X), 3 (Y), and 5 (Z) ligates Ca^{2+} while position 7 (-Y) is chelated by its backbone oxygen[39, 40, 46]. The ninth position, 9 (-X), is indirectly bound to Ca^{2+} through an associated water molecule (fig. 1.4.1). The highly conserved 12 (-Z) chelates the calcium ion with two oxygen-containing sidechains (usually Glu or Asp) to form the pentagonal bipyramidal coordination.

A conserved glycine (G) at position 6 of the EF-binding loop also plays an important role in achieving the correct conformation from apo- to Ca^{2+}-bound state[7, 39, 40, 45, 46]. More importantly, the identity of the 12th residue is critical in cation selectivity. The 12th position is conserved to be either glutamate (E) or aspartate (D). EF-hands containing Asp12 have shorter side chains than Glu12, making it difficult for Asp12 sidechain oxygen atoms to coordinate Ca^{2+} ion in the correct coordination. Because of the shorter side chain, EF-hands with Asp12 favor binding to Mg^{2+} due to the smaller binding site formed[39, 40, 46]. Mg^{2+} are able to bind to Ca^{2+} specific sites in an octahedral geometry, however, Mg^{2+} binding does not induce any conformational changes in the EF-hand[18, 39-41, 44, 46]. Other than selectivity, Mg^{2+} binding in NCS proteins stabilizes the Ca^{2+}-free state of the protein at low Ca^{2+} levels and is functionally different from the Ca^{2+}-bound state[18, 40, 46, 47].

In dark-adapted photoreceptor cells, there is an influx in Na^{+} and Ca^{2+} ions due to the presence of cytosolic cGMP levels maintaining a fraction of cGMP-gated ion channels to remain

open. However, there are light-insensitive Na^+/K^+, Ca^{2+} exchangers along the plasma membrane of a photoreceptor's outer segment that allow the continuous exit of Ca^{2+} ions in either light-activated or dark-adapted photoreceptors[5, 6, 17, 22, 23, 44, 48-50]. As a result, light-stimulated decrease in cGMP caused by PDE6 activation causes a substantial drop in intracellular Ca^{2+} ion concentration from 250 nM to 25 nM with cGMP-gated ion channels closing and Na^+/K^+, Ca^{2+} exchangers remaining opened[5, 9, 17, 23, 33, 48]. It is known that changes in Ca^{2+} levels trigger the visual recovery phase of photoexcitation, by which RetGC is either activated at low Ca^{2+} and inhibited at high Ca^{2+} levels. Previous studies of RetGC regulation were known to be dependent on the binding and release of Ca^{2+} ions in metal-free (apo-form) myristoylated GCAPs[51]. However, Mg^{2+} ions were discovered to be critical for stabilizing GCAP as the activator state[7, 11, 12, 40, 45, 46, 52, 53].

Of the four Ca^{2+} binding EF-hands in GCAPs, only EF2-4 are functionally capable of chelating Ca^{2+} and Mg^{2+} ions while EF1 is necessary for RetGC-GCAPs binding interactions[5, 6, 9, 21, 23, 34, 35, 38]. EF1 contains conserved loop residues Cys-29 (position 3, (Y)) and Pro-30 (position 4) that disable metal ion binding[1, 4]. *Peshenko et al.* observed that Ca^{2+} ions binding to EF2-4 at physiological Mg^{2+} levels (1 mM) in the dark-adapted state functioned as a RetGC inactivator[46, 54-56]. Conversely, Mg^{2+} is able to bind to EF2-4 and function as a RetGC activator in light-excited photoreceptors [40, 46, 47]. Moreover, Mg^{2+} binding to EF2-4 with an octahedral coordination at low Ca^{2+} levels cause conformational changes in EF1 that are favorable for RetGC activation[39]. *Peshenko et al.* confirmed disabling EF2-4 to bind to both Ca^{2+} and Mg^{2+} does not activate or inhibit RetGC activity [46].

All NCS proteins contain a covalently attached N-terminal myristoyl group. In some NCS proteins, the N-terminal myristoylation promotes Ca^{2+}-induced membrane targeting (termed Ca^{2+}-myristoyl switch) and functions as a Ca^{2+}-dependent anchor to cellular membranes [4, 9, 40, 43]. For

instance, myristoylation is important for recoverin to bind to disc membranes in the presence of high Ca^{2+} concentrations [57]. Absence of myristoylation in recoverin causes cytosol localization [58]. However, the myristoylated GCAP proteins do not possess a functional Ca^{2+}-myristoyl switch [33, 34]. The X-ray crystal structure of Ca^{2+}-bound GCAP1 inhibitor revealed that the myristoyl group was sequestered inside the protein, which makes hydrophobic contacts between the N- and C-termini helices [40, 53, 59, 60]. Moreover, *Lim et al* observed that the myristoyl group was buried inside GCAP1 at low and high Ca^{2+} concentrations and did not significantly affect folding stability by NMR and Differential Scanning Calorimetry (DSC) analyses[40].

A nuclear magnetic resonance (NMR) structure of Ca^{2+}-free/Mg^{2+}-bound $GCAP1^{V77E}$ was solved in 2016 by Dr. Sunghyuk Lim, a former post-doc of the Ames lab at the University of California Davis [14, 43, 53, 60]. Although the NMR structure of the Ca^{2+}-free GCAP1 mutant was similar to the X-ray crystal structure of a Ca^{2+} saturated GCAP1 solved by Dr. Ricardo Stephen, there were critical differences observed by NMR that identified functional Ca^{2+}-induced conformational changes [59]. NMR played an important role in locating residues along the sequence with Ca^{2+}-sensitive NMR chemical shift differences (fig. 1.4.2). More specifically, EF4 and the C-

terminal helix (α10) had the largest chemical shift differences (fig. 1.4.2) that agreed with the structural differences seen in the Ca^{2+}-free/Mg^{2+}-bound state versus Ca^{2+} saturated GCAP1 [53, 59].

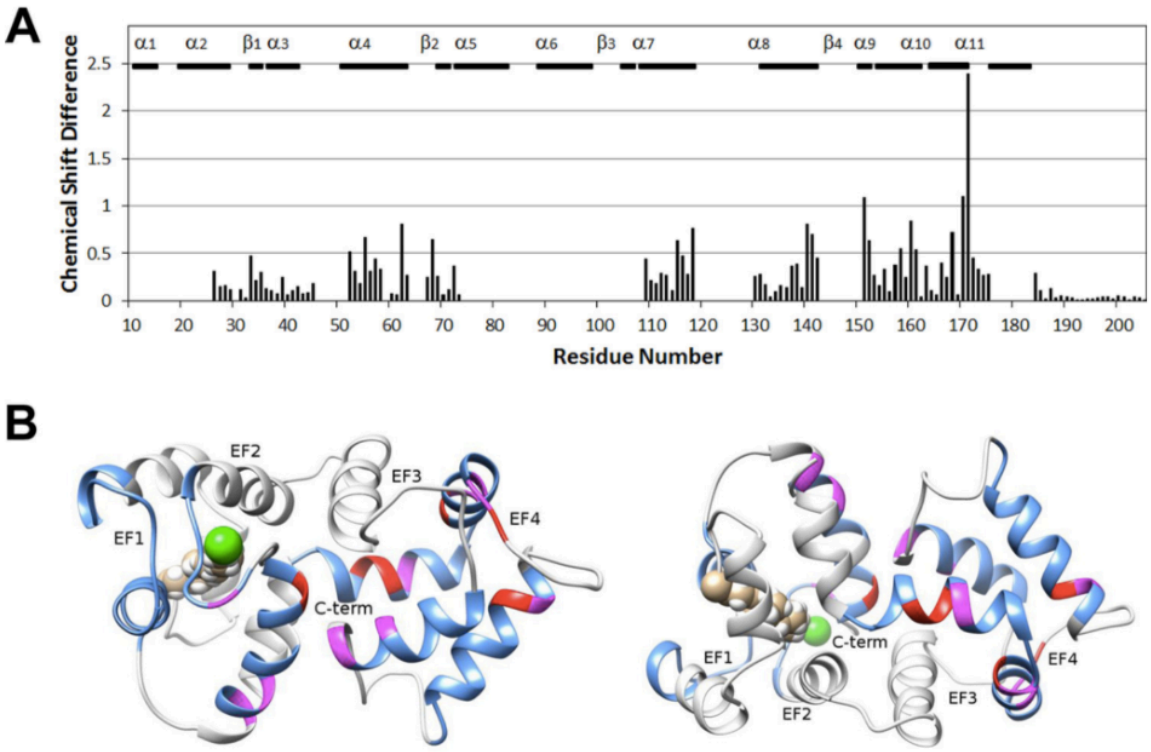

Fig. 1.4.2. Conformational changes in GCAP1 by presence of Ca^{2+} detected by NMR. (A) NMR amide chemical shift difference between Ca^{2+}-bound and Ca^{2+}-free plotted against residue number shows residues involved in structural changes. Critical residues exhibiting largest NMR chemical shift different are observed in EF4 (residues 140, 151-152, 160) and helix α10 (residues 168, 170-171). (B) Structure of GCAP1 mapping residues that observed chemical shift difference: red (> 0.8 ppm), magenta (0.5-0.8 ppm), and blue (<0.5 ppm) [21, 23]. Figure adapted and previously published in JBC (Lim et al, 2015) DOI: 10.1074/jbc.M115.696161
https://creativecommons.org/licenses/by/4.0/

The C-terminal helix (α10) of Ca^{2+}-free/Mg^{2+}-bound $GCAP1^{V77E}$, now termed as the Ca^{2+} switch helix, is one-half turn longer than the Ca^{2+} bound state (fig. 1.4.4). In particular, threonine-171 (Thr-171 or T171) and leucine-174 (Leu-174 or L174) in the C-terminal helix observed the greatest change in its structural environment [53, 61]. In the Ca^{2+}-free state, T171 is solvent exposed and L174 is buried and partakes in a hydrophobic contact with leucine-92 (Leu-92 or L92).

However, the converse is true in the Ca^{2+}-bound state – T171 is buried and L174 is solvent exposed [53]. These subtle conformational changes induced by Ca^{2+} in the Ca^{2+}-switch helix of GCAP1 confirms the switch from activator to inactivator [53, 59].

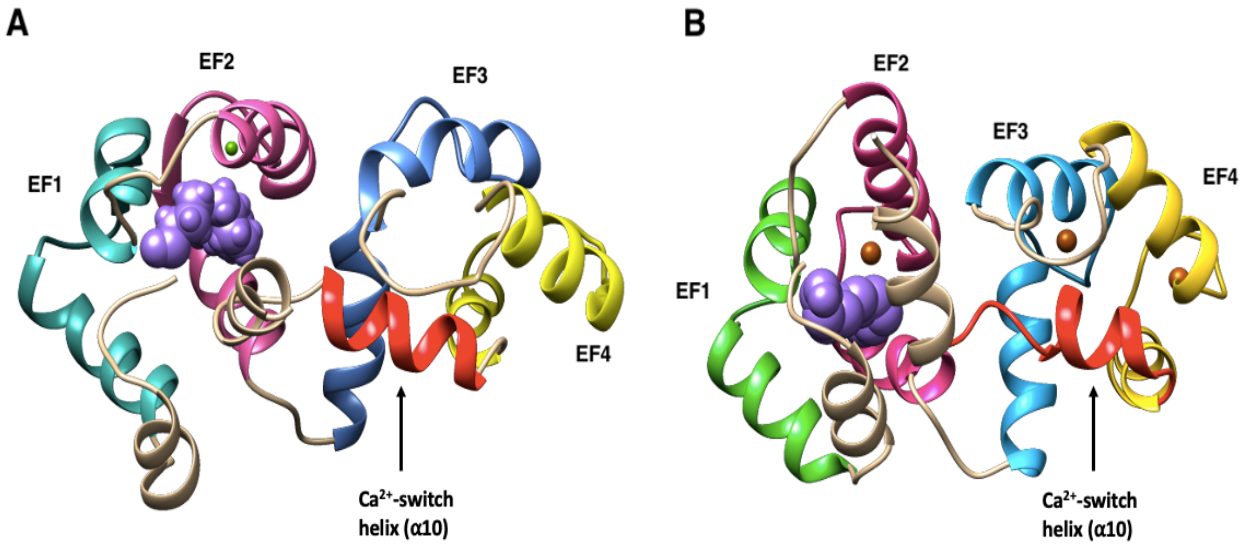

Fig. 1.4.4. Ca^{2+} induced conformational changes in GCAP1. (A) Ca^{2+}-free/Mg^{2+}-bound NMR structure of $GCAP1^{V77E}$ solved by Dr. Lim (PDB ID: 2NA0) that highlights the elongated Ca^{2+}-switch helix in *red*. (B) Ca^{2+} saturated X-ray crystallography structure of GCAP1solved by Dr. Stephen (PDB ID: 2R2I) shows the shortened Ca^{2+}-switch helix at high Ca^{2+} levels [53, 59]. N-terminal myristoyl-group is represented in purple and bound Mg^{2+} and Ca^{2+} ions are colored green and orange, respectively.

NCS proteins, such as recoverin and GCAPs, function as a dimer in physiological conditions [14, 42, 43, 53, 62]. In addition, most dimeric NCS proteins have similar amino acid sequences but bind and function in different sensory signal transduction pathways (fig. 1.4.5 below). Recoverin, found exclusively in retinal photoreceptor cells, functions to inhibit rhodopsin kinase in dark-adapted conditions [13, 14, 17, 37, 40, 43]. As mentioned previously, GCAPs regulate RetGC activity by binding to activate or inhibit when needed. In fig. 1.4.5, bovine GCAP1-2 and zebrafish GCAP5 are functional dimers that regulate dimeric RetGC. In particular, GCAP1 exists in two sensory systems with different functions: visual and olfactory [4, 16, 17, 43]. In the retina, Ca^{2+}-free

GCAPs bind to RetGC at low Ca^{2+} levels to activate the resynthesis of cGMP [6, 11, 33, 34, 36, 41, 46, 54, 59]. In contrast, Ca^{2+}-bound GCAPs bind to RetGC at high Ca^{2+} levels to turn off RetGC activity in dark-adapted photoreceptor cells [5, 19, 23, 33, 38, 48, 49]. In the olfactory sensory system, Ca^{2+}-bound GCAP1 activates the surface receptor ONE-GC [32, 43].

```
                    10        20        30        40        50        60
GCAP1       MGNIMDGK-- --------SV EELSSTECHQ WYKKFMTECP SGQLTLYEFR QFFGLKNLSP
GCAP5       MGDSSS---- -------MSA TELSACKCHQ WYRKFMTECP SGQLTFYEFK KFFGLKNLSE
RECOVERIN   MGNSKSGALS KEILEELQLN TKFTEEELSS WYQSFLKECP SGRITRQEFQ TIYSKFFPEA

                   70        80        90       100       110       120
GCAP1       WASQYVEQMF ETFDFNKDGY IDFMEYVAAL SLVLKGKVEQ KLRWYFKLYD VDGNGCIDRD
GCAP5       KSNAYVNTMF KTFDIDDDGC IDFMEYVAAL SLVLKGGVQQ KLRWYFKLFD MDGSGCIDKD
RECOVERIN   DPKAYAQHVF RSFDANSDGT LDFKEYVIAL HMTSAGKTNQ KLEWAFSLYD VDGNGTISKN

                  130       140       150       160       170       180
            ELLTIIRAIR AIN----PCS D------STM TAEEFTDTVF SKIDVNGDGE LSLEEFMEGV
GCAP1
GCAP5       ELLLIFKAVQ AIN----GAE -------PEI SAEDLADIVF NKIDVNGDGE LSLEEFMEGI
RECOVERIN   EVLEIVTAIF KMI----SPE DTKHLPEDEN TPEKRAEKIW GFFGKKDDDK LTEKEFIEGT

GCAP1       QKDQMLLDTL TRSLDLTR-I VRRLQNGEQD EEGASGRETE AAEADG      205
GCAP5       SADEKISEML TQSLDLTR-I VSNIYNDSYI EQEAEIIEDQ A           198
RECOVERIN   LANKEILRLI QFEPQKVKEK LKEKKL                            202
```

Fig. 1.4.5. Sequence alignment of functional dimeric NCS proteins. Highlighted in red are amino acid residues at the dimeric interface of selected NCS proteins. Swiss Protein Database accession numbers are P4606 (bGCAP1), 51177 (bGCAP2), Q5MAC8 (zGCAP5), and P21457 (bovine recoverin) [43].

The Ca^{2+}-dependent conformational changes in the tertiary structure of GCAPs are considered minor. However, these relatively small changes in the C-terminal helix and EF-hands are hypothesized to facilitate a large change in the dimer's quaternary structure that bind to RetGC dimer differently [43, 53]. In fig. 1.4.6 below, an illustration shows the effect of small Ca^{2+}-induced tertiary structural changes in GCAP1 that facilitate larger quaternary structural changes in the dimer that in turn promote conformational changes in RetGC that confer Ca^{2+}-dependent cyclase

activity [55]. To test this model, I will determine the structure of dimeric GCAP proteins in my thesis research below.

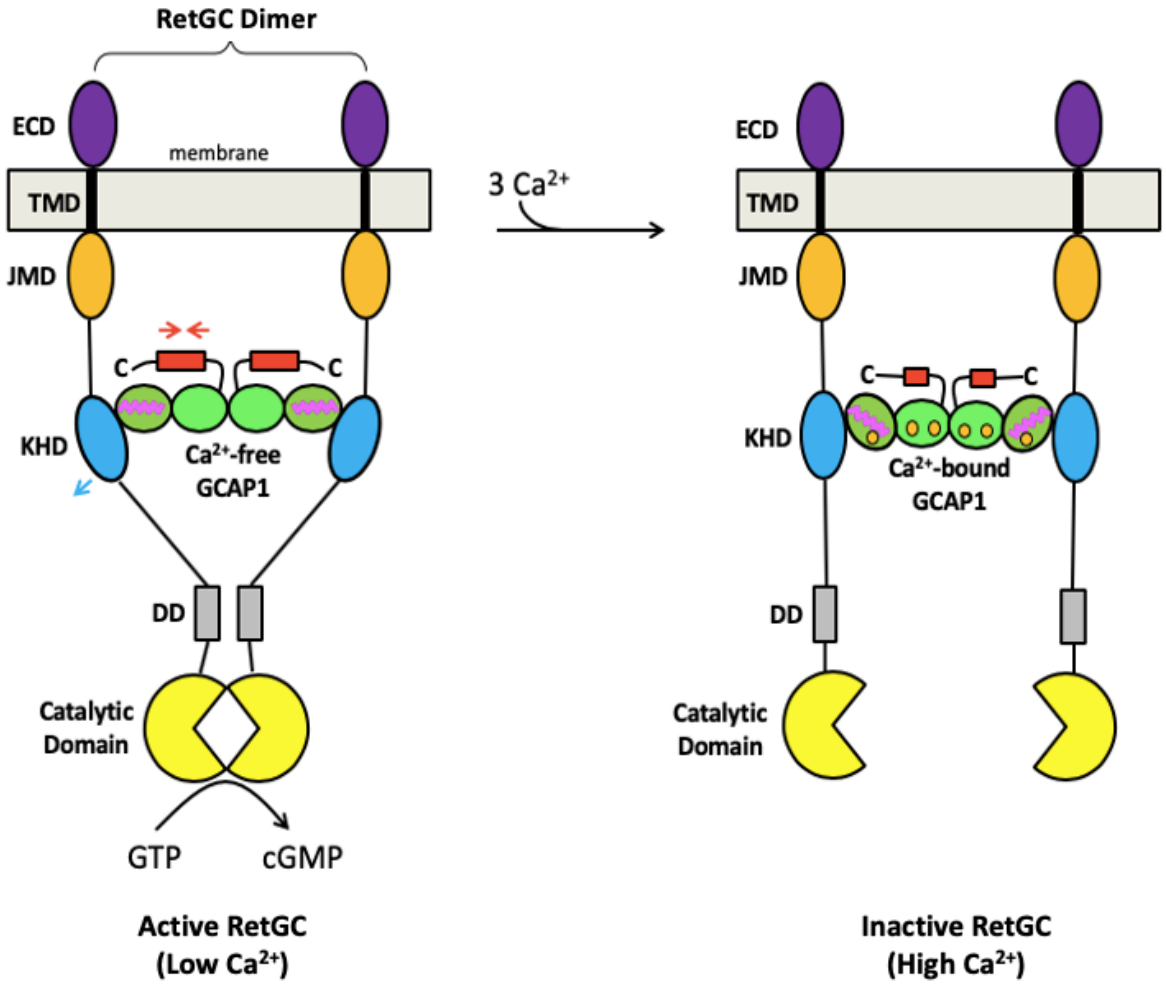

Fig. 1.4.6. Ca^{2+}-dependent regulation of RetGC mediated by GCAPs. Ca^{2+}-free myristoylated GCAP1 dimer (left) is an activator at low Ca^{2+} and (B) Ca^{2+}-bound myristoylated GCAP1 dimer is an inactivator at high Ca^{2+} [55].

1.5 Role of Retinal Degeneration 3 (RD3) Protein

RetGC is a critical enzyme for photoreceptors to recover from photoexcitation. In addition to the cyclase's regulation by GCAPs, retinal degeneration 3 (RD3) protein can bind to RetGC to inhibit cyclase activity [63-65]. Moreover, RD3 is a 23-kDa non-calcium binding protein found in the

inner segment of photoreceptor cells and is needed for trafficking RetGC into the outer segments [63, 66-68]. Leber's congenital amaurosis (LCA) is a rare autosomal recessive eye disorder that affects the retina and can cause visual impairment in infancy [67-70]. It was discovered that the lack of RD3 in LCA human patients and in the rd3 mouse strain led to severe retinal degeneration and in some cases, blindness [63, 66-69, 71]. *Peshenko et al* confirmed that RD3 functions as a high-affinity inhibitor of RetGC at basal activity and light-activation by GCAPs *in vitro* [63, 67, 72]. Moreover, the decrease in RD3 significantly lowered the RetGC concentration in photoreceptors, emphasizing the importance of RD3 in transporting the cyclase into the outer segment (Azadi et al., 2010; Peshenko et al., 2011). Thus, RD3 is critical for RetGC trafficking and suppressing basal cyclase activity for the survival of photoreceptor cells.

RetGC is first synthesized in the endoplasmic reticulum (ER) of photoreceptor's inner segment before it is transported to the outer segment (see fig. 1.5.1. below). RD3 binds to RetGC and induces membrane curvature to allow the exit of RetGC-RD3 complex as spherical vesicles [73]. The RetGC-RD3 membrane-bound transport intermediate leaves the ER and cyclase is inhibited by RD3 throughout the RetGC trafficking into the outer segment to prevent photoreceptor impairment [63, 67, 68, 71, 73]. When the RetGC-RD3 complex reaches the cilium, RetGC is dissociated from the vesicle via post-translational modification before it is incorporated into the disk membranes [73]. Finally, RD3 is then returned to the ER to repeat the RetGC trafficking (fig. 1.5.1).

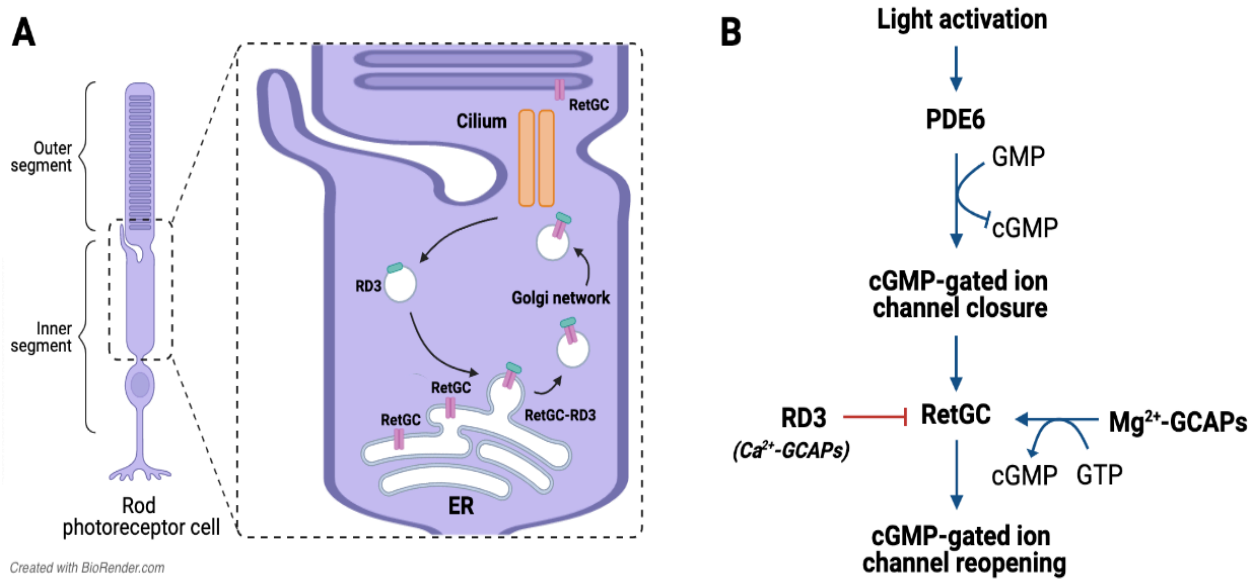

Fig. 1.5.1. Role of RD3 in RetGC trafficking and regulation. (A) Anatomy of a photoreceptor inner segment shows RD3 as a RetGC inhibitor and facilitates trafficking of RetGC from the endoplasmic reticulum to the outer segment. (B) Light-activated PDE6 causes decrease in cGMP that closes cGMP-gated ion channels. Light-induced drop in cGMP prevents Ca^{2+} influx and visual recovery is turned on when Ca^{2+}-free GCAPs bind to RetGC. RD3, similar to Ca^{2+}-bound GCAPs), inhibit cyclase activity.

Overall, RD3 is critical as a negative regulator of RetGC cyclase activity during the transport to the photoreceptor's disk membranes while suppressing RetGC basal activity and stimulation by GCAPs [74, 75]. The absence of RD3 and/or mutations linked by RD3 can cause a decrease in RetGC in photoreceptor cells and result in retinal degenerative disorders [31, 41, 67, 68, 73, 74].

1.6 Mutations in GCAPs and RD3 Lead to Retinal Degenerative Diseases

RetGC1 is one of the most important enzymes involved in vertebrate phototransduction. Visual recovery is regulated by RetGC mediated by the Ca^{2+} and Mg^{2+} sensors GCAPs, by which RetGC is activated at low Ca^{2+} and inhibited at high Ca^{2+} levels. In addition, the accumulation of the key enzyme and survival of photoreceptors is dependent on the high affinity inhibitor RD3

expressed in the inner segment [65, 73, 74, 76]. Hence, any mutations linked to RetGC isozymes (*RetGC1* and *RetGC2*) weakens the cyclase activity and leads to retinal degenerative blinding disorders [67, 74, 77, 78]. More specifically, it was found that R838 substitutions in the dimerization domain of human RetGC1 isozyme (human gene *GUCY2D*) is genetically linked to cone-rod dystrophy type 6 (CORD6), a retinal degenerative disorder causing early-onset loss of photoreceptor cells [74, 79]. Substitutions of R838 was discovered to induce changes in Ca^{2+} sensitivity of RetGC as structural changes in the dimerization domain, the binding interface for GCAPs, by reducing their binding affinity and overall resulting in the photoreceptor deterioration [55, 56, 74, 79]. Thus, research efforts on determining the three-dimensional structures of GCAPs, RD3, and RetGC are critical to understand the structure-function relationship and provide information for developing new drugs targeting retinal degenerative disorders.

Additionally, mutations found in the Ca^{2+} and Mg^{2+} sensing GCAP proteins can also affect the survival of vertebrate photoreceptors [41, 51, 54, 56]. Mutations in Y99, N104, I143, L151, and E155 of EF3-4 of GCAP1 are genetically linked to autosome dominant cone-rod dystrophy [6, 30, 69, 72, 80-83]. Substitutions in these specified critical residues weakens and/or disables the EF-hand binding loop responsible for coordinating Ca^{2+} ions. Consequently, the changes induced in the coordination of Ca^{2+} causes less sensitivity in GCAP1 to inhibit RetGC even at high Ca^{2+} levels [38, 84]. GCAP1 loses its full ability to inhibit the cyclase at high Ca^{2+} levels and allows RetGC to continue catalyzing the re-synthesis of cGMP in dark-adapted photoreceptors [7, 8, 14, 48, 84, 85]. As a result, the cGMP-gated ion channels remain and allow influx of Ca^{2+} that can turn on apoptosis and photoreceptor death. Hence, it is important to determine the structure of GCAPs and utilize the structural data to understand the structure-function relationship that can provide clues on the molecular mechanisms of mutations linked to blinding disorders.

As mentioned, RD3 has two important functions in photoreceptor regulation: (1) a high affinity inhibitor of RetGC to suppress cyclase activity and light-stimulation by GCAPs, and (2) facilitates RetGC trafficking from inner to the outer segment of photoreceptors [63, 64, 66]. Indeed, a nonsense mutation that causes the absence of RD3 is associated to severe retinal degenerative disorders such as Leber's congenital amaurosis type 12 (LCA-12) [71, 86]. Thus, research efforts on determining the three-dimensional structures of GCAPs, RD3, and RetGC are critical to understand the structure-function relationship and to provide information for developing new drugs targeting retinal degenerative disorders.

1.7 PURPOSE OF STUDY

My thesis research primarily involved doing structural analysis of RD3 and GCAP5. My first project was to develop a protocol for the preparation of the RD3 protein for Nuclear Magnetic Resonance (NMR) structural studies. Previous attempts to prepare a soluble full-length RD3 were unsuccessful due to sample aggregation that prevented its structural analysis by X-ray crystallography and/or NMR. In chapter 2, I will describe an elaborate protocol for the protein expression, refolding, and purification of RD3 for NMR structural analysis. My development of the sample preparation protocol was essential for the NMR structure determination and proved to be a significant effort. In chapter 3, I present my structural analysis of dimeric GCAP5 by NMR and Electron Paramagnetic Resonance Double Electron-Electron Resonance (EPR-DEER). These NMR and EPR-DEER studies will probe hot spot residues at the dimeric interface that may be associated to genetically linked retinal degenerative diseases. Additionally, this structural information will allow better understanding of the functional contacts in the RetGC-GCAP5 complex and provide insights for drug discovery and development to aid in treating retinal degenerative diseases.

Chapter 2

NMR Structural Studies of retinal degeneration protein-3 (RD3)

2.1 Introduction

Cyclic guanosine monophosphate (cGMP) is a key second messenger in the visual sensory system that functions as a gatekeeper to the cGMP-gated (CNG) ion channels along the plasma membrane of photoreceptor cells [87]. The absorption of light in the retina triggers a phototransduction cascade, followed by the activation of phosphodiesterase (PDE6) [10]. PDE6 is an important enzyme in visual excitation as it catalyzes the hydrolysis of second messenger cGMP to guanosine monophosphate (GMP); thus, the reduction of cGMP results in the closure of CNG channels, which blocks the entry and Na^+ and Ca^{2+}, causes membrane hyperpolarization, and generates a neural signal [2-4, 87].

To recover from visual excitation (when the light stimulus is removed), retinal membrane guanylyl cyclase (RetGC) is turned on to replenish cGMP that is needed for the re-opening of the CNG channels. RetGC is an important enzyme for the visual recovery phase of light-activated photoreceptors as it catalyzes the resynthesis of cGMP from cytosolic guanosine triphosphate

(GTP) by binding to calcium-binding proteins called guanylyl cyclase activating proteins (GCAPs) [6, 34-36].

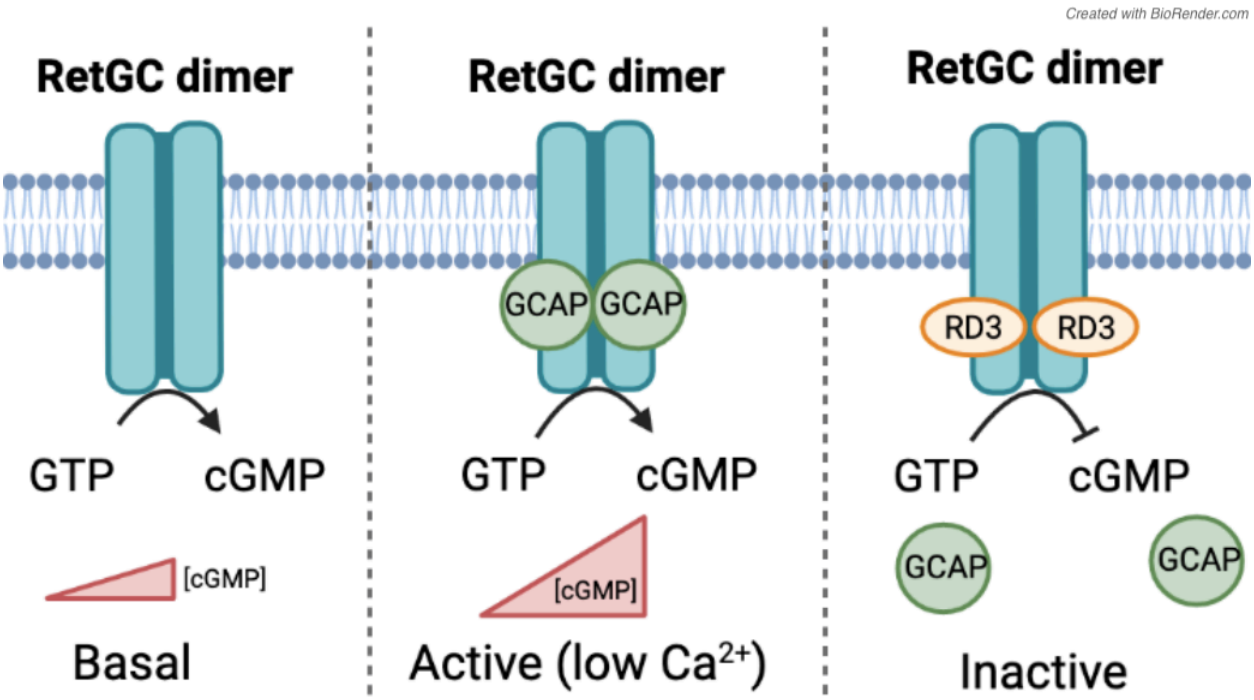

Fig. 2.1.1. Regulation of RetGC by GCAPs and RD3. cGMP is replenished at RetGC basal activity (left). When RetGC is activated by GCAPs as a light-stimulated activator at low Ca^{2+} concentration (center), cGMP levels are amplified. In the presence of GCAPs, RetGC is inactive when RD3 binds as a high affinity inhibitor (right).

RetGC is activated when it binds to Mg^{2+}-bound GCAPs at low Ca^{2+} and is inhibited when it binds to either Ca^{2+}-bound GCAPs or the RD3 protein (fig. 2.1.1) [11, 18, 40, 46]. In essence, Ca^{2+}-free GCAP proteins bind to and activates RetGC at high light levels and Ca^{2+}-bound GCAPs and/or RD3 binds and inactivates RetGC in the dark. The GCAPs and RD3 compete for binding to the same site in RetGC [63]. Thus, regulation of RetGC mediated by GCAPs and RD3 is essential for the survival of photoreceptor cells. Mutations genetically linked to RetGC, GCAPs, or RD3 can cause visual impairment and is associated with retinal degenerative diseases such as rod-cone dystrophy and Leber's congenital amaurosis type 1 (LCA-1) [12, 70, 76].

The role of RetGC is imperative to the regulation of visual recovery in light-excited photoreceptor cells. Before RetGC is integrated in the outer segment, RetGC is first synthesized in the inner segment before it is trafficked into the disk membranes of the photoreceptor cells [63, 64, 66, 67, 71]. More specifically, RetGC is produced in the endoplasmic reticulum (ER) as a membrane bound protein. When RD3 binds to the cyclase, the RetGC-RD3 complex causes a physical bending of the membrane that allows the membrane-bound intermediate to bud out and exit the ER [63, 64, 66, 67]. When the RetGC-RD3 membrane-bound transport intermediates leave the ER, RD3 initiates the trafficking of RetGC into the outer segment while suppressing its catalytic activity [63, 64, 66-68, 71]. RetGC-RD3 is transported through the Golgi before RetGC dissociates from the small vesicle and passes through the cilium [63, 67, 71]. Fig. 1.5.1 shows RetGC being incorporated into the disk membranes and thus, trafficking facilitated by RD3 is essential for accumulation of RetGC in the outer segment of photoreceptor cells. Thus, mutations in RetGC isozymes and/or RD3 that disrupt RetGC binding to RD3 will increase the residual cyclase activity (because RD3 binding inhibits the cyclase) that will in turn increase the basal concentration of cGMP and therefore promote apoptosis and diminish the integrity of photoreceptors [63, 64, 66-68, 71, 73].

Since the discovery of RD3, the low abundance of the native protein in photoreceptors posed as a major challenge for doing structural analysis. Additionally, recombinant full-length RD3 had the tendency of aggregation and precipitation when expressed in bacterial cells [73, 74, 86]. The low abundance and solubility challenges of the native full-length RD3 made it difficult to prepare purified samples that were sufficient for NMR and/or X-ray crystallography studies [67, 75]. In this chapter, I will discuss my development of a detailed protocol for doing protein expression and purification of a functional truncated RD3 for NMR structural analysis. This deletion construct (18-161, RD3-d) was observed to be functional and soluble enough for NMR structural studies,

which was essential for solving the three-dimensional structure. The three-dimensional structure of RD3 provides insights in understanding RetGC-RD3 binding interactions, RD3 trafficking mechanism, and drug development for mutations linked to retinal degenerative disorders.

2.2 Materials and Methods

Optimized overexpression of RD3-d construct

Initial attempts to express and isolate full-length human RD3 caused aggregation and precipitation in bacterial cells, by which sample conditions were not amenable for NMR structural studies. To overcome the obstacle, Dr. Alexander M. Dizhoor (Salus University, PA, USA) created a deletion construct (residues 18-160, called RD3-d) by PCR amplification using Phusion Flash polymerase and subcloned into pET11d vector to produce recombinant soluble RD3-d exclusive of any affinity tags [74]. Uniformly ^{15}N-labeled and ^{13}C, ^{15}N-labeled samples of RD3-d were expressed in BL21(DE3)CodonPlus *E. coli* strain and purified from inclusion bodies [75, 86].

A frozen stock of RD3-D is inoculated in a 20 mL Luria broth (LB) with a final concentration of 100 μg/mL ampicillin (100 mg/mL stock) and was grown for 3-4 hours in a 37°C, 200 rpm shaking incubator before it is inoculated in a 1L M9 minimal media until A_{600} 0.6. Protein expression was induced by adding a final concentration of 1 mM isopropyl-β-D-1-thiogalactopyranoside for 4 hours. The bacterial cell pellet was harvested by centrifugation at 6,000 rpm for 20 minutes (Thermo Scientific fixed angle rotor F9-4x1000y) at 4°C and stored in -80°C overnight [74].

Isolation of folded RD3-d by urea extraction

The bacterial cell pellet was resuspended in 25 mL lysis buffer termed TEM buffer consisting of 10 mM Tris-HCl (pH 8.3), 0.5 mM EDTA, 14 mM 2-mercaptoethanol (BME). The RD3-d lysate was then sonicated on ice for 2 min (output = 3 with 2 min cooling interval) and

repeated twice. The inclusion bodies from the lysed cells were isolated by centrifugation at 22,000 x g for 20 min at 4°C in (Sorvall fixed angle rotor SS-34). After initial pre-extraction, the sonication and centrifugation were repeated once for washing. The washed pellet comprising of inclusion bodies was resuspended in 12 mL of 10 mM Tris-HCl (pH 7.5), 2 mM EDTA, 14 mM 2-mercaptoethanol (BME), and 8 M urea for urea extraction. This was gently stirred for 35 min at 4°C and then centrifuged at 22,000 x g for 10 min at 4°C. The supernatant consisting of soluble RD3-d was dialyzed against 1 L of 10 mM Tris-HCl (pH 7.5), 0.1 mM EDTA, and 14 mM BME for 3-4 h without stirring and then overnight against fresh 1 L of the same buffer with stirring at 4°C. Dialyzed protein was centrifuged at 22,000 x g for 20 min at 4°C.

Purification of RD3-d by Fast Protein Liquid Chromatography (FLPC)

A final concentration of 1M NaCl and 5 mM DTT was added to RD3-d before FPLC protein purification. RD3-d was purified by hydrophobic interaction Octyl-Sepharose, anion exchange (HiTrap Q HP, GE Healthcare), and size exclusion Superdex-200 column chromatography. RD3-d was purified to be more than 95% pure analyzed by SDS-PAGE.

NMR Spectroscopy

Uniformly ^{15}N-labeled and ^{13}C, ^{15}N-labeled samples of RD3-D were exchanged into an NMR buffer comprising of 5 mM Tris-d_{11} (pH 7.4), 3 mM dithiothreitol-d_{10} (DTT-d_{10}), 50 μM ethylenediaminetetraacetic acid-d_{12} (EDTA-d_{12}), 0.04% w/v NaN_3, and 93% H_2O/7% D_2O and had a final concentration between 0.5 – 0.9 mM. All NMR experiments were performed at 23°C on a Bruker Avance 600 MHz spectrometer with a four channel interface and triple resonance cryogenic (TCI) probe [86]. Assignments of backbone resonances were acquired by performing and analyzing the following two- and three-dimensional spectra: HNCA, HNCACB, CBCA(CO)NG, and HNCO [88]. In addition, assignments of sidechain resonances that assist in three-dimensional structural

elucidation were obtained from the following spectra analysis: HCCH-TOCSY, CCCONH, HCCCONH, ^{13}C-edited NOESY, ^{15}N-edited NOESY and TOCSY, and CT-HSQC [86]. NMR spectra were processed using NMRPipe and probed using Sparky NMRFAM software [86, 89, 90]. NMR backbone assignments were initially acquired by Dr. Sunghyuk Lim and later the three-dimensional structure was solved by Dr. Qinhong Yu [75, 86].

2.3 Results and Discussion

Solving the three-dimensional atomic-level structure of the RD3 protein faced two major challenges: (1) low expression of soluble recombinant protein in bacteria and (2) large tendency of protein aggregation and precipitation that prevented the formation of concentrated protein samples (10 mg/mL) needed for structural analysis [75, 86]. Before I joined the lab, Dr. Sunghyuk Lim in the Ames lab made initial attempts to express full-length RD3 in bacteria and to purify the recombinant protein for NMR structural analysis. However, samples of the full-length recombinant protein were low-yielding due to protein aggregation and NMR resonances were severely broadened, perhaps caused by protein self-association. When I joined the lab in 2017, our collaborator, Dr. Sasha Dizhoor suggested that the first 18 residues from the N-terminus and the last 28 residues at the C-terminus in RD3 contained many small amino acids that usually form a random coil. Dr. Dizhoor surmised that these residues in RD3 were likely unstructured and might contribute to the sample heterogeneity suggested by the broad NMR signals. Therefore, Dr. Dizhoor prepared a truncated deletion construct of RD3 (residues 18-160, called RD3-d) and he verified that RD3-d remained functionally intact [74]. The functional assay required recombinant RetGC1 expressed in HEK293 cells and recombinant GCAP1 expressed in *E. coli* [74]. The addition of RD3-d preserved its function as a high affinity inhibitor to RetGC in the presence of GCAPs *in vitro* [75].

When expressing the recombinant RD3-d in bacteria, the recombinant RD3-d protein expression was more than 5-fold greater than that of full-length RD3. However, the expressed RD3-d protein was now found exclusively in the insoluble fraction of the bacterial lysate, known as inclusion bodies. My first assignment when I first joined the lab in 2017 was to develop a purification strategy for the RD3-d variant protein from inclusion bodies. I found that the RD3-d inclusion bodies could be effectively solubilized using 8 M urea; however, when dialyzing the urea solubilized RD3-d against PBS buffer under physiological conditions, more than 90% of the refolded RD3-d protein precipitated in the presence of 0.15 M KCl. Surprisingly, if I removed all the salt (NaCl and KCl) from the refolding buffer (TEM buffer), the dialysis of the urea solubilized RD3-d resulted in the striking formation of a soluble form of the refolded RD3-d protein that did not precipitate during the dialysis against TEM buffer. The refolded and solubilized RD3-d prepared in this way could then be purified as described below. These purified RD3-d samples were shown to bind functionally to RetGC and inhibit cyclase activity just like the wild-type protein[75]. These purified RD3-d samples could be concentrated to more than 10 mg/mL without aggregating and were therefore now suitable for structural analysis by NMR. Moreover, the size exclusion chromatography coupled with multi-angle light scattering (SEC-MALS) analysis determined that RD3-d forms a stable monomer in solution (17 ± 1 kDa) (fig. 2.3.1) [75]. A detailed protocol that I developed for preparing isotopically labeled RD3-d samples for NMR is described below.

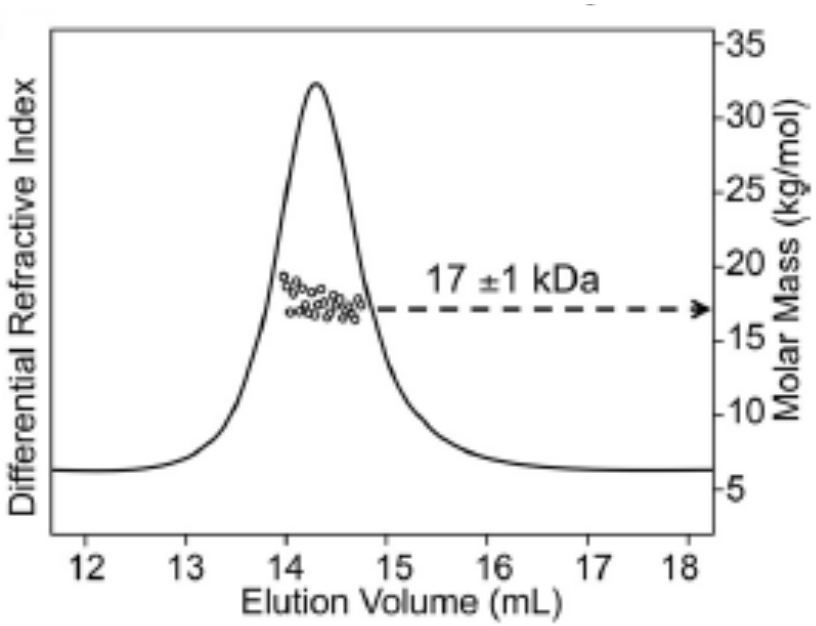

Fig. 2.3.1. SEC-MALS analysis. The absolute molar mass of RD3-d reported to be 17 ± 1 kDa and is independent of the shape. The 17 kDa molar mass was determined by the Zimm plot of the observed light scattering with a refractive index *dn/dc* 0.185 of l/g [75]. Figure previously published in JBC (Peshenko, Yu et al, 2019) DOI: https://doi.org/10.1074/jbc.RA118.006106 https://creativecommons.org/licenses/by/4.0/

Uniformly ^{15}N-labeled and ^{13}C, ^{15}N-labeled samples of RD3-d for NMR studies were expressed in *E. coli* using minimal M9 media [74, 75, 86]. RD3-d was exclusive of affinity tags and purified from inclusion bodies [74, 75, 86]. Protein expression was induced by IPTG for 4 hours at 25°C before cells were harvested by centrifugation. Resuspended cells were lysed with RD3 lysis buffer (as previously described in 2.2 methods and materials) and by sonication. After initial centrifugation, lysis and sonication was repeated once again before 8 M urea extraction. The pellet containing insoluble and misfolded RD3-d was resuspended in 8 M urea to unfold and increase its solubility [74, 75, 86]. Unstructured RD3-d becomes was now more soluble and protein folding was initiated by dialysis against 1 L of TEM buffer in the absence of 8 M urea over 24 hours. Folded

RD3-d was centrifuged and final concentrations of 1M NaCl and 5 mM DTT was added before purification by FPLC.

First, the soluble fraction of RD3-d from the refolding step above was loaded onto a hydrophobic interaction column (HIC) using a high salt loading buffer A (20 mM Tris-HCl (pH 8.0), 1M NaCl) and then protein was eluted with a gradient from buffer A to elution buffer B (20 mM Tris-HCl (pH 8.0) over 50 minutes at a flow rate of 2.0 mL/min. Hydrophobic columns with varying lengths of immobilized straight chain alkyl ligands were tested to determine the column efficiency and its ability to fractionate a greater amount of protein for further purification. The 16-kDa truncated RD3-d was successfully purified by using an octyl-sepharose hydrophobic interaction column as monitored by SDS-PAGE analysis (fig. 2.3.2).

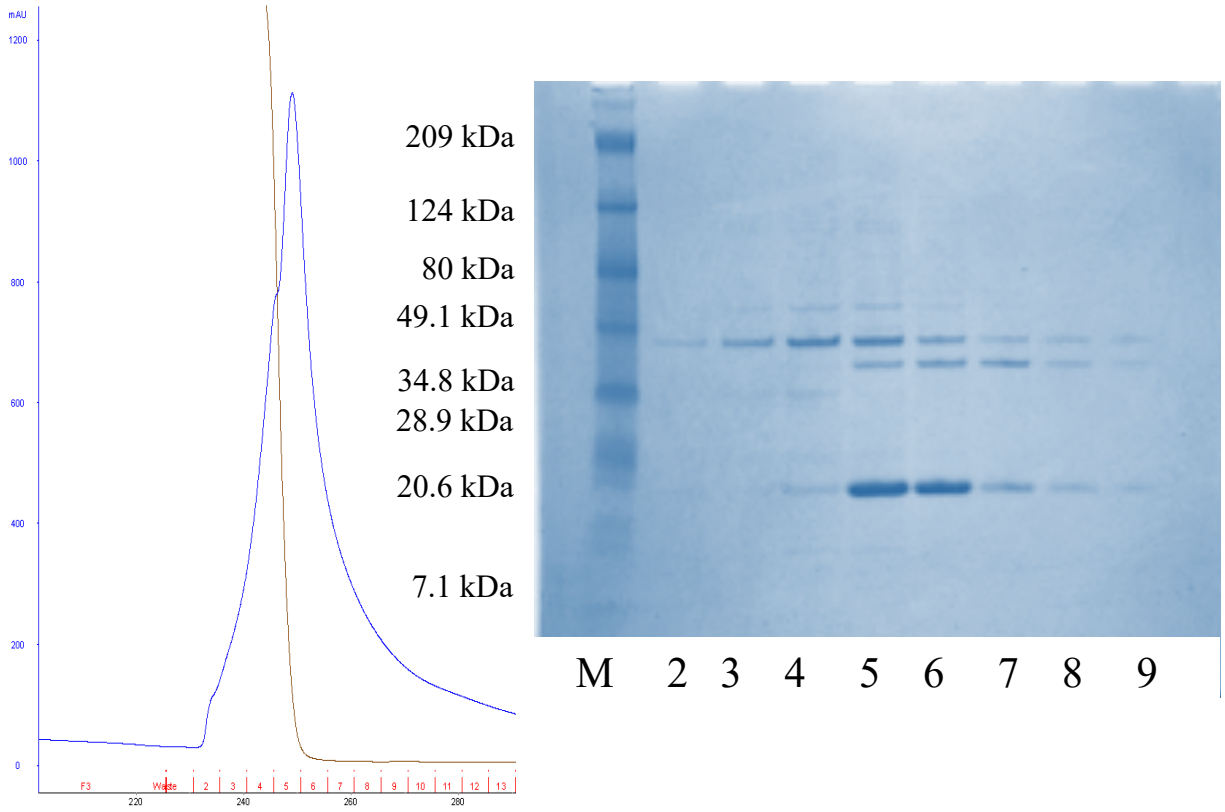

Fig. 2.3.2. Hydrophobic interaction column. Chromatogram of RD3-d using an octyl-sepharose column. RD3-d was loaded onto the column with high salt and eluted at low salt. Fractions #1-9 were analyzed by SDS-PAGE to confirm the presence of the 16-kDa RD3-d.

SDS-PAGE analysis of the collected fractions confirmed the presence of 16-kDa protein and higher molecular weight impurities. To resolve this issue, fractions #5-15 were pooled and diluted five-fold with MQ-H_2O before loading onto a Q anion exchange column. Because the elution of RD3-d had trace amounts of salt in the collected fractions, dilution was necessary to lower the ionic strength and avoid losing protein in the flowthrough waste. The Q-sepharose anion exchange column contains positively charged resins that allow ionic interactions between negatively charged species. Diluted RD3-d is loaded to the column with a salt-free loading buffer C (20 mM Tris-HCl (pH 8.0), 1 mM DTT) and eluted with a gradient from buffer C to a high salt elution buffer D (20 mM Tris-HCl (pH 8.0), 0.5 M NaCl, 1 mM DTT) over 60 minutes at flow rate of 2.0 mL/min. As shown in the chromatogram and SDS-PAGE gel (fig. 2.3.3), the higher molecular weight impurities were no longer detected. Thus, the second purification increased the purity of RD3-d needed for NMR structural analysis.

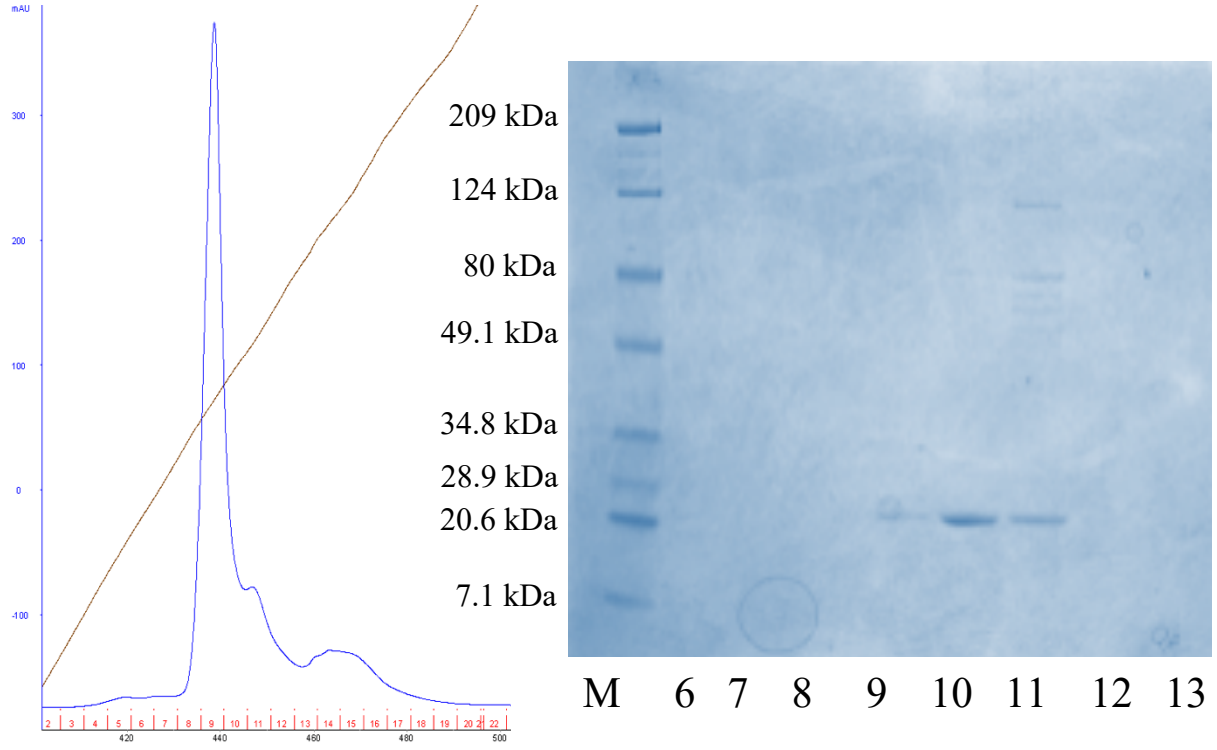

Fig. 2.3.3. Q-sepharose anion exchange chromatogram. Diluted fractions of RD3-d from HIC was loaded onto the column with the absence of salt and eluted at high salt. Fractions #9-11 were analyzed by SDS-PAGE to confirm the presence of the 16-kDa RD3-d.

The second purification was necessary, as shown in fig. 2.3.3, as fractions consisting of RD3-d observed less impurities present. Fraction #12 of the anion exchange chromatogram displayed a trace amount of higher molecular weight impurities that is unfavorable for structural studies. Hence, a final size exclusion chromatography purification was essential to acquire a highly purified sample for NMR.

The final size exclusion chromatography eluted RD3-d as a resolved peak (fig. 2.3.4) and the SDS-PAGE gel analysis confirmed the purity of the sample. Fractions #42-48 showed a 16-kDa band, indicative of RD3-d, and were pooled for NMR sample preparation. The pooled fractions were exchanged in a deuterated NMR buffer and then concentrated to 0.5 – 0.9 mM using an Amicon ultra-15 centrifugal filter unit with a 3-kDa molecular cut off.

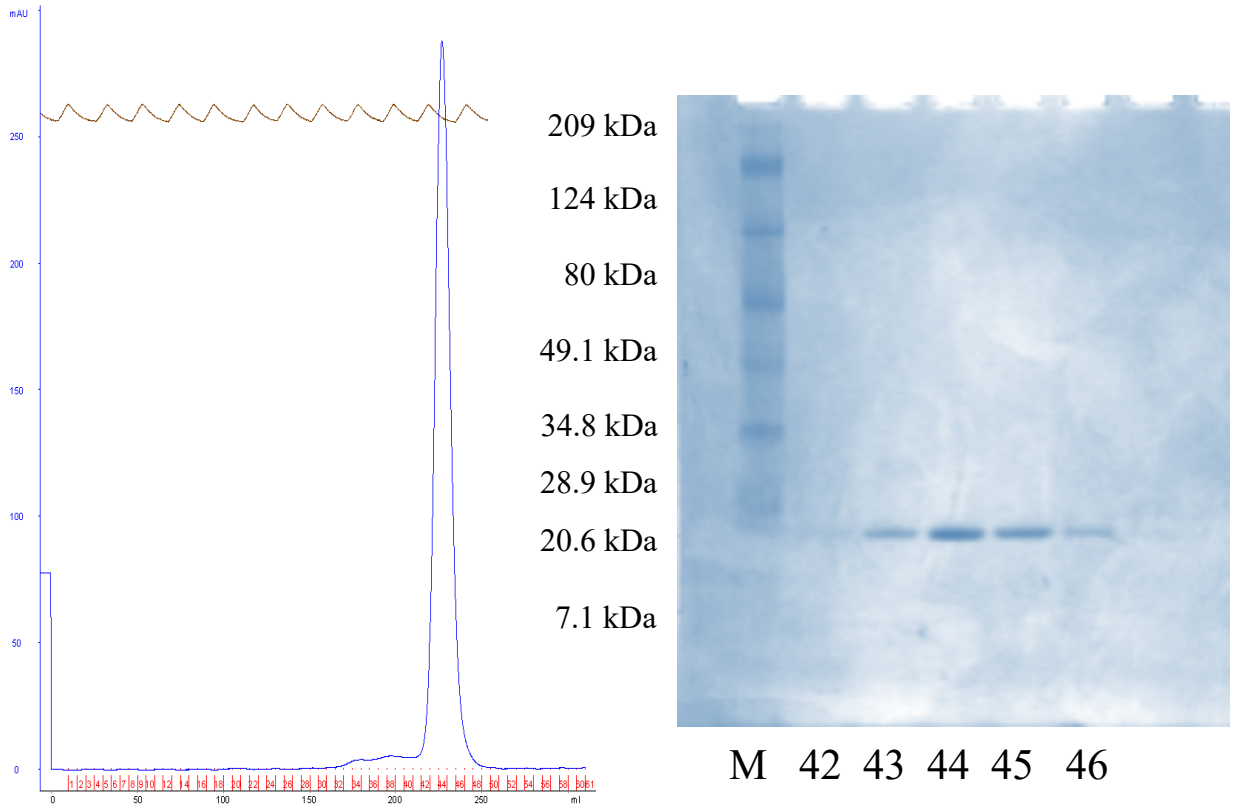

Fig. 2.3.4. Final size exclusion chromatography of RD3-d. Chromatogram shows well-resolved peak eluted from fractions #42-48 and SDS-PAGE gel confirmed high purity of sample with no impurities detected.

Another SDS-PAGE gel analysis that documents the progression of RD3-d protein expression and purification is shown in fig. 2.3.5. In fig. 2.3.5, aliquot samples of the initial lysate, supernatant, urea-solubilized unfolded protein, dialyzed refolded protein, HIC, Q, and SEC fractions illustrates the purification of the 16-kDa protein. The two lysis steps and urea solubilization (as mentioned in 2.2 *Materials and Methods*) was crucial for isolating soluble RD3-d from most of the impurities detected (see fig. 2.3.5.) before it was refolded for further protein purification.

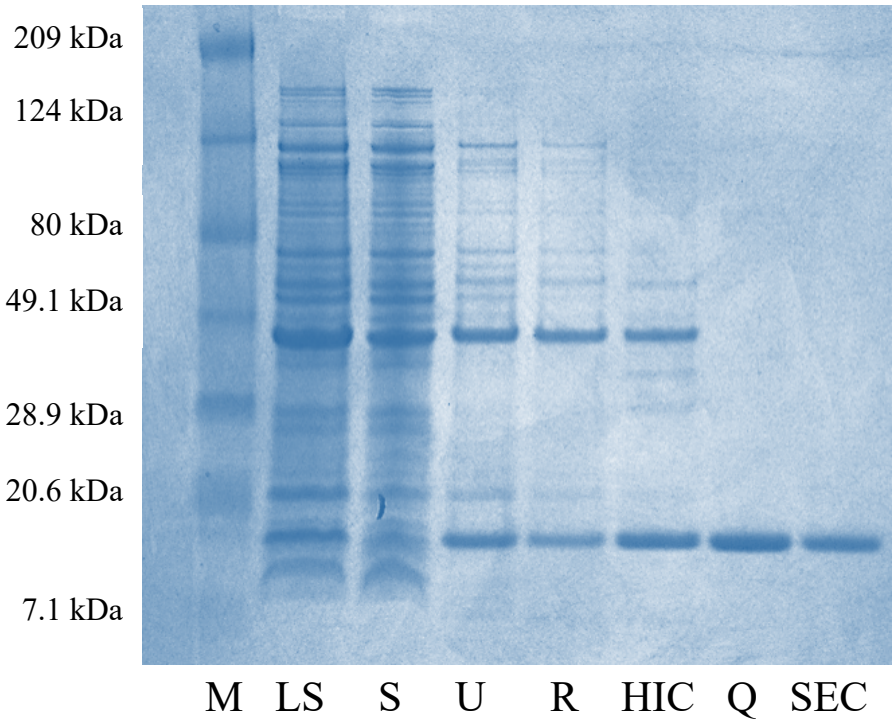

Fig. 2.3.5. SDS-PAGE gel profile of RD3-d expression and purification. LS is initial lysate after first sonication, S is supernatant of second lysis/wash, U is urea-solubilized unfolded RD3-d, R is soluble refolded RD3-d, HIC is pooled fractions #5-8 from hydrophobic interaction column, Q is pooled fractions #9-11 from anion exchange, and SEC is pooled fractions #43-46 from size exclusion.

The isotopically labeled, highly purified, and concentrated RD3-d protein samples prepared by me were then analyzed by NMR. A two-dimensional ^{1}H-^{15}N heteronuclear single quantum correlation (HSQC) spectrum of ^{15}N-labeled RD3-d is shown in Fig. 2.3.6. The ^{1}H-^{15}N HSQC NMR spectrum of RD3-d revealed the truncated variant was stably folded due to uniform intensities and well-dispersed peaks. Therefore, the high quality of the HSQC spectrum of RD3-d demonstrated the feasibility of determining the atomic-resolution NMR structure of RD3-d. Detailed assignments of backbone and sidechain NMR resonances of RD3-d (Fig. 2.3.6) were obtained by Dr. Sunghyuk Lim, and the three-dimensional NMR structure of RD3-d was solved by Dr. Qinhong Yu [75, 88].

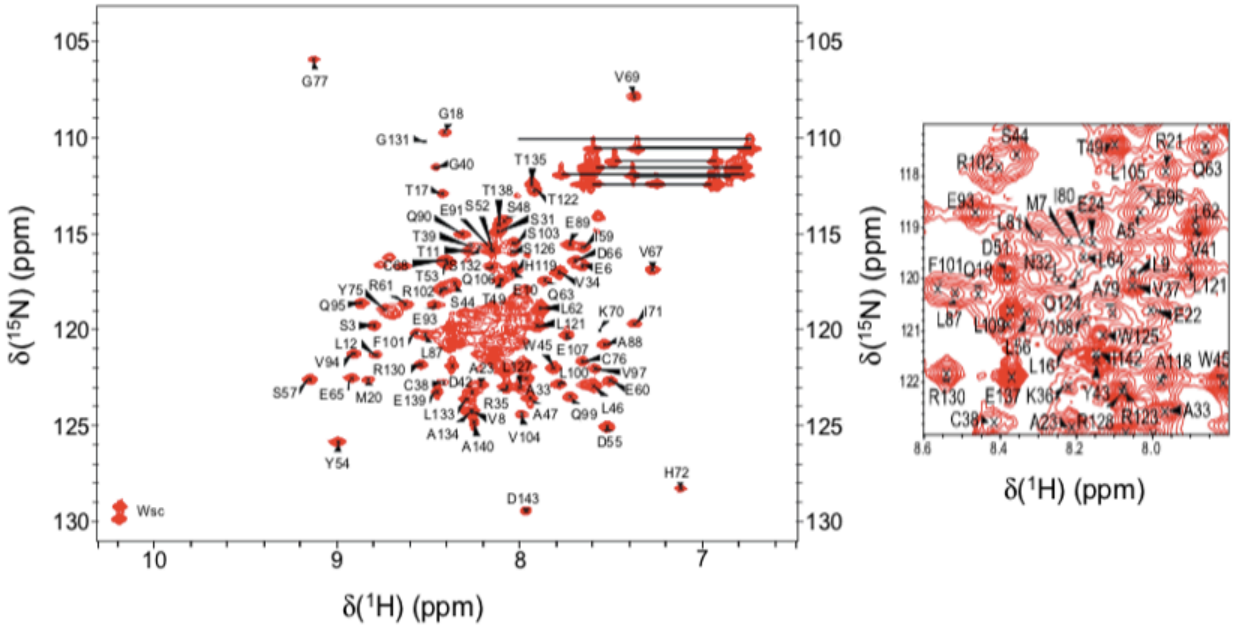

Fig. 2.3.6. Two-dimensional ^{1}H-^{15}N Heteronuclear Single Quantum Correlation (HSQC) NMR spectrum. Well-dispersed peaks and backbone N-H amide assignments labeled. The inset is an expanded view of the spectrally crowded region in the center[86]. Figure modified from (Lim et al, 2017) [86].

More than 86% of the backbone resonances (^{1}HN, ^{15}N, $^{13}C\alpha$, $^{13}C\beta$, and ^{13}CO) and sidechain methyl-resonances were assigned, and the assigned chemical shifts were used to

calculate the secondary structure of RD3-d by TALOS+ [86, 91]. Based on the secondary structure calculation, RD3-d is comprised of a four-helix bundle comprising of two helical hairpins in parallel (fig. 2.3.7A/B) [75, 86].

On the basis of the NMR resonance assignments of RD3-d (BMRB 27305), the three-dimensional NMR structure of RD3-d was calculated based on distance restraints derived from the analysis of NOESY spectra and long-range orientational restraints derived from residual dipolar coupling data as described[75]. The NMR-derived structure of RD3-d was resolved for 141 amino acids, starting at Arg19 and ending at Asp160. The last 20 residues at the C terminus (Arg140–Asp160) are unstructured and dynamically disordered. The 10 lowest-energy NMR structures are overlaid in Fig. 2.3.7A. The overall precision of the NMR ensemble is expressed by a root-mean-square deviation (RMSD) of 0.55 Å calculated from the coordinates of the main-chain atoms. The quality of the NMR structures was assessed using PROCHECK-NMR (25), which shows that 96.8% of the residues occur in the allowed or favorable regions from the Ramachandran plot. RD3-d forms an elongated overall structure (70 Å long by 30 Å wide) with a four-helix bundle (helix α1, Pro21–Val51; helix α2, Pro75–Lys87; helix α3, Pro90–Gln107; and helix α4, Val111–Thr139) shown in Fig. 2.3.7A. Helices α1 and α2 are connected by a long unstructured loop (residues Arg52–Ser74). Helices α1 and α4 are each quite long (27 Å) and interact with one another in an anti-parallel fashion that gives rise to a very long end-to-end distance in the structure. The elongated shape of the RD3-d NMR structure can explain the unusually large radius of gyration observed for RD3 by size exclusion chromatography [75].

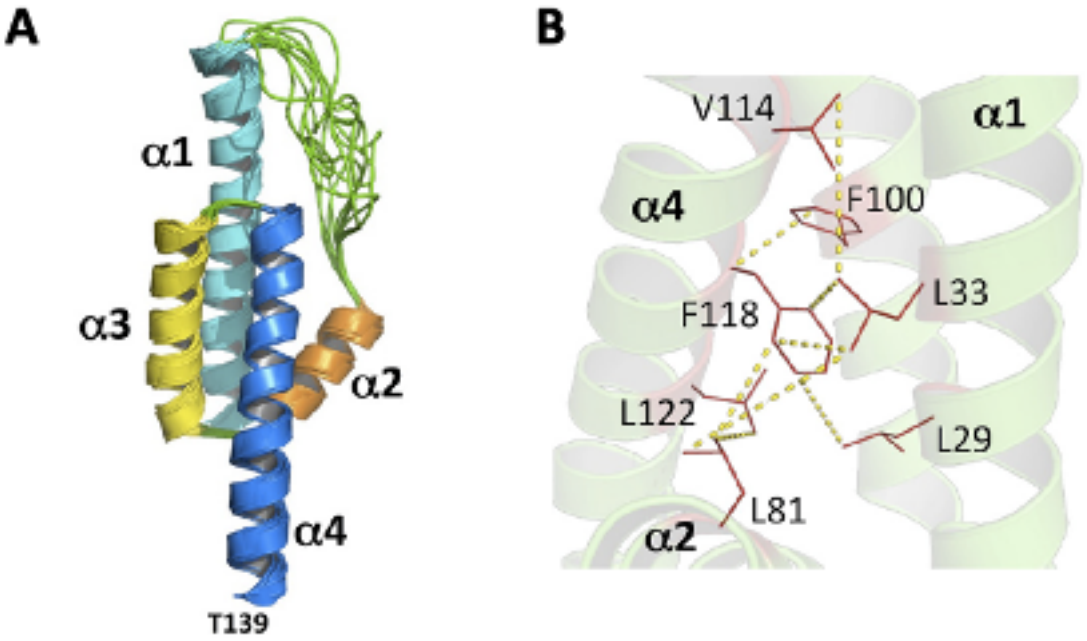

Fig. 2.3.7. NMR structure of RD3-d solved by Dr. Qinhong Yu. (A) Ensemble of 10 lowest energy NMR structures of RD3-d (PDB: 6DRF) solved by Dr. Qinhong Yu. (B) An expansion view of the energized-minimized average structure, highlighting the crucial long-range NOEs that display the hydrophobic interactions within helices responsible for the formation of the four-helix bundle (L29, L33, L81, F100, V114, F118, L122) [75]. Figure previously published in JBC (Peshenko, Yu et al, 2019) DOI: https://doi.org/10.1074/jbc.RA118.006106
https://creativecommons.org/licenses/by/4.0/

Before the NMR structure of RD3-d was known, *Peshenko et al* suggested a potential RetGC-RD3 binding interface located between RD3 residues Lys87 – Leu122 [74]. These RetGC-sensitive residues in RD3 are in discontinuous stretches throughout the amino acid sequence but are spatially close to one another near the center of the NMR structure (highlighted red in Fig. 2.3.8). RD3 residues at each end of the elongated NMR structure (highlighted blue in Fig. 2.3.8) are not essential for the RetGC inhibitory binding [75]. Many of the residues affecting RetGC regulation are solvent-exposed (see His89, Cys93, Pro95, Ile97, Arg99, Arg101, Gln102, and Ser120 in Fig. 2.3.8), consistent with these residues being able to make direct contact with RetGC. By contrast, a few of the RetGC-sensitive residues are buried in the hydrophobic core (Ile88, Ala96, Phe100, and Leu122), suggesting that these residues are inaccessible and must not make

any regulatory contact with RetGC. Future studies are needed to pinpoint and map all the residues on the surface of RD3 that are clustered to form a binding site for RetGC.

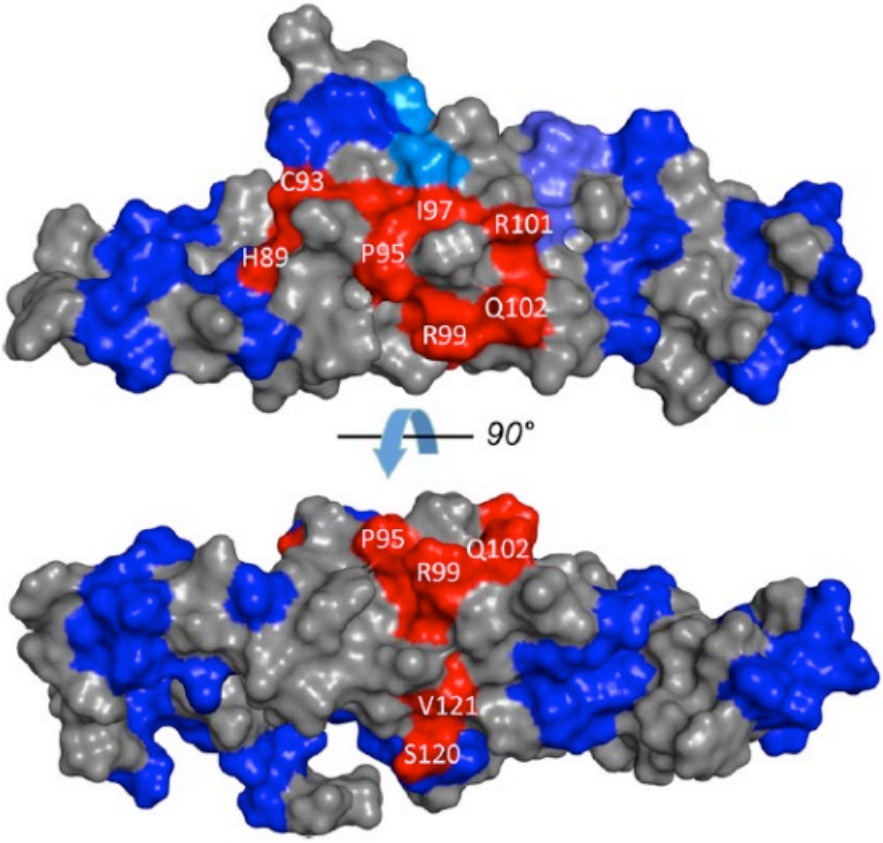

Fig. 2.3.8. RetGC interface maps to the central region of RD3-d. Rd3-d residues (His89, Cys93, Pro95, Ile97, Arg99, Arg101, Gln102, and Ser120) that inhibit RD3 binding to RetGC (red) and those that have no inhibitory effect on cyclase binding (blue)[75]. Figure previously published in JBC (Peshenko, Yu et al, 2019) DOI: https://doi.org/10.1074/jbc.RA118.006106 https://creativecommons.org/licenses/by/4.0/

Chapter 3

NMR and EPR-DEER derived structure of dimeric guanylyl cyclase activating protein-5 (GCAP5)

3.1 Introduction

The visual recovery phase of phototransduction in vertebrate photoreceptors is triggered by the light-induced reduction of second messenger, cGMP that initiates the closure of the cGMP-gated ion channels in light-stimulated photoreceptors. Upon illumination, a key enzyme called PDE6 catalyzes the hydrolysis of cGMP and prevents Ca^{2+} ions from entering into the cells while preserving the outflow of Ca^{2+} by the Na^{+}/Ca^{2+}, K^{+} exchanger [10, 52]. Consequently, the light-induced decrease in cytosolic Ca^{2+} levels are responsible for the Ca^{2+}-sensitive regulation of the key enzyme RetGC by GCAPs [11, 44, 48, 49, 92]. In light-stimulated photoreceptors, Ca^{2+}-free/Mg^{2+}-bound GCAPs bind to RetGC at low Ca^{2+} levels to activate cyclase activity that replenishes cGMP levels required to re-open the ion channels [40, 44]. In contrast, Ca^{2+}-bound/Mg^{2+}-free GCAPs bind to RetGC at high Ca^{2+} levels to turn off the cGMP resynthesis in dark-adapted photoreceptors [41, 72]. Mammalian GCAP1 and GCAP2 were previously shown to bind to RetGC isozymes (*RetGC1* and *RetGC2*) and undergo Ca^{2+}-sensitive conformational changes that allow the reversible switch from activator to inhibitor state [1, 14, 22, 23, 33, 34, 38, 48].

The X-ray crystal structure of Ca^{2+}-bound chicken GCAP1 and the NMR solution structure of Ca^{2+}-free/Mg^{2+}-bound bovine GCAP1 mutant V77E have been previously determined and distinguished a critical structural difference that may be responsible for the Ca^{2+}-dependent regulation of RetGC [53, 59]. The Ca^{2+}-sensitive lengthening of the C-terminal helix (α10) in bovine GCAP1, denoted as the Ca^{2+}-switch helix, at low Ca^{2+} levels is proposed to trigger RetGC activation upon illumination [53]. Thus, Ca^{2+}-dependent conformational changes in GCAPs are critical for RetGC regulation in visual phototransduction.

Additionally, the GCAP proteins contain a covalently attached N-terminal myristoyl group like that observed in recoverin, frequenin and other Ca^{2+}-myristoyl switch proteins that belong to the neuronal calcium sensor (NCS) superfamily [9, 43]. Surprisingly, unlike most NCS proteins, the GCAPs do NOT possess a functional Ca^{2+}-myristoyl switch, and the GCAPs do not exhibit Ca^{2+}-dependent binding to membranes like what is found for the other NCS proteins [43, 52]. A point mutation (D3N) in mammalian and zebrafish GCAP5 was used in this study to enhance the amount of N-terminal myristoylation catalyzed by the yeast (*S. cerevisiae*) N-myristoyltransferase (NMT) that was used for the recombinant expression of myristoylated forms of GCAPs in BL21 *E. coli* cells [52].

Recently, six GCAP homologs (zGCAP1-5, 7) were identified in zebrafish photoreceptors that may differ in Ca^{2+}-binding properties and Ca^{2+}-sensitive regulation of RetGC compared to GCAPs in mammals[88, 93-96]. Interestingly, zGCAP5 is the only homolog that contains two non-conserved cysteine residues (Cys15 and Cys17) that could chelate biologically active transition metals, like Fe^{2+} and Zn^{2+}, and zGCAP5 may have a different function in zebrafish

photoreceptors[88].

Fig. 3.1.1. Sequence alignment of zebrafish GCAPs. zGCAPs are 23-kDa proteins expressed in photoreceptor cells and undergo Ca^{2+}-dependent conformational changes. All GCAPs contain 4 EF-hands highlighted in green, red, cyan, and yellow. Nonconserved cysteine residues (Cys15 and Cys17) in GCAP5 are bolded in red. EF1 is not a functional EF-hand while EF2-4 can bind to Ca^{2+} and Mg^{2+} ions. Swiss Protein Database accession numbers for zGCAP1-5 are Q90WX4, Q90WX3, Q8UUX9, Q6ZM98, AND Q5MAC8, respectively [88]. Figure previously published from (Lim et al, 2017) DOI:10.1021/acs.biochem.7b01029.

Iron binding proteins can adapt to form iron-sulfur (Fe-S) clusters and exist as biological sensors with functional diversity [88, 97]. Ferrodoxin (PDB ID: 5AUI) and rubredoxin (PDB ID: 1FHM) are two iron-sulfur containing proteins that functions as an electron transport protein with different Fe:S stoichiometry [88, 90, 97, 98]. Interestingly, two cysteine residues in zGCAP5 (Cys15 and Cys17) are in close enough proximity to chelate a ferrous ion (Fe^{2+}) and adapt to a Fe_1S_0 stoichiometry, like rubredoxin, to form a Fe^{2+}-bound dimer. The increase in Fe^{2+} levels in the retina has been associated with age-related macular degeneration (AMD), a permanent blinding disorder

observed in human patients over 50 [99]. Analogous to the well-known Ca^{2+} dependent regulation of mammalian RetGC mediated by GCAPs, the presence of Fe^{2+} and zGCAP5 may function as a potential redox sensor in zebrafish phototransduction [88].

Currently, atomic resolution structures are known for the Ca^{2+}-bound forms of GCAP1 and GCAP3, and Ca^{2+}-free/Mg^{2+}-bound GCAP1 V77E mutant [53]. In this chapter, I report an NMR and EPR-DEER derived atomic-level structure of the Ca^{2+}-free/Mg^{2+}bound GCAP5 dimer, which is the first structure of a GCAP protein in a native activator state. I will discuss a potential function of the Fe^{2+}-bound GCAP5 dimer in zebrafish photoreceptor regulation and present the structure of Fe^{2+}-free/Mg^{2+}-bound GCAP5 dimer calculated by a protein-protein docking webserver called High Ambiguity Driven protein-protein Docking (HADDOCK) [43, 55, 62]. Portions of this chapter are adapted with permission from Lim, S.; Scholten, A.; Manchala G.; Cudia, D.; Zlomke-Sell, SK.; Koch, KW.; Ames, JB. *Biochemistry* vol. 56,51 (2017): 6652-6661. Copyright 2017 American Chemical Society. DOI:10.1021/acs.biochem.7b01029

3.2 Materials and Methods

Cloning and Site-directed Mutagenesis of zebrafish GCAP5 (zGCAP5)

Recombinant myristoylated $GCAP5^{D3N}$ WT (henceforth termed as GCAP5, residues 2 - 198) was amplified by PCR and subcloned into pET21 vector to produce soluble GCAP5 exclusive of any affinity tags [52, 88, 94, 96, 100, 101]. A D3N point mutation in GCAP5 was required for a consensus sequence for yeast (*S. cerevisiae*) *N*-myristoyl CoA transferase (NMT) that was used to catalyze the covalent attachment of myristic acid to the N-terminus of GCAP5 [52, 88, 94, 96, 100, 101]. The D3N mutation has no effect on the physiological function of GCAPs [34]. Cloning of all mutants were prepared as described previously, designing primers with point mutations of interest for every

mutant: C15A/C17A, cysless-GCAP5 (hereafter called $GCAP5^{CL}$), all single native and non-native cys $GCAP5^{CL}$, H18E, H18E/Y21E, R22D, M25E, D71E, F72E, V76E, and W93E [52, 88, 94, 96, 100, 101].

Overexpression of Myristoylated GCAP5 and Mutants

Recombinant myristoylated GCAP5 was prepared by a co-expression of the $GCAP5^{D3N}$ and yeast NMT in BL21(DE3) *E. coli* strain [52, 88, 100, 101]. A frozen stock of $GCAP5^{D3N}$ was inoculated in a 20 mL Luria broth (LB) with final concentrations of 100 μg/mL ampicillin (100 mg/mL stock) and 50 μg/mL kanamycin (50 mg/mL stock) and grown for 3-4 hours in a 37°C, 200 rpm shaking incubator before it was inoculated in a 1L M9 minimal media until A_{600} reached 0.7. A final concentration of 10 mg/mL myristic acid in ethanol (10 mg/mL concentrated stock) was added. Protein expression was then induced at A_{600} 0.7 by adding a final concentration of 1 mM isopropyl-β-D-1-thiogalactopyranoside for 5 hours. The bacterial cell pellet was harvested by centrifugation at 6,000 rpm for 20 minutes (Thermo Scientific fixed angle rotor F9-4x1000y) at 4°C and stored in -80°C overnight. GCAP5 mutants were overexpressed in the same manner as described [88, 100].

Purification of GCAP5 by Fast Protein Liquid Chromatography (FPLC)

Myristoylated GCAP5 (and GCAP5 mutants) bacterial cell pellet was resuspended in 25 mL lysis buffer consisting of 20 mM Tris-HCl (pH 8.3), 2 mM ethylene glycol-bis(β-aminoethyl ether)-N,N,N',N'-tetraacetic acid (EGTA), 1 mM dithiothreitol (DTT), 0.1 M KCl, 10% glycerol and 0.1 mM phenylmethylsulfonyl fluoride (PMSF). The bacterial lysate was then sonicated on ice for 2 min (output = 3 with 2 min cooling interval) and repeated until it is no longer viscous. The soluble protein was isolated from debris by ultracentrifugation at 35K rpm for 1.5 h at 4°C in a fixed T1250 rotor. A final concentration of 0.35 M ammonium sulfate was added to GCAP5 to

increase solubility before FPLC protein purification. GCAP5 was purified by hydrophobic interaction Butyl-Sepharose, anion exchange (HiTrap Q HP, GE Healthcare), and size exclusion Superdex-200 column chromatography as described previously [88, 100, 101]. Myristoylated GCAP5 was purified to be more than 95% pure analyzed by SDS-PAGE [88, 100, 101]. Finally, the regulation of RetGC by zGCAP5 (and zGCAP5$^{C15A/C17A}$) in the presence of 100 μM Fe^{2+} was recorded by *in vitro* guanylate cyclase (GC) assays, as described previously, by collaborator Dr. Karl-W. Koch (University of Oldenburg, Oldenburg, Germany) [88].

Analytical Size Exclusion Chromatography (SEC)

The molar mass of purified zGCAP5 WT was initially measured by using an analytical SEC (Superdex 200 HR 10/30, GE Healthcare) [18, 88]. Experiments were performed at 4°C and SEC column was pre-equilibrated with buffer consisting of 30 mM MES (pH 6.5), 5 mM citrate (for Fe^{2+} studies) , and 100 mM NaCl [88]. 100 μL samples of GCAP5 WT and GCAP5$^{C15A/C17A}$ in the presence of Mg^{2+} (5 mM) or Fe^{2+} (1 mM) were concentrated to 200 μM before being manually loaded onto the column with an elution flow rate of 0.5 mL/min [88]. Then, the apparent molar mass of GCAP5 samples were calculated based on a standard curve of elution volume (V_e)/void volume (V_0) *versus* the calculated log of known molecular weights of the following protein standards (Fig. 3.3.4): cytochrome C (12 kDa), carbonic anhydrase (29.2 kDa), albumin (66.5 kDa), and alcohol dehydrogenase (82 kDa) [88, 101].

Isothermal Titration Calorimetry (ITC)

ITC experiments were performed using a MicroCal VP-ITC microcalorimeter to measure binding of Fe^{2+} to metal-free samples of GCAP5 WT and GCAP5$^{C15A/C17A}$ [88]. First, purified protein samples were treated with 5 mM EGTA to chelate Ca^{2+} contaminants. The removal of excess EGTA was done by dialysis, exchanging decalcified protein samples in ITC titration buffer

containing 30 mM MES (pH 6.5), 100 mM NaCl, and 1 mM BME. Fe^{2+} titrant consisted of 2 mM ferrous gluconate in ITC titration buffer. Concentration of GCAP5 samples was 50 μM and 2 mM Fe^{2+} titrant. ITC experiments were executed at 25°C on 50 μM GCAP5 samples titrated with 40 incremental additions of 5 μL Fe^{2+} titrant (2 mM stock) [88] .The binding isotherm calculated was generated to calculate the binding affinity (K_d), enthalpy changes (ΔH), and binding stoichiometry/molar ratio of the ligand and protein (Fig. 3.3.3) [18, 88, 102].

NMR Spectroscopy

Myristoylated GCAP5 WT and yeast *N*-myristoyl CoA transferase (NMT) were first co-expressed in *E. coli* and grown in isotope-labeled M9 minimal media with ^{15}N-labeled NH_4Cl and/or ^{13}C-labeled glucose to produce isotope-labeled protein needed for two- and three-dimensional NMR structural studies [88, 100, 101]. Uniformly ^{15}N-labeled and ^{13}C, ^{15}N-labeled samples of myristoylated Mg^{2+}-bound $GCAP5^{D3N}$ and mutants were exchanged into an NMR buffer comprising of 5 mM MES (pH 6.5), 3 mM dithiothreitol-d_{10} (DTT-d_{10}), 2-5 mM $MgCl_2$, 0.04% w/v NaN_3, and 93% H_2O/7% D_2O and had a final concentration between 0.5 – 0.9 mM [100, 101].

All NMR experiments were performed at 23°C on a Bruker Avance 600 MHz spectrometer with a four-channel interface and triple resonance cryogenic (TCI) probe [88, 100, 101]. Assignments of backbone resonances were acquired by performing and analyzing the following two- and three-dimensional spectra: HNCA, HNCACB, CBCA(CO)NH, and HNCO [100, 101]. In addition, assignments of sidechain resonances that assist in three-dimensional structural elucidation were obtained from the following spectra analysis: HCCH-TOCSY, CCCONH, HCCCONH, ^{13}C-edited NOESY, ^{15}N-edited NOESY and TOCSY, and CT-HSQC [100, 101]. A detailed explanation of assigning backbone and sidechain resonance of GCAP5 are provided below (*3.3 Results)*.

Residual Dipolar Coupling (RDC) by NMR analysis

Residual dipolar coupling (RDC) are important structural restraints in protein NMR that provide information on the three-dimensional structure of the protein by using the alignment of backbone amides (^{1}H-^{15}N) in secondary structure calculated relative to the magnetic field (B_0) [103]. To prevent protein from tumbling in solution, a filamentous bacteriophage *Pf1* (Asla Biotech Ltd., Latvia) was added to a ^{15}N-labeled GCAP5 (0.5 mM) sample to serve as an orienting medium and generate a weak alignment relative to the magnetic field [103].

First, *Pf1* (0.5 mL) was added resuspended in 2 mL MES NMR buffer (described previously) and spun at 50,000 rpm for 2 hours at 4°C (AH-650, swing rotor). *Pf1* pellet was then resuspended in 2 mL MES NMR buffer and ultracentrifuged was repeated once. Concentration of *Pf1* was calculated by UV-Vis at 270 nm and a final concentration of 12 mg/mL *Pf1* was added to ^{15}N-labeled GCAP5 for NMR analysis. Backbone ^{1}H-^{15}N RDC constants (D_{NH}) were recorded from a two-dimensional IPAP (inphase/antiphase) ^{1}H-^{15}N HSQC and RDCs were calculated as the difference in ^{15}N-splitting for every amide resonance in the presence and absence of phage *Pf1* [104]. Reported RDC Q-factor and RDC analysis were validated by PALES [105].

NMR Titration of Fe^{2+} Binding to GCAP5

For NMR titration studies, GCAP5 WT and GCAP5$^{C15A/C17A}$ samples with incremental additions of $FeSO_4$ was prepared anaerobically by Dr. Sunghyuk Lim as described previously [88]. ^{1}H-^{15}N HSQC NMR spectra of Fe^{2+}-bound GCAP5 WT (and GCAP5$^{C15A/C17A}$) were collected with 0, 0.25, 0.50, 1.0, 2.0, and 5.0 equivalence of $FeSO_4$ and overlaid for NMR titration analyses [88]. All NMR spectra were processed using NMRPipe and probed using Sparky NMRFAM software [88, 89, 100, 101, 106].

NMR Assignments

The sequential backbone assignments were obtained based on the following NMR spectra: ^{1}H-^{15}N HSQC, HNCO, CBCA(CO)NH, HNCA and HNCACB [100]. First, HSQC peaks were manually picked, and then the C-terminal residue of GCAP5 was assigned as a reference. Relative to the reported chemical shifts of every amino acid residue, the assigned ^{1}H-^{15}N chemical shifts (ppm) of the C-terminal residue was matched in all acquired triple-resonance spectra and then aligned. From there, backbone chemical shifts (Hα, Cα, Cβ, CO, ^{15}N and HN) were assigned using HNCA, HNCACB, CBCA(CO)NH, and HNCO spectra.

For instance, HNCACB triple-resonance spectra identifies the ^{13}C chemical shifts of Cα and Cβ resonances that are correlated to the selected ^{1}H-^{15}N peak representing one residue (*i*, stronger intensity) and the previous residue (*i*-1, weaker intensity). Fig. 3.2.1 shows the GCAP5 amino acid sequence and sequential backbone assignment strategy. Sequential backbone assignments were repeated to find unique segments within the sequence and every residue was connected one by one until the completion of backbone assignments. In HNCACB, there are 3-4 ^{13}C peaks in a ^{15}NH strip where Cα (and $C\alpha_{i-1}$) and Cβ (and $C\beta_{i-1}$) are opposite signs [24, 25, 107-109]. A common technique in NMR assignments is to identify unique *i* residues, like glycine, alanine, serine and threonine, and match the weaker intensities (*i*-1) based on reported average chemical shifts [24, 25, 107-109]. Glycine is unique as it only has a single $^{13}C\alpha$ resonance at 45 ppm chemical shift and does not overlap with other residues [24, 25, 107-109]. Fig. 3.2.1b shows the process of assignments D105 – C105 in HNCACB spectra analysis. In the G104 ^{15}NH strip, glycine has a $^{13}C\alpha$ resonance at 45 ppm (strong intensity) and contains two weaker peaks with a distinct chemical shift pattern belonging to either a serine or threonine ($^{13}C_{\beta}$ resonances are more downfield due to the side-chain OH group and occur at higher ppm). After confirmation of previous residue (*i*-1) belonging to

serine (fig. 3.2.1b), the assigned Cα and Cβ chemical shifts of serine is set as the *i* residue and is matched to stronger intensities equivalent in a different ^{15}NH strip. Analysis of *i*-1 chemical shifts are repeated until a unique oligopeptide is assigned to a unique region in the GCAP5 sequence as shown in fig. 3.2.1. This process can be done reversibly (previous and forward) and is exhaustively repeated across all triple-resonance NMR spectra until remaining peaks are assigned. Using this approach, I assigned 86% of the backbone resonances and the remaining 14% could not be assigned due to spectral overlap.

MGDSSSMSAT ELSACKCHQW YRKFMTECPS GQLTFYEFKK FFGLKNKSEK
SNAYVNTMFK TFDIDDDGCI DFMEYVAALS LVLKGGVQQK LRWYFKLFDM
DGSGCIDKDE LLLIFKAVQA INGAEPEISA EDLADIVFNK IDVNGDGELS
LEEFMEGISA DEKISEMLTQ SLDTRIVSN IYNDSYIEQE AEIIEDQA

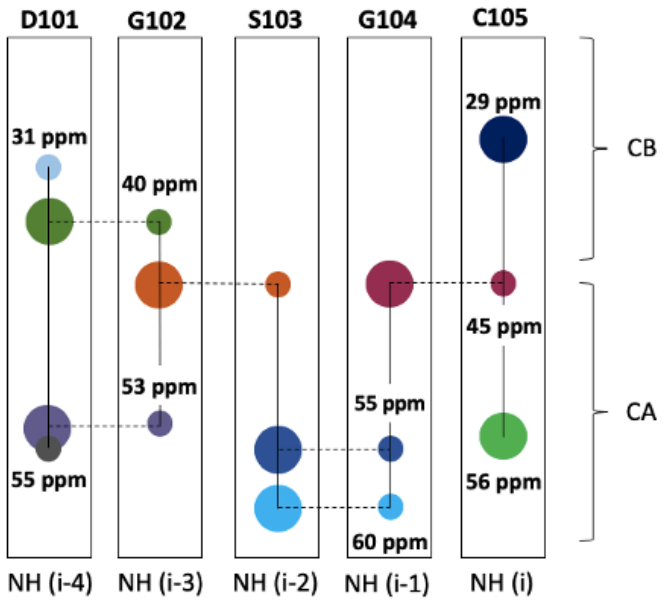

Fig. 3.2.1. (A) GCAP5 amino acid sequence with highlighted C15/C17 in bold red. (B) Representative figure of D101 – C105 sequential backbone assignment process in HNCACB NMR spectra.

Once sequential assignments have been finalized, assignments of non-aromatic residues with hydrophobic sidechains are critical information to determine short to long-range distance restraints between residues for the three-dimensional structure of a protein [24, 25, 107-109]. The Nuclear

Overhauser Effect (NOE) is the rate of magnetization through space by which NOEs are observed between protons of residues that may be far apart in sequence but within 5 Å in space [24, 25, 107-109]. Terminal methyl resonances are key information to acquire long-range NOEs. Sidechain assignments are identified by the following triple-resonance spectra: HCCH-TOCSY, CCCONH, HCCCONH, ^{13}C-edited NOESY, ^{15}N-edited NOESY and TOCSY, and CT-HSQC [24, 25, 107-109]. CCCONH and HCCONH are triple-resonance spectra that comprise of sidechain resonances; however, a fraction of resonances in GCAP5 samples were broadened by detection due to the spectra's low sensitivity. HCCH-TOCSY analysis couples all C-H belonging to one residue and their previous backbone assignments of Cα/Hα and Cβ/Hβ assists in finding the ^{1}H-^{13}C strip plot. For instance, fixating the spectrum at V55 Cα and V55 Hα identified at the diagonal cross-peak will provide other resonances belonging to assigned Hβ and sidechain Hγ1/ Hγ2 as shown in fig. 3.2.2a. To find Cγ1/Cγ2, locating the new Hγ1/ Hγ2 of V55 as a cross-peak coupled with stereospecific ^{1}H-^{13}C HSQC will identify Cγ1-Hγ1 and Cγ2-Hγ2. Leucine and valine can be identified and assigned on ^{1}H-^{13}C HSQC as Leu Cδ1 and Val Cγ1 have an opposite phase from Leu Cδ2 and Val Cγ2 (fig. 3.2.2b).

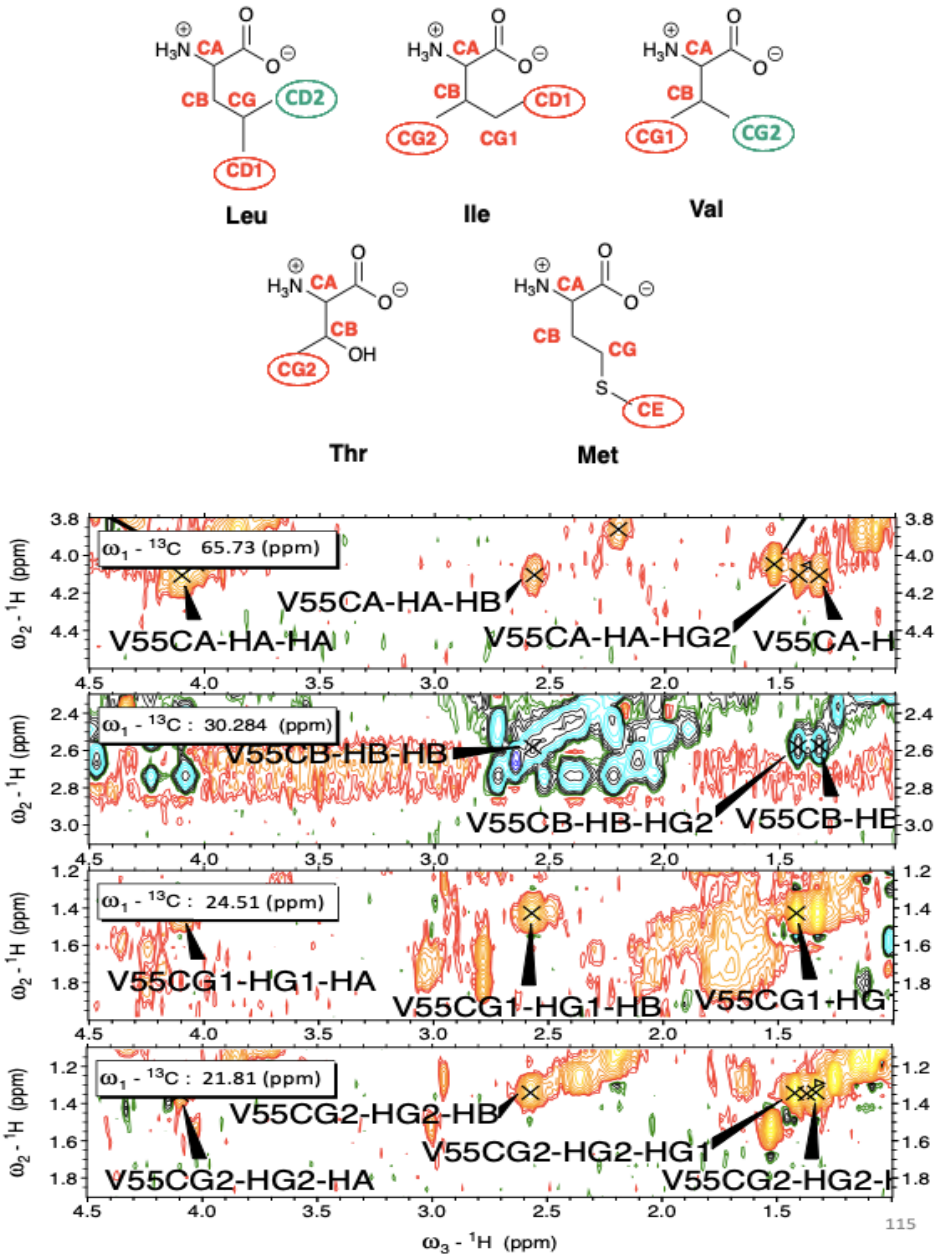

Fig. 3.2.2. Sidechain assignment and stereospecific sidechain residues. (A) Non-aromatic residues with stereospecific sidechains detected by ^{1}H-^{13}C HSQC. (B) V55 sidechain assignment process utilizing prior knowledge of backbone Cα/Hα and Cβ/Hβ assignments to identify sidechain resonances (Cδ1, Cδ2, Cγ1, Cγ2, Hδ1, Hδ2, Hγ1, Hγ2) [100, 101].

Extent of Myristoylation in GCAP5 by LC-MS and NMR Analyses

Heterogeneity was observed in all GCAP5 samples and caused NMR peak broadening due to extraneous resonances. To determine whether the sample heterogeneity might be caused by

incomplete protein myristoylation, samples of myristoylated (with pBB131-NMT) and unmyristoylated GCAP5 (lacking pBB131-NMT) were prepared to send off to the mass spectrometry facilities for liquid chromatography mass spectroscopy (LC-MS) analysis by Dr. William Jewell (UCD, Davis, CA). ^{1}H-^{15}N HSQC spectra of ^{15}N-labeled myristoylated and unmyristoylated GCAP5 were recorded separately and overlaid to detect any notable differences.

NMR Structure Calculation by Xplor-NIH

The NMR solution three-dimensional structure of a Ca^{2+}-free/Mg^{2+}-bound myristoylated $GCAP5^{D3N}$ activator was calculated based on acquired dihedral angles from TALOS+, NOEs, backbone hydrogen bonds, and RDCs as structural distance restraints [91, 110]. NMR-guided structures were calculated using these structural restraints and implemented in restrained molecular dynamics simulations within Xplor-NIH [101, 111]. First, backbone chemical shifts (Hα, Cα, Cβ, CO, ^{15}N and HN) were assigned by NMR and utilized to measure dihedral angles by TALOS+ [91, 110]. Terminal side-chain methyl and aromatic resonances were assigned by utilizing HCCH-TOCSY, CCCONH and HCCCONH NMR spectra to aid in acquiring NOEs distance restraints from ^{15}N-edited NOESY-HSQC and ^{13}C-edited NOESY-HSQC [100]. The template structure of the Xplor-NIH calculations was the Ca^{2+}-free/Mg^{2+}-bound myristoylated GCAP5 homology (based on x-ray crystal structure of bovine Ca^{2+}-bound GCAP1, PDB ID: 2R2I) calculated using SWISS-MODEL. A total of 500 structures in refinement were calculated and the final 10 structures were selected to produce an energy-minimized average structure. The final structures were then deposited to RCSB PDB (PDB ID: 7M2M) and structure quality was assessed by PROCHECK-NMR and MolProbity [100, 101, 112]. The structural statistics are shown in Table 3.3.1 (*3.3. Results*).

Spin Labeling for EPR-DEER Sample Preparation

Apo-myristoylated GCAP1^{V77E} (and DEER mutants: T29C, E57C, E133C and E154C) and GCAP5^{CL} (and DEER mutants: A15C, A17C, T26C, A28C, N56C, A69C, A105C, N139C, E152C, E156C and S159C) were first dialyzed against 4 L dialysis buffer in 20 mM Tris-HCl (pH 7.4) with 100 μM tris(2-carboxyethyl)phosphine (TCEP) overnight at 4°C [62, 101]. A 40 mM stock solution of the spin-label (1 oxyl 2,2,5,5-tetramethyl-Δ3-pyrroline-3-methyl) methanethiosulfonate (termed MTSSL, Toronto Research Chemicals Inc., Toronto, Canada) was prepared by dissolving in dimethylsulfoxide (DMSO). The dialyzed protein was adjusted to 10-20 μM before the addition of excess MTSSL was added to protein at a 30:1 molar ratio. The reaction was performed on ice for 30 min and then unreacted MTSSL was dialyzed away against 4 L dialysis buffer in 20 mM Tris-HCl (pH 7.4) at 4°C for 4-6 hours. Dialysis was repeated once again with 4 L fresh dialysis buffer overnight at 4°C. The spin-labeled protein was concentrated to a final concentration of ~300 μM by using an Amicon ultra-15 centrifugal filter unit with a 10-kDA molecular weight cut off. The final spin-labeled protein was then exchanged three times into deuterated DEER buffer containing 10 mM Tris-d_{11} (pH 7.4), 2 mM $MgCl_2$ and 99.9% D_2O. The sample was sent to collaborators Dr. Graham P. Roseman and Dr. Tufa E. Assafa in the Dr. Glenn Milhauser lab (UCSC, Santa Cruz, CA) and 25% glycerol-d_8 was added to the protein as a cryo-protectant before freezing [62, 101]. All EPR-DEER measurements were performed by collaborators at Dr. Glenn Milhauser lab (UCSC, Santa Cruz, CA) for both GCAP1^{CL} and GCAP5^{CL} mutants as described previously [62, 101].

Molecular Docking of GCAP5 Dimerization by HADDOCK

The dimeric structure of Fe^{2+}-free/Mg^{2+}-bound GCAP5 was calculated based on EPR-DEER distance restraints and uploaded onto a protein-protein (or protein-ligand) docking HADDOCK webserver [113]. The NMR solution structure of monomeric Mg^{2+}-bound GCAP5 (Fig. 3.3.11) was docked with itself and the measured EPR-DEER intermolecular distance restraints were applied to the docking calculation [101, 113]. The EPR-DEER distance restraints were classified as unambiguous and a margin error of ±5 Å was applied for every restraint (*shown in Table 3.3.2*) [101]. First, the calculation generated 1000 structures via rigid body energy minimization. Then, the best 200 structures moved forward to a semi-flexible simulated annealing and later subjected to refinement in explicit waters [101, 113]. The final 200 water refined structures were categorized in 12 clusters and the coordinate file with the lowest interface RMSD (i-RMSD) was selected for the final dimeric model in this study [101].

Multi Angle Light Scattering (MALS)

GCAP5 (and mutants) samples were loaded to a (1) size-exclusion chromatography (SEC) column or (2) syringe-pump (batch-mode) and coupled to a multi-angle light scattering (MALS) instrument. The MALS miniDawn instrument equipped with a 690-nm laser (Wyatt Technologies, Inc.) was connected to a refractive index instrument, through which the MALS instrument records the observed light scattering intensity and differential refractive index data of the sample of interest.

An analytical SEC column (Superdex 200 HR 10/30, GE Healthcare) was pre-equilibrated 4°C in buffer containing 20 mM Tris-HCl (pH 7.4), 0.1 M NaCl, and 1 mM DTT. A 1.0 mL concentrated GCAP5 (and mutants) sample was manually loaded onto the column and eluted at a flow rate of 0.5 mL/min. Then, data analysis was processed using the ASTRA software (Wyatt

Technologies, Inc.) and molar mass of GCAP5 (and mutants) was calculated based on a Zimm plot analysis with a refractive index increment (dn/dc = 0.185 L/g) [101, 114, 115].

3.3 Results

Function of Fe^{2+}-bound GCAP5 in Zebrafish Photoreceptors

Although an increase in Fe^{2+} levels in the retina are correlated to macular degeneration (AMD), the function of GCAP5 in the presence of Fe^{2+} was investigated to determine the importance of the two non-conserved cysteine residues (Cys15 and Cys17) [88]. Our collaborator Dr. Karl W. Koch (University of Oldenburg, Oldenburg, Germany) performed *in vitro* functional analysis to quantify the cyclase activity relative to cGMP levels produced [88]. Because active recombinant zebrafish photoreceptor guanylyl cyclases (zGCs) were not available at the time, Dr. Koch's functional studies were focused instead on recombinant mammalian GCs (GC-E) enzyme activity in the presence of bovine GCAP1 and zGCAP5 (and zGCAP5$^{C15A/C17A}$).

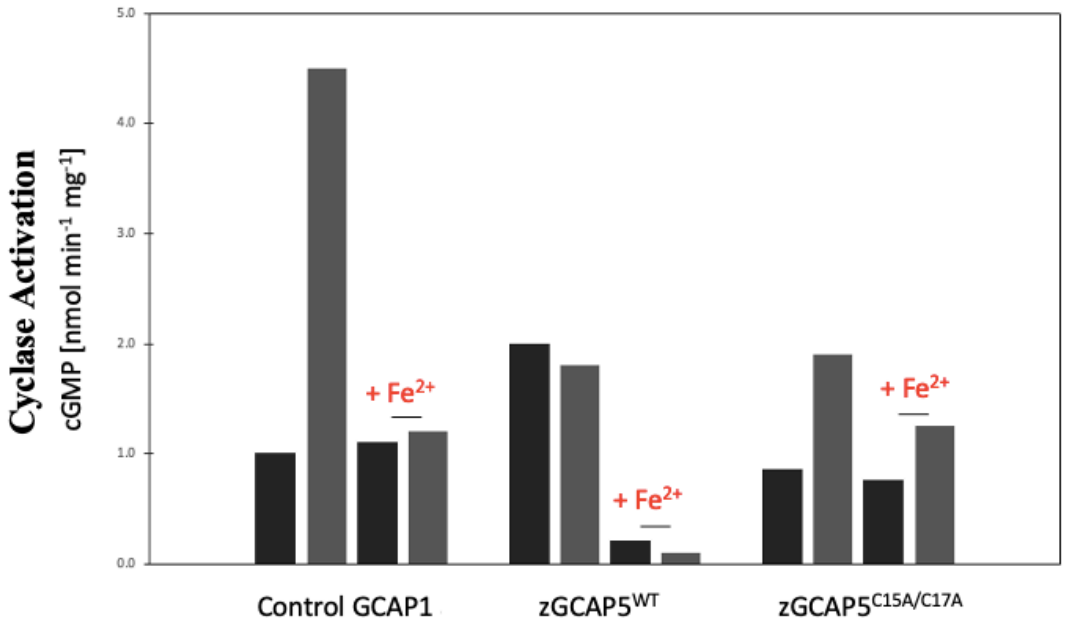

Fig. 3.3.1 *in vitro* guanylate cyclase (GC-E) assay determines Fe^{2+}-bound GCAP5 as GC-inhibitor. Black bars represent GCAP samples in the presence of 1.5 µM free Ca^{2+} and gray bars show data for GCAP samples in the presence of <10 nM free Ca^{2+} due to presence of EGTA.

Addition of 100 nM Fe^{2+} was added to GCAPs (+ Fe^{2+}). Presence of Fe^{2+} in GCAP5 WT decreased the enzyme activity 10x-fold while $GCAP5^{C15A/C17A}$ had an insignificant effect on enzyme activity [88]. Figure modified and previously published from (Lim et al, 2017) DOI:10.1021/acs.biochem.7b01029.

The effects of GCAP1 and GCAP5 on guanylyl cyclase activity are shown in Fig. 3.3.1. As a positive control, Fe^{2+}/Ca^{2+}-free GCAP1 was shown to cause about 5-fold activation of cyclase activity at Ca^{2+} levels below 10 nM (gray bar in left panel of Fig. 3.3.1), whereas the cyclase activity is reduced 5-fold by Ca^{2+}-bound GCAP1 at Ca^{2+} levels at or above 1.5 micromolar (black bar in left panel of Fig. 3.3.1). The addition of 100 nM Fe^{2+} in the presence of Ca^{2+}-free GCAP1 reduces the cyclase activity like that of Ca^{2+}, suggesting that Fe^{2+} can bind to the EF-hands of GCAP1 and mimic Ca^{2+} binding. Indeed, Fe^{2+} binding to GCAP proteins measured by isothermal titration calorimetry (see Fig. 3.3.3) and NMR titrations indicate that Fe^{2+} does indeed bind to the second and third EF-hands of both GCAP1 and GCAP5 [88]. However, GCAP1 binds to Ca^{2+} with about 100-fold higher affinity compared to that of Fe^{2+}, which explains why the presence of 100 nM Fe^{2+} has no effect on cyclase activity in the presence of Ca^{2+}-bound GCAP1 (Fig 3.3.1). By stark contrast, GCAP5 can bind to Fe^{2+} even in the presence of saturating Ca^{2+} levels, because the presence of Fe^{2+} caused a more than 10-fold decrease in GC-E catalytic activity in the presence of Ca^{2+}-bound GCAP5. This result suggests that Fe^{2+} may bind to a separate site on GCAP5 (Cys15 and Cys17) that is outside of the EF-hands. To test this possibility, a GCAP5 double mutant was constructed in which the two cysteines (Cys15 and Cys17) were replaced with alanine (called $GCAP5^{C15A/C17A}$) to abolish Fe^{2+} binding to these cysteines. As predicted, this double mutant abolishes the Fe^{2+}-induced inhibition of cyclase activity that was observed in the presence of wild type GCAP5. Thus, the two cysteine residues (Cys15 and Cys17) are essential for the Fe^{2+}-induced inhibition of cyclase activity caused by GCAP5.

Fe^{2+} binding to GCAP5 was first detected by a faint yellow color in a highly purified GCAP5 sample [88]. This yellow color suggested the possible formation of an iron-sulfur cluster in GCAP5 that could be detected by ultraviolet-visible (UV-vis) absorption spectroscopy of GCAP5. In the presence of Fe^{2+}, GCAP5 WT exhibited an absorbance at 325 and 420 nm indicative of an iron-sulfur cluster (fig. 3.3.2) [88, 116]. Fig. 3.3.2 presents the absorbance spectrum of GCAP5 $^{C15A/C17A}$ double mutant with no detectable absorbance at 325 nm, suggesting Cys15 and Cys17 are important residues to form the iron-sulfur cluster in GCAP5 as a cyclase inhibitor [88].

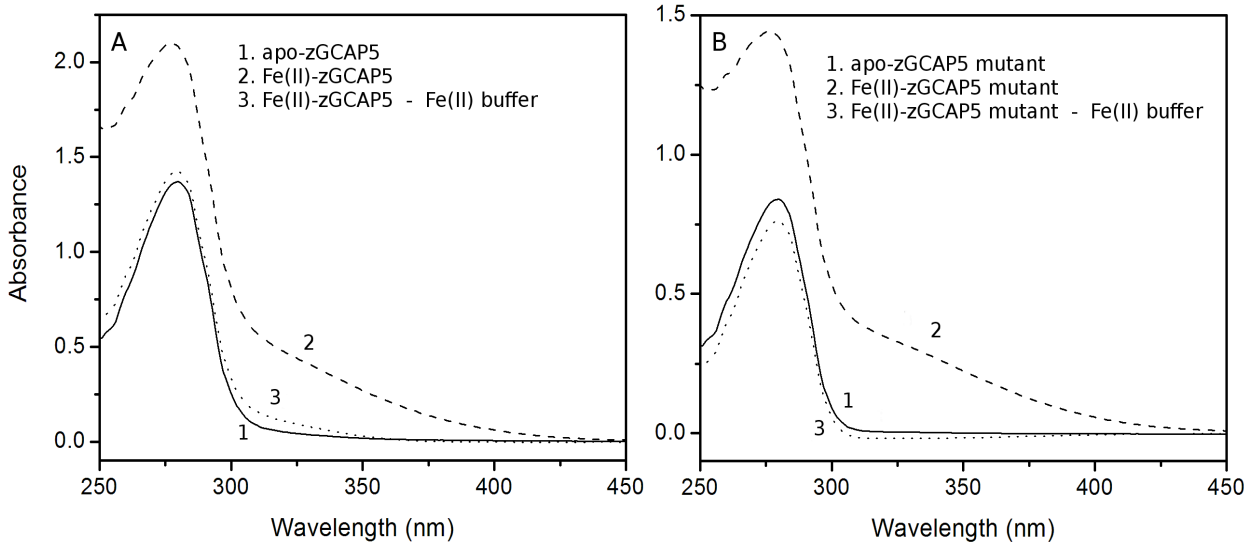

Fig. 3.3.2. UV-vis absorbance spectrum to detect iron-sulfur cluster formed by C15/C17. GCAP5 WT observed a positive absorbance difference at 325 nm corresponding to an iron-sulfur cluster (left). GCAP5$^{C15A/C17A}$ double mutant disables C15/C17 binding to Fe^{2+} with no detectable change in absorbance, suggesting no iron-sulfur cluster formed (right).

Fe^{2+} Binding to GCAP5 Measured by Isothermal Titration Calorimetry (ITC)

After confirming a functional role of Fe^{2+} in GCAP5, the binding of Fe^{2+} to GCAP5 was quantitatively measured by ITC. Incremental titration of Fe^{2+} to GCAP5 WT (and GCAP5$^{C15A/C17A}$) resulted in a binding isotherm that allowed calculation of the dissociation constant (K_d), binding site(s), stoichiometric ratio of at least two Fe^{2+} bound per GCAP5, and the changes in enthalpy (ΔH) measured by ITC at 25°C (fig. 3.3.3.) [88]. In fig. 3.3.3B, the binding

isotherm of GCAP5 WT was multiphasic and detected two distinct binding sites. The first binding site is a high-affinity site of Fe^{2+} (K_d < 100 nM) with a stoichiometric ratio (*n*) of 1 Fe^{2+} ion per GCAP5 dimer (or 0.5 Fe^{2+} per GCAP5 monomer) [88]. Moreover, the GCAP5 wild-type binding isotherm had a separate lower affinity site of Fe^{2+} (K_d 3 ± 1 μM) with *n* = 2 ± 0.5 of Fe^{2+} per GCAP5 monomer (fig. 3.3.3B) [88]. The lower affinity binding of Fe^{2+} most likely represents Fe^{2+} binding to the EF-hands in GCAP5, because mutations in EF2 and EF3 that disable Ca^{2+} also eliminate the low affinity Fe^{2+} binding (Karl Koch, unpublished).

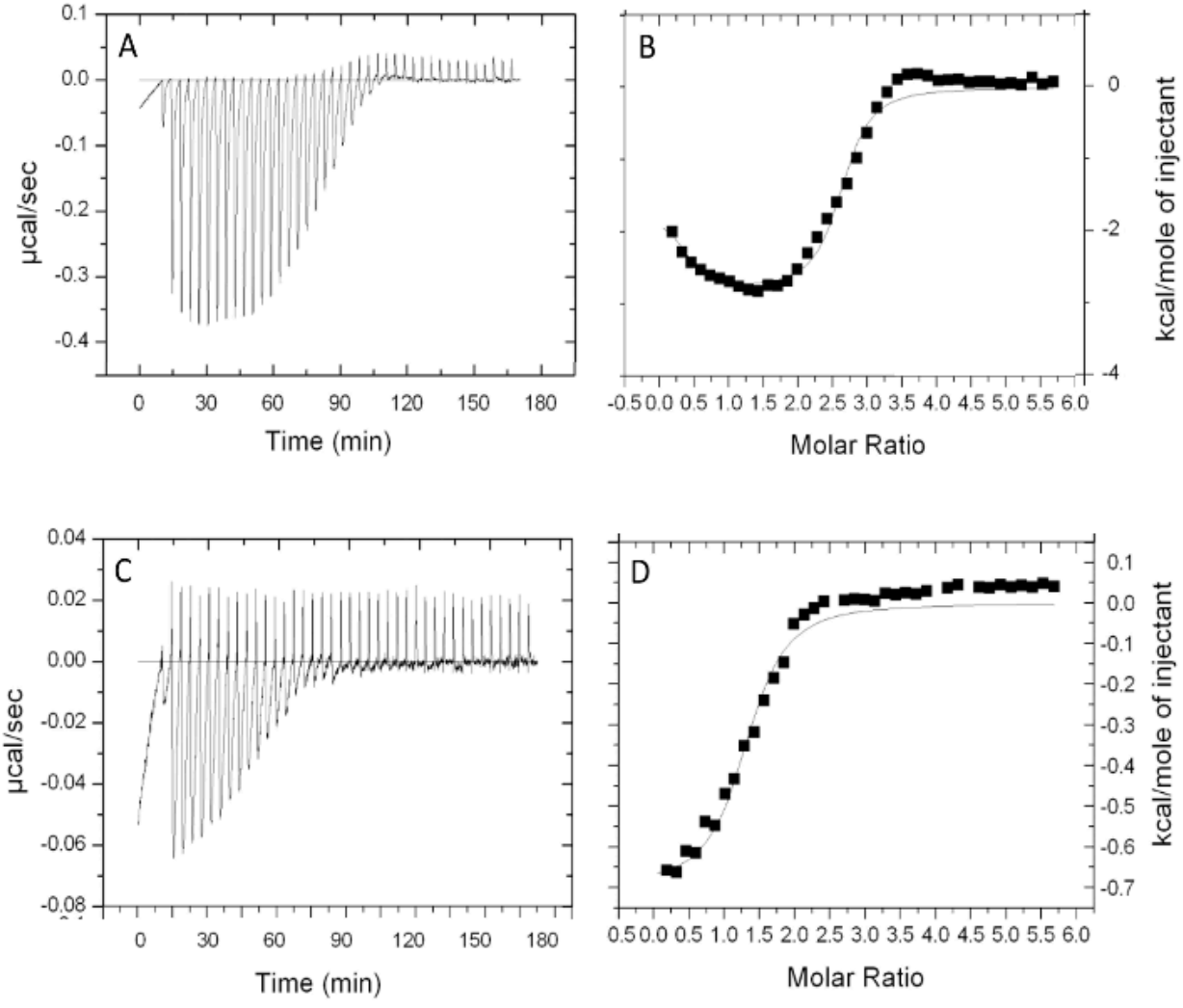

Fig. 3.3.3. Fe^{2+} binding to GCAP5 WT (left) and GCAP5$^{C15A/C17A}$ double mutant (right) measured by ITC. (A) GCAP5 WT and (C) GCAP5$^{C15A/C17A}$ represents the changes in heat upon

incremental additions of $Fe^{2+}$to the samples during the ITC at 25°C. The binding isotherms of wild-type and double mutant (B and D) were fit to a two-site and one-site model, respectively. (B) Binding isotherm of wild-type calculates two binding sites with a high-affinity site with a dissociation constant (K_d) of <100 nM and a stoichiometry (*n*) of 0.4 ± 0.1 equiv. Fe^{2+} per monomer and low-affinity site with a K_d of 3 ± 1 μM with *n* = 2 ± 0.5 equiv. per monomer. (D) The binding isotherm of the double mutant had a low-affinity site with a K_d 3 ± 1 μM[88]. Figure modified and previously published from (Lim et al, 2017) DOI:10.1021/acs.biochem.7b01029

The titration of Fe^{2+} to $GCAP5^{C15A/C17A}$ double mutant abolished the high-affinity Fe^{2+} binding site, suggesting Cys15 and Cys17 are critical residues associated with high affinity site of .Fe^{2+} (fig. 3.3.3D) [88]. The binding isotherm of the double mutant detected a low-affinity site of Fe^{2+} with a K_d of 3 ± 1 μM and *n* = 2 ± 0.5 of Fe^{2+} per monomer like that observed for wild type [88]. The low-affinity Fe^{2+} binding sites are hypothesized to be due to non-specific Fe^{2+} binding to the second and third EF-hands of GCAP5 [88].

Analytical SEC Confirms GCAP5 as a Preformed Dimer in Solution

To determine if zGCAP5 is a functional dimer like bovine GCAP1, the molecular weight was calculated by analytical SEC (fig. 3.3.4) [88]. GCAP5 (and $GCAP5^{C15A/C17A}$) were plotted in a calibration curve based on the protein standards and determined that the elution time agreed to the molar mass of 42 kDa [88]. As mentioned previously, GCAP5 monomer is 23-kDa, implying the 42-kDa weight corresponded to a dimer in solution. Moreover, fig. 3.3.4 illustrates that GCAP5 samples loaded onto SEC with the presence of Mg^{2+} and Fe^{2+} for had no effect on the molar mass of GCAP5 (and $GCAP5^{C15A/C17A}$) [88].

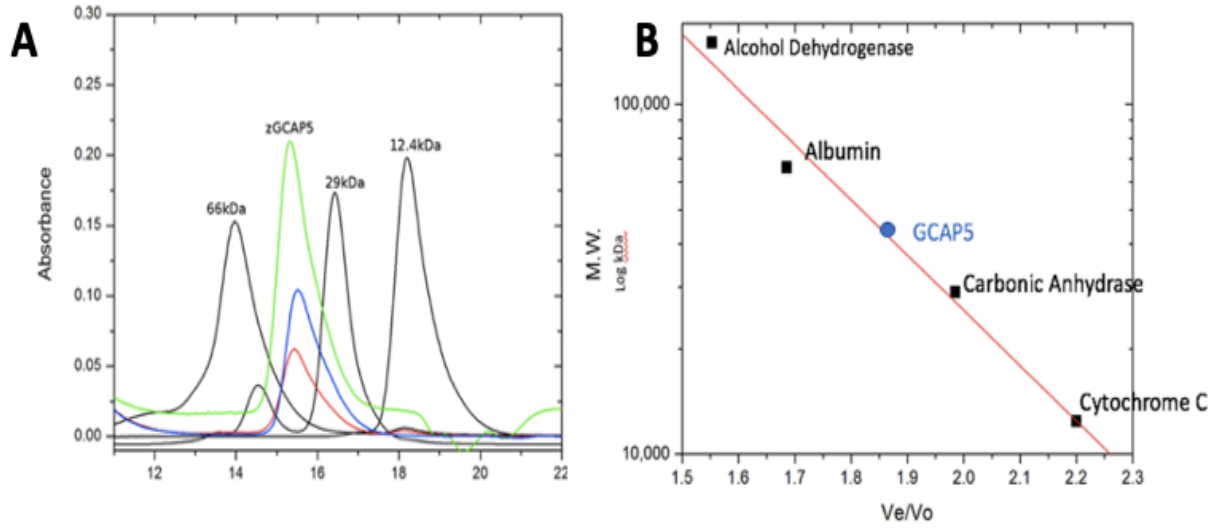

Fig. 3.3.4. Molar mass determined by analytical SEC confirms GCAP5 is a dimer. (A) An overlay of SEC chromatograms of protein standards (12.4, 29 and 66 kDa in black), GCAP5 WT in the presence of Mg^{2+} (green) and Fe^{2+} (blue) and GCAP5$^{C15A/C17A}$ in the presence of Fe^{2+} (red). All GCAP5 (and C15A/C17A mutant) samples observed similar elution profile. (B) Calculated molar mass calibration curve of elution volume over void volume against log (kDa) of standards' molecular weight. The molar mass of GCAP5 was determined to be 42 kDa and is consistent with the molecular weight of GCAP5 as a dimer[88, 101] Figure previously published from (Lim et al, 2017) DOI:10.1021/acs.biochem.7b01029

Fe^{2+}-induced Structural Changes in GCAP5 Observed by NMR

After verifying the function and stoichiometry of Fe^{2+} binding to wild type GCAP5 , I next wanted to determine whether any protein conformational changes in GCAP5 might be caused by the binding of Fe^{2+}. Fig. 3.3.5 presents NMR experiments performed with ^{15}N-labeled samples of Fe^{2+}-free GCAP5 (red) and Fe^{2+}-bound GCAP5 (black). In addition, the ^{1}H-^{15}N HSQC spectrum of ^{15}N-labeled Fe^{2+}-free GCAP5 displayed 191 peaks that were well-resolved and with uniform intensity peaks, which suggest the protein is stably folded [88]. Every resonance/peak in the 2D HSQC is associated with a particular backbone amide from a residue with characteristic chemical shift, and thus, the spectrum represents a residue-specific fingerprint of protein conformation. The HSQC spectrum of GCAP5 in the presence of saturating levels of Fe^{2+} (black peaks in Fig. 3.3.5) revealed

more than a dozen peaks whose spectral frequency and/or intensity were altered by the addition of Fe^{2+}. Fe^{2+}-binding caused some peaks to become broadened beyond detection (see peaks at 7.6, 7.8, 8.05, 9.1, 9.3, and 10.6 ppm), whereas Fe^{2+} also caused a few new peaks to appear (6.4, 6.8 and 9.7 ppm). Thus, the number of Fe^{2+}-induced spectral changes seen in Fig. 3.3.5 suggests that GCAP5 has multiple Fe^{2+} binding sites and is consistent with the Fe^{2+} binding heterogeneity observed in the ITC isotherm (Fig. 3.3.3).

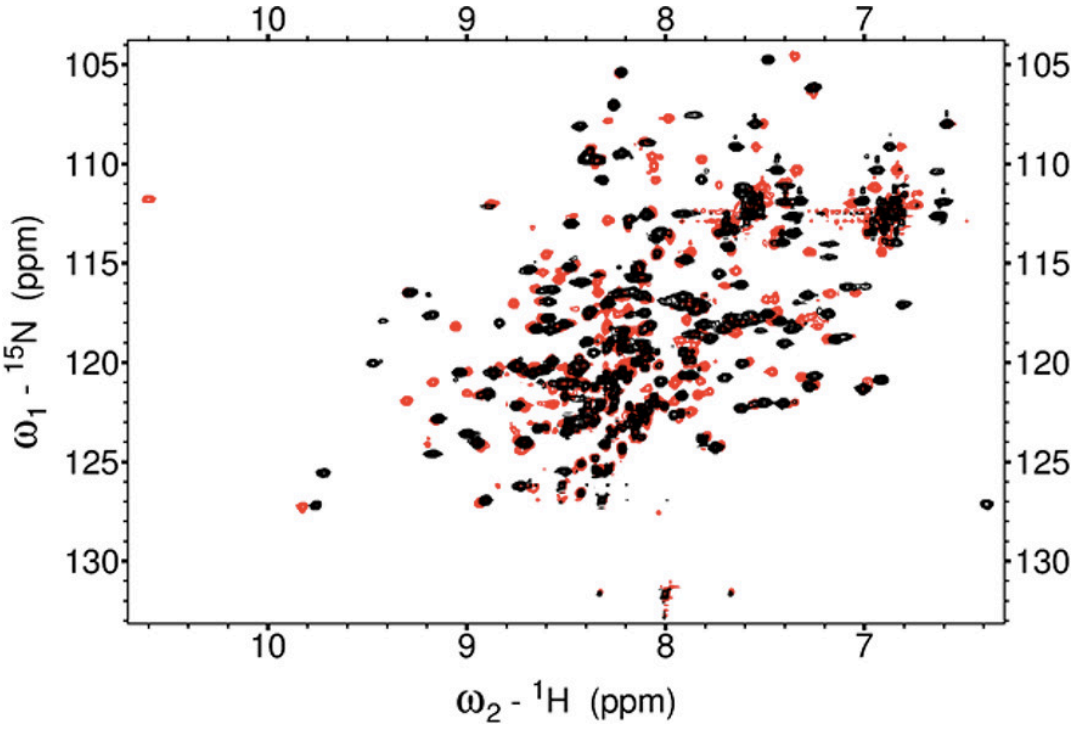

Fig. 3.3.5. ^{1}H-^{15}N HSQC spectrum of ^{15}N-labeled GCAP5. A 2D NMR HSQC spectra overlay of ^{15}N-labeled GCAP5 in the absence of Fe^{2+} (red) and the presence of saturating levels of Fe^{2+} (black) displaying the Fe^{2+} induced structural changes from the chemical shift differences observed [88]. Figure previously published from (Lim et al, 2017) DOI:10.1021/acs.biochem.7b01029.

Identifying Fe^{2+}-binding Sites in GCAP5 by NMR Titration

To identify the residues in the Fe^{2+} binding sites observed by ITC, 2D HSQC spectra were recorded of ^{15}N-labeled GCAP5 and GCAP5$^{C15A/C17A}$ samples as a function of adding incremental amounts of Fe^{2+}. Fig. 3.3.6a-b depicts the overlay of NMR spectra with Fe^{2+} concentrations (0

equiv. in red, 0.50 equiv. in green, 1.0 equiv. in blue, and 3.0 equiv. in black) in WT (A) and double mutant (B). The NMR titration of GCAP5^{WT} (Fig 3.3.6A) revealed two types of binding sites: one type had two separate resolved peaks that represent Fe^{2+}-free and Fe^{2+}-bound states (see magenta solid circle and arrows in Fig. 3.3.6A), which is indicative of slow exchange kinetics on the NMR chemical shift timescale. The term "slow exchange" in this context refers to Fe^{2+} binding event in which the exchange rate of binding is smaller (slower) than the frequency difference between the NMR peaks (representing the free and bound states). In other words, the exchange rate is slower than the chemical shift timescale and the two states are resolved. By contrast, many other peaks in the NMR titration exhibited fast exchange kinetics in which a single peak titrates from the Fe^{2+}-free to Fe^{2+}-bound state (see magenta dashed circles in Fig. 3.3.6). In this case, the exchange rate is larger (faster) than the frequency difference between the free and bound peaks and the two states are not resolved. Instead, the two states are represented by a single averaged peak whose chemical shift titrates progressively from the Fe^{2+}-free to Fe^{2+}-bound state (see dashed circles in Fig. 3.3.6). Fast exchange kinetics indicates relatively weak binding affinity in the micromolar range or higher.

The NMR resonances assigned to Cys15, Lys16 and Cys17 (highlighted by magenta filled circles and arrows in fig 3.3.6A) exhibited slow-exchange kinetics on the NMR chemical shift time scale because two sets of peaks could be assigned to the Fe^{2+}-free and Fe^{2+}-bound resonances of Cys15, Lys16 and Cys17. The Fe^{2+}-free/Mg^{2+}-bound resonances of Cys15, Lys16, and Cys17 were assigned to the peaks at 7.6/115 ppm, 7.7/116 ppm, and 7.53/111.6 ppm, respectively (fig. 3.3.7). The Cys15 and Cys17 peak assignments were confirmed by the absence of these peaks in C15A/C17A double mutant HSQC titration spectra (fig. 3.3.6) [88, 100]. The slow-exchange kinetics here for Cys15, Lys16, and Cys17 are consistent with high affinity binding of Fe^{2+} in the

nanomolar range. Thus, Cys15, Lys16 and Cys17 are shown here to have slow exchange kinetics and are associated with nanomolar Fe^{2+} binding near these residues[88]. By contrast, the Fe^{2+} sensitive resonances that exhibited fast exchange kinetics (dotted circles in Fig. 3.3.6) indicate low affinity Fe^{2+} binding (micromolar or higher) and are assigned to residues in EF2 (F62, A78 and L81) and EF3 (G102, A130).

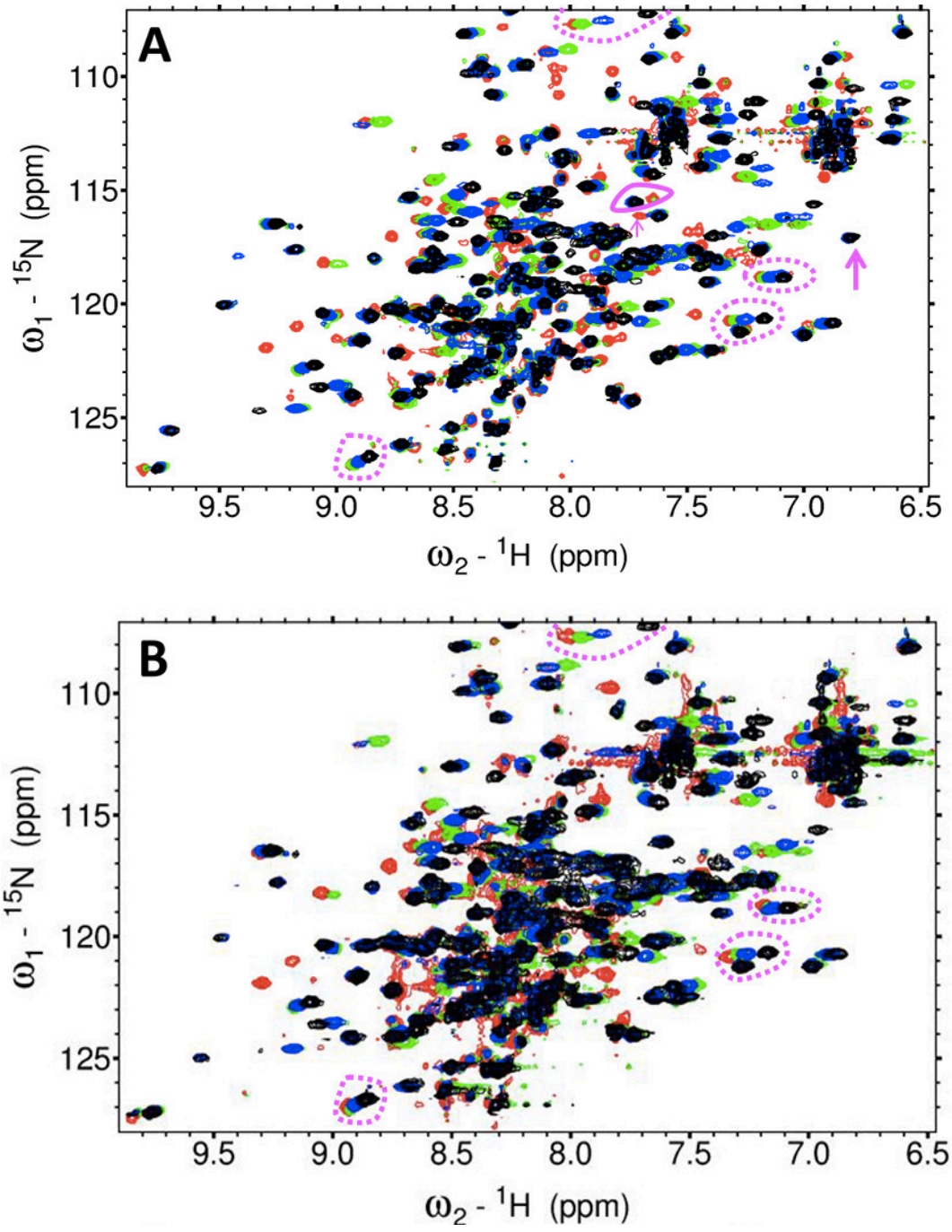

Fig. 3.3.6. NMR titration of Fe^{2+} binding to GCAP5 WT (A) and GCAP5$^{C15A/C17A}$ double mutant (B). ^{1}H-^{15}N HSQC overlay of GCAP5 WT and GCAP5$^{C15A/C17A}$ double mutant titrated with incremental aliquots of Fe^{2+} at 0 (red), 0.50 (green), 1.0 (blue) and 3.0 (black). Resonances marked by a magenta filled circle and arrows exhibited slow exchange kinetics and resonances marked by dashed circles exhibited fast exchange kinetics during the titration experiment[88]. Figure previously published from (Lim et al, 2017) DOI: 10.1021/acs.biochem.7b01029.

The ^{1}H-^{15}N HSQC spectrum of ^{15}N-labeled Fe^{2+}-bound GCAP5$^{C15A/C17A}$ double mutant (fig. 3.3.6B) shows an absence of resonances that were assigned to Cys15 and Cys17 in the wild type spectrum [88]. Instead, the double mutant spectra identified resonances highlighted in magenta dashed lines (fig. 3.3.6B) that corresponded to fast exchange kinetics, in which the Fe^{2+} binding is faster than the frequency difference between the peaks in the bound versus the free state and corresponds to micromolar or weaker affinity. The fast exchanging peaks were mostly assigned to resonances from EF2 and EF3, which is consistent with the lower affinity Fe^{2+} binding occurring in the EF-hands.

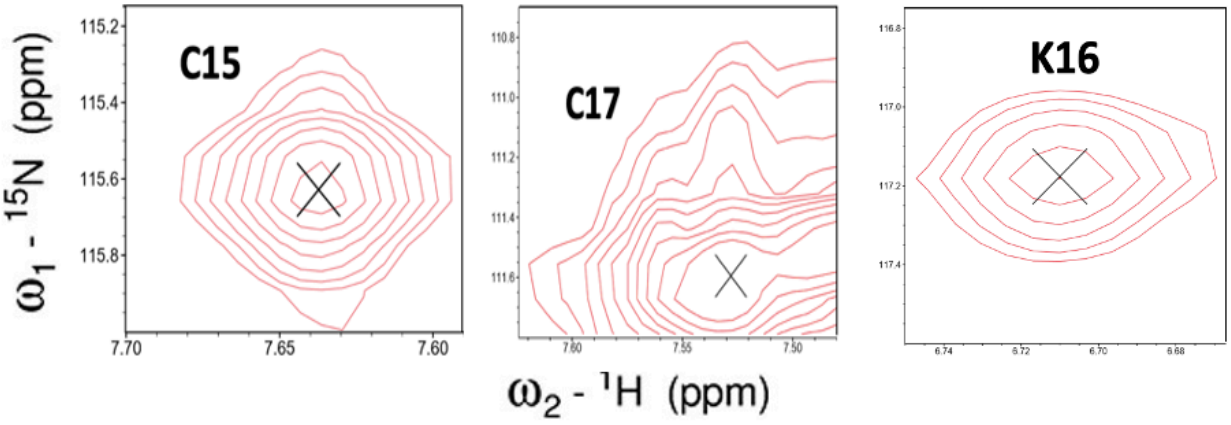

Fig. 3.3.7. Slow exchange resonances in NMR titration of Fe^{2+} binding to GCAP5^{WT}. Resonances exhibiting slow exchange were assigned to C15, K16, and C17 [88, 100].

NMR Assignments of Mg^{2+}-bound Myristoylated GCAP5

The final assignments of backbone and sidechain resonances of uniformly ^{13}C- and $^{13}C/^{15}N$-labeled Mg^{2+}-bound myristoylated GCAP5 (native residues 2–198 with D3N mutation for

NMT) are represented by the 2D ^{1}H-^{15}N HSQC and constant-time ^{1}H-^{13}C HSQC as shown (fig. 3.3.7). The ^{1}H-^{15}N HSQC spectrum exhibited well-dispersed peaks and uniform intensities, which confirmed that GCAP5 in solution was stably folded and the assignments were determined based on acquired the triple-resonance heteronuclear NMR spectra. The NMR structural studies of Ca^{2+}-free/Mg^{2+}-free myristoylated GCAP5 obtained assignments of more than 86% of the main chain ^{13}C resonances ($^{13}C\alpha$, $^{13}C\beta$ and ^{13}CO), 84% of backbone amides (^{1}HN, ^{15}N), and 75% of ^{13}C methyl sidechain resonances [100]. As GCAP5 is a dimer in solution, remaining unassigned residues (fig. 3.3.8B) were mostly in spectrally overlapped regions (due to peak broadening) or were broadened beyond detection. Fig. 3.3.8B identifies unassigned residues (in asterisk) in the GCAP5 sequence and is prominent that residues 136-146 are unassigned that could be due to NMR exchange broadening from confirmational heterogeneity in the fourth EF-hand. The chemical shift assignments of GCAP5 can be found in the BioMagResBank (http://www.bmrb.wisc.edu) with accession number 27705 [100].

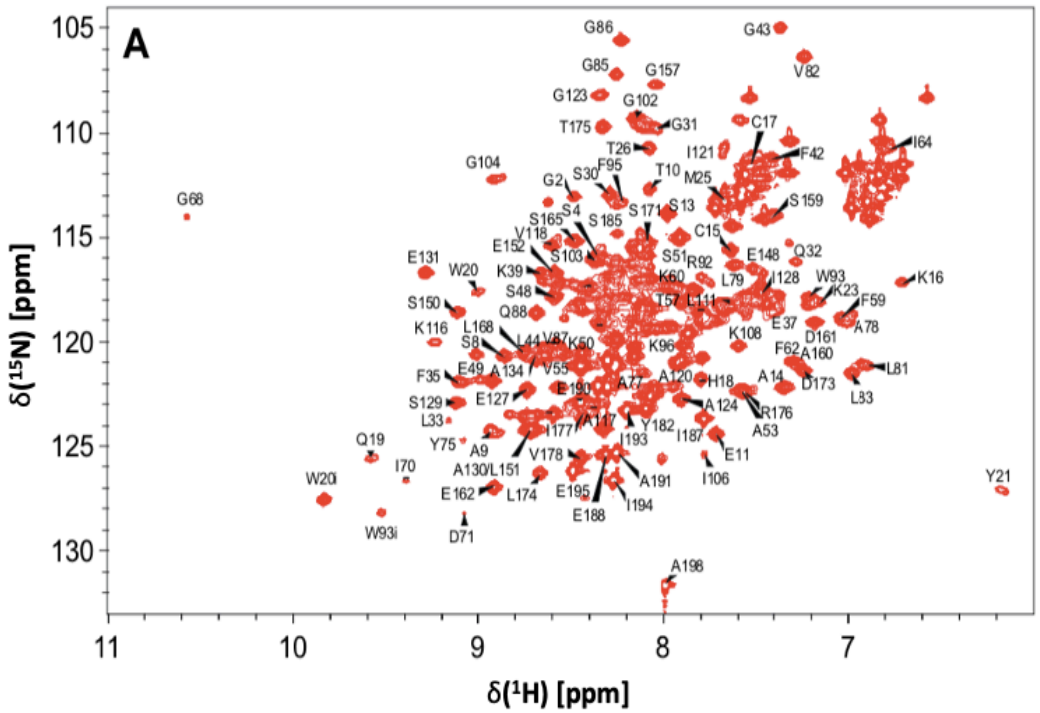

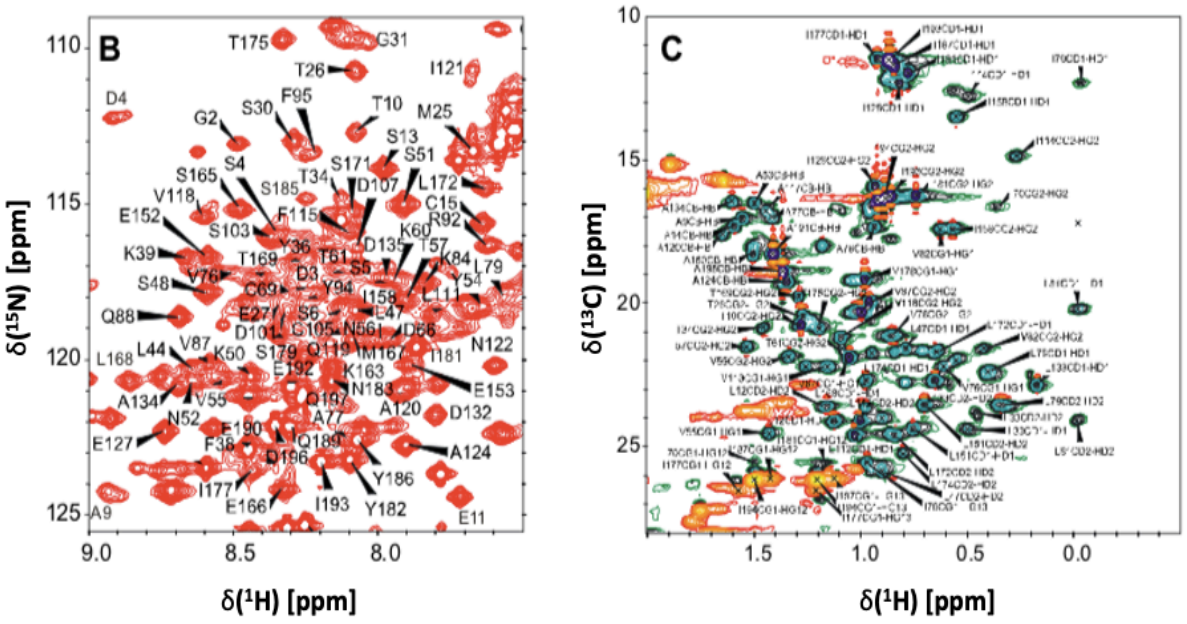

Fig. 3.3.7. Two-dimensional ^{1}H-^{15}N HSQC and constant-time ^{1}H-^{13}C HSQC. (A) ^{1}H-^{15}N HSQC spectrum of ^{15}N-labeled Ca^{2+}-free/Mg^{2+}-bound myristoylated GCAP5 illustrating labeled representative backbone assignments (86%). (B) Expansion view of ^{1}H-^{15}N HSQC in spectrally crowded region showing challenge of assignment process. (C) Constant-time ^{1}H-^{13}C HSQC spectrum of ^{13}C-labeled Ca^{2+}-free/Mg^{2+}-bound myristoylated GCAP5 representing labeled sidechain resonances critical for NOE analysis. Complete assignments are available (BMRB accession no. 27705) [100]. Figure previously published from (Cudia, 2019).

The secondary structure of Ca^{2+}-free/Mg^{2+}-bound myristoylated GCAP5 was calculated based on the NMR backbone assignments and uploaded onto a secondary structure prediction online software called TALOS+ [91, 110]. The secondary structure was determined from the calculated difference between observed chemical shifts and the average random coil chemical shifts [91]. The secondary structure of GCAP5 was found to be quite similar to that of mammalian GCAP1 (fig. 3.3.8B). There were ten pronounced α-helices at regions H1 (residues8-14), H2 (residues 18-26), H3 (residues 35-41), H4 (residues 49-62), H5 (residues 74-82), H6 (residues 87-95), H7 (residues 110-117), H8 (residues 129-135), H9 (residues 150-160), and H10 (residues 162-172) (fig. 3.3.8A/B) [100]. The secondary structure in all EF-hands (helix-loop-helix) are detectable, with the

exception that the third and fourth β-strands aren't clear due to a lack of stabilization by Mg^{2+} as seen in the second EF-hand (fig. 3.3.8A/B) [100].

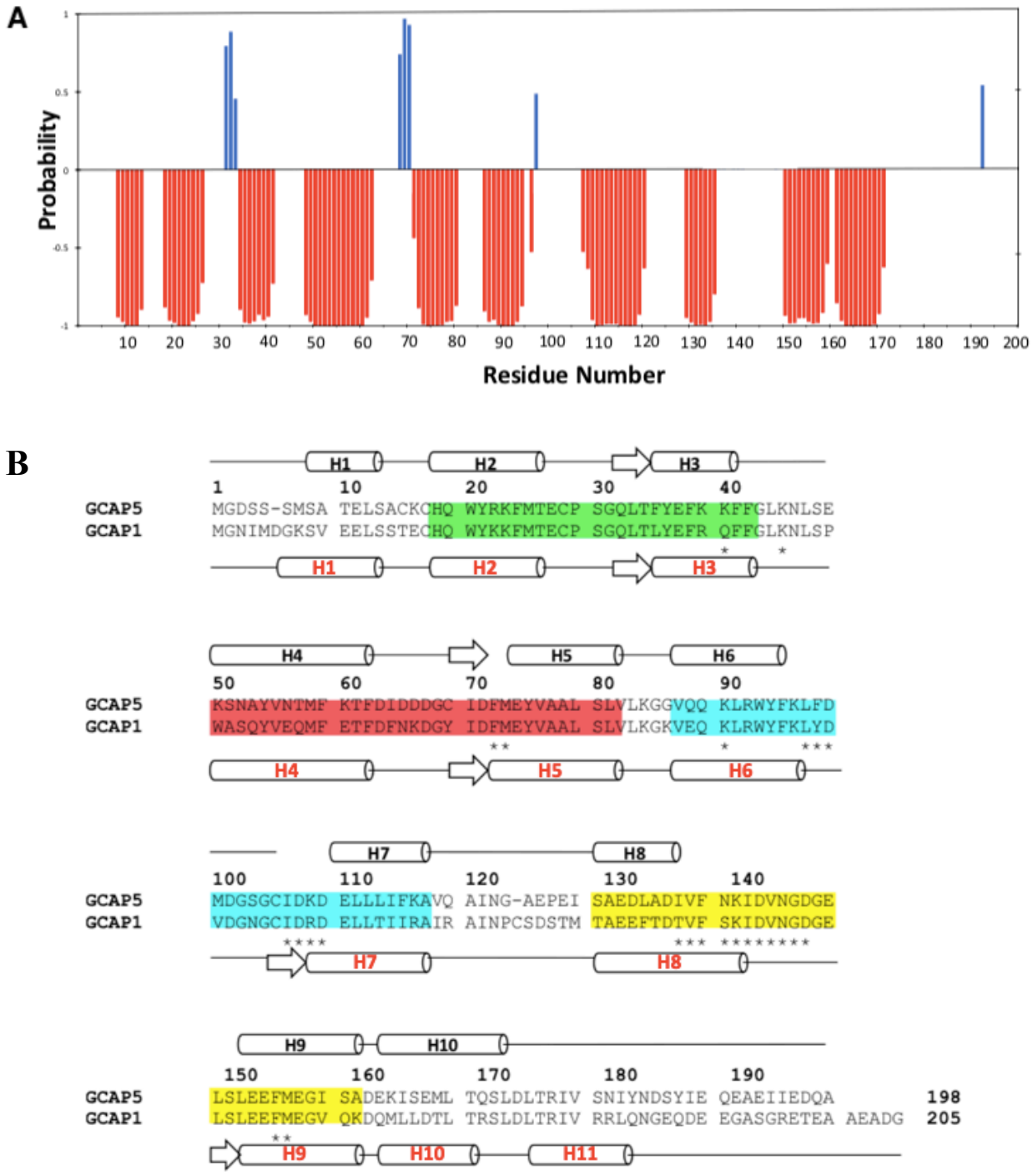

Fig. 3.3.8. Amino acid sequence and secondary structure of Ca^{2+}-free/Mg^{2+}-bound myristoylated GCAP5. (A) Chemical shift index (CSI) calculated by TALOS+ANN secondary structure plotting the probability (α-helix as negative, β-strand as positive, and random coil as

zero) as a function of residue number. (B) Sequence alignment of GCAP5 and GCAP1 with labeled EF hands (green for EF1, red for EF2, cyan for EF3, and yellow for EF4) based on TALOS+ analysis. α-helix is represented as a cylinder, β-strand as arrow, and random coil as line. Residues marked with an asterisk are unassigned (BMRB accession no. 27705) Secondary structure of GCAP5 is represented above its sequence (labeled H1-10 in black) and GCAP1 is represented below its sequence (labeled H1-11 in red) [100]. Figure modified and previous published from (Cudia, 2019) DOI: 10.1007/s12104-019-09877-y

NOESY-based distances are critical for determining the three-dimensional structure of GCAP5. NOESY-derived distances are calculated from the rate of magnetization transfer through space between residues far apart in sequence but within 5 Å. The terminal methyl sidechain resonance assignments were important for NOESY-based analysis. In fig. 3.3.9, representative ^{15}N-amide strips show cross peaks between L172Hδ2 and T61Hγ2, G2Hα2 and V178Hγ1, and V55Hγ2 and I181Hγ2, respectively, that determined these long-range residues were within 5 Å. Despite severe overlapping seen across all NMR spectra, NOESY-based analysis collected 145 long-range NOEs to aid in solving the globular shape of GCAP5 [101].

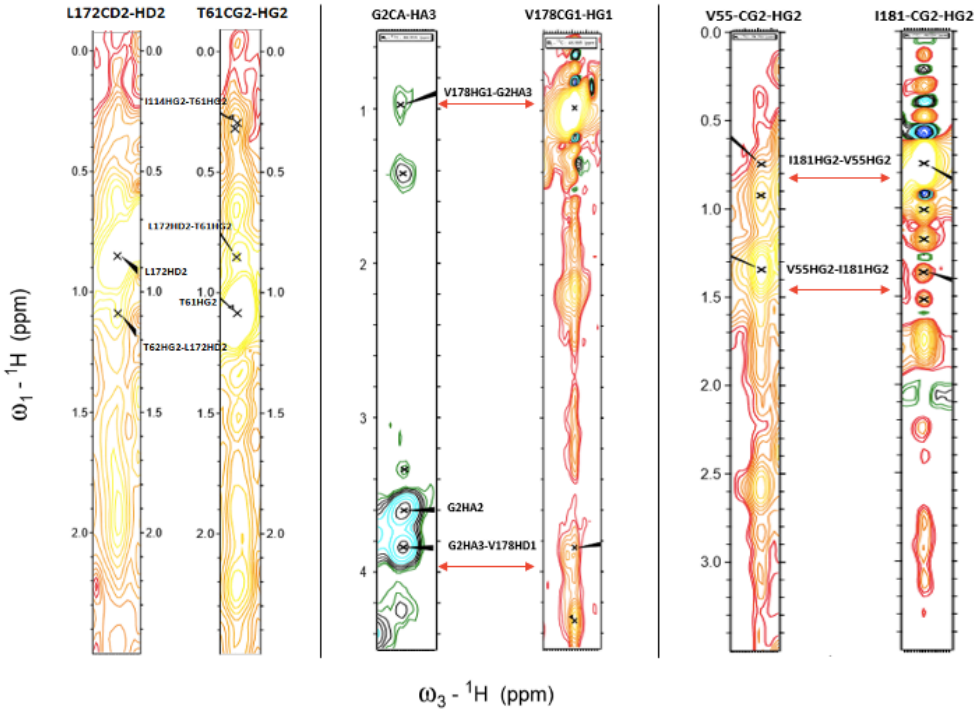

Fig. 3.3.9. Representative ^{15}N-NH amide strip plots in NOESY analysis of Ca^{2+}-free/Mg^{2+}-bound GCAP5. Long-range NOEs are represented between L172Hδ2-T61Hγ2 (left), G2Hα2-V178Hγ1 (center), and V55Hγ2-I181Hγ2 (right).

The final structural restraints needed for calculating the 3D structure of Ca^{2+}-free/Mg^{2+}-bound GCAP5 was residual dipolar coupling (RDCs) restraints to determine the orientation of secondary structure (α-helices) relative to one another. In fig. 3.3.10, RDCs were calculated based on the absence and presence of the orienting medium *Pf1* phage. The calculated RDCs versus the observed RDCs are in good agreement (fig. 3.3.10C) and was used in the structural calculation by Xplor-NIH with the following restraints: NMR-derived dihedral angles, NOESY-based distances, and RDCs [101].

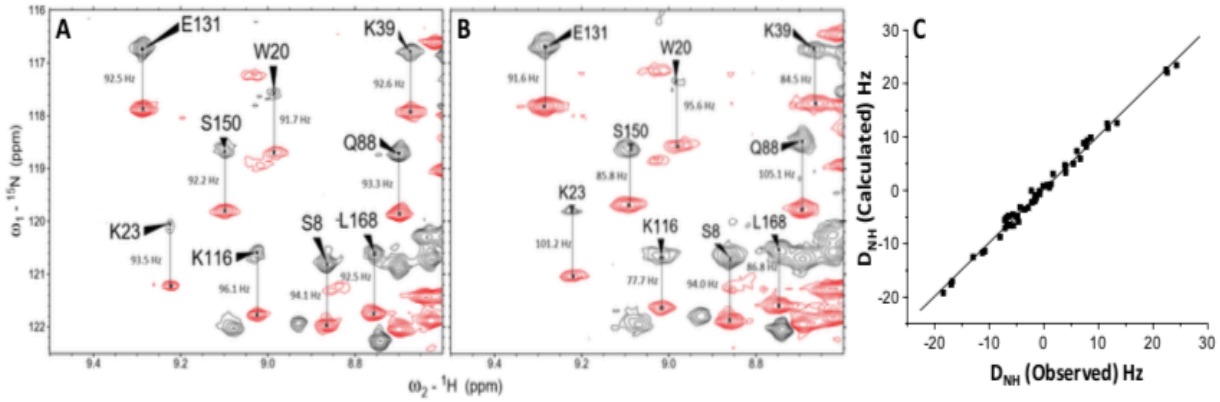

Fig. 3.3.10. Residual dipolar coupling (RDC) structural analysis to determine orientation of α-helices in globular three-dimensional structure of GCAP5. ^{1}H-^{15}N IPAP-HSQC spectra of Ca^{2+}-free/Mg^{2+}-free GCAP5 in the absence (A) and presence (B) of *Pf1* orienting medium (12 mg/mL). The observed spectral J_{NH} splitting (in the absence and presence of *Pf1* phage, respectively) between J_{NH} and J_{NH} + D_{NH} are represented by vertical lines and differences were used to calculate RDCs. (C) Calculated RDCs are plotted against the measured RDCs and show good agreement with Q-factor = 0.27 and R-factor = 0.985 [101, 105].

NMR Solution Structure of Ca^{2+}-free/Mg^{2+}-bound Myristoylated GCAP5

The NMR solution structure of Ca^{2+}-free/Mg^{2+}-bound GCAP5 was calculated with the structural restraints (table 3.3.1) by restrained molecular dynamics simulations within Xplor-NIH as

described previously [101]. An overlay of the ten lowest energy structures calculated by Xplor-NIH in fig. 3.3.11. has an RMSD of 1.0 Å [101]. Interestingly, the TALOS-derived secondary structure and NOESY-based analysis determined GCAP5 to be structurally similar to Ca^{2+}-bound GCAP1 with 11 α-helices and 4 β-strands: α1 (residues 8-15, *N-terminal helix*), α2 (residues 19-27), α3 (residues 35-41), α4 (residues 50-62), α5 (residues 72-82), α6 (residues 88-97), α7 (residues 108-121), α8 (residues 130-140), α9 (residues 151-160), α10 (residues 162-172, *Ca^{2+}-switch helix*), α11 (residues 175-182, *C-terminal helix*), β1 (residues 32-34, *non-functional EF*), β2 (residues 69-71, *Mg^{2+}binding*), β3 (residues 105-107), and β4 (residues 148-150) (see fig. 3.3.11) [59, 101].

A

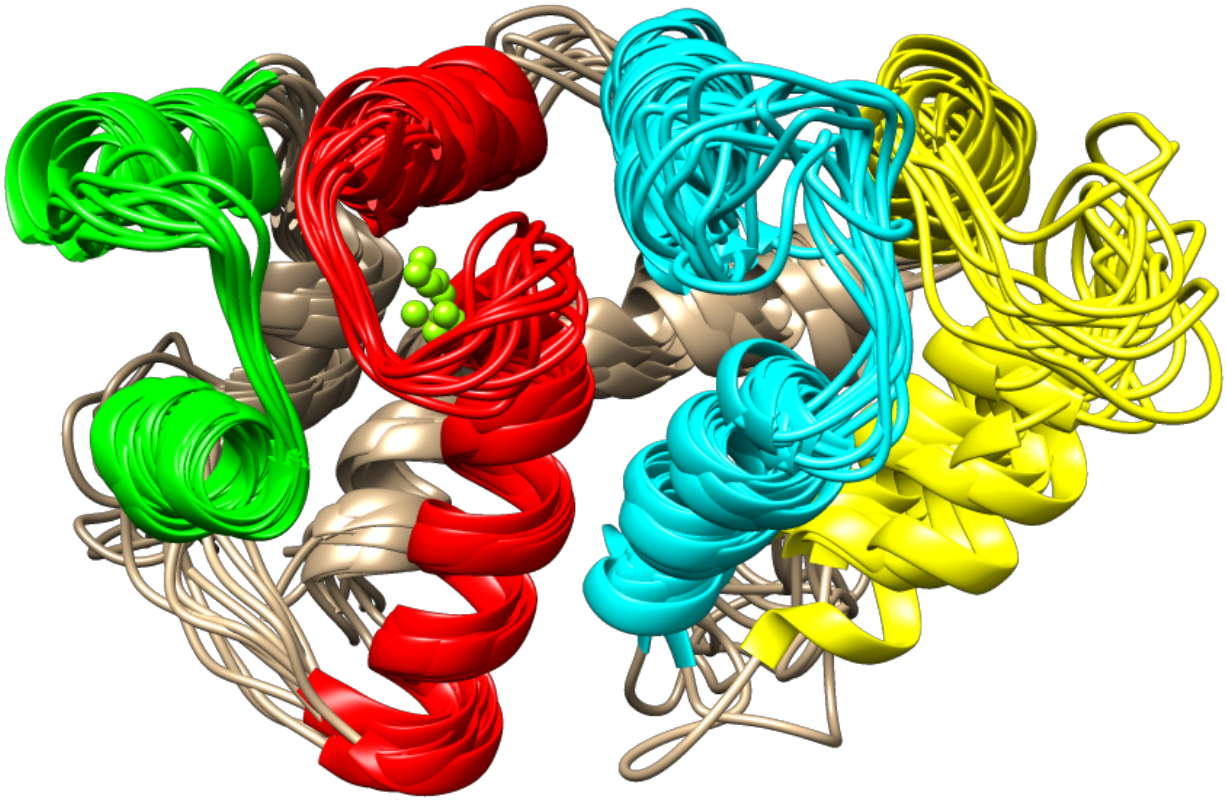

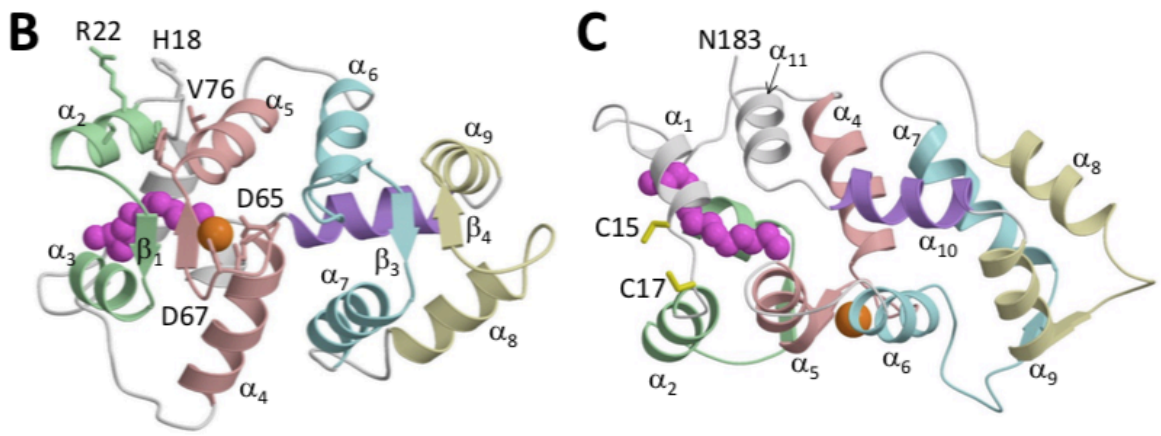

Fig. 3.3.11. NMR-derived ensemble solution structure of Ca^{2+}-free/Mg^{2+}-bound GCAP5 (PDB ID: 7M2M). (A) The ensemble of the ten lowest NMR structures has a RMSD of 1.0 (table 3.3.1.). EF-hands are represented in EF1 (green), EF2 (red), EF3 (cyan), and EF4 (yellow) with Mg^{2+} ion in green [101]. (B-C) The average main chain structure of GCAP5 showing a similar structural arrangement as bovine Ca^{2+}-bound GCAP1(see fig. 1.4.4B)[59]. N-terminal myristoyl group is presented in magenta and Ca^{2+}-switch helix (α10) associated in activator-to-inactivator state is in purple. Sidechain atoms of residues involved in Mg^{2+} binding (D63, D65, D67) and at the dimeric interface is shown in (H18, Y21, M25, F72, V76) are shown in sticks [101].

The initial secondary structure of GCAP5 determined by chemical shift index (TALOS+) identified the C-terminal residues in α11 as a random coil; however, a more rigorous analysis of long-range and sequential NOEs observed between N-terminal and C-terminal domain was able to define a C-terminal helix that was apparently not detected by chemical shift index [91, 101]. I do not understand why the C-terminal helix was not detected by the chemical shift analysis. One possibility is that the C-terminal helix might exhibit dynamics that might perturb the chemical shifts. In any event, this illustrates the limitation of secondary structure prediction by chemical shift index. The detailed NOE patterns of an α-helix appear to be a more reliable method of determining secondary structure. Despite this discrepancy, the solution structure of GCAP5 formed two domains: N-terminal (EF1 - EF2) and C-terminal (EF3 – EF4) described in fig. 3.3.11 [101]. Interestingly, Cys15 and Cys17 are more solvent-exposed in GCAP5 due to the elongation of

the N-terminal helix observed (fig. 3.3.11C). This lengthening of the N-terminal helix of GCAP5 allows Cys15 and Cys17 to facilitate Fe^{2+} binding, which is not seen in mammalian GCAP1 (fig. 3.3.8) [100, 101].

The Ca^{2+}-switch helix (α10, fig. 3.3.11B/C purple helix) observed in GCAP1 studies is also conserved in GCAP5, where Mg^{2+}-bound state is one turn longer than Ca^{2+}-bound GCAP1 and is consistent as an activator (Ca^{2+}-free/Mg^{2+}-free GCAP5) [53, 59, 101]. Finally, the C-terminal helix (α11) of Mg^{2+}-bound GCAP1 is one-half turn shorter than Ca^{2+}-bound GCAP1 and is similar to the Ca^{2+}-myristoyl tug mechanism as previously described in GCAP1 studies [43, 53, 59, 101]. Overall, the NMR-derived solution structure of Ca^{2+}-free/Mg^{2+}-bound myristoylated GCAP5 (PDB: 7M2M) was validated by the online software PROCHECK and confirmed that 90% of the residues were in the most favorable region in the Ramachandran plot (table 3.3.1.) [101, 112].

Table 3.3.1. NMR structural statistics of GCAP5

NMR restraints	Value (restraint violation)
Short-range NOEs	526 (0.0 ± 0.0)
Long-range NOEs	145 (0.0 ± 0.0)
Hydrogen bonds	144 (not used in water refinement)
Dihedral angles	172 (0.1 ± 0.3)
$^1D_{HN}$ RDC	24 (0.0 ± 0.0)
RDC Q-factor	0.321
Coordinate precision (Å)*	
RMSD (backbone atoms)	1.0 ± 0.04
RMSD (all heavy atoms)	1.6 ± 0.1
Deviation from idealized geometry	
Bonds (Å)	0.007 ± 0.001
Angles (°)	0.823 ± 0.015
Impropers (°)	0.925 ± 0.025

Ramachandran Plot (%)	
Favored region	78.1
Allowed region	16.3
Outlier region	5.6
Structure quality[#]	
Clash score	80
Ramachandran outliers	5.6%
Sidechain outliers	6.1%

[*]Coordination precision was calculated for residues 9-16, 20-41, 49-81, 89-120, 130-139, and 158-160.
[#]Structure quality metrics assessed by MolProbity [112]

Extent of Protein Myristoylation

Spectral heterogeneity of the GCAP5 samples were observed in all NMR spectra recorded and posed challenges in the structural analysis by NMR. In particular, the 2D ^{15}N-^{1}H HSQC spectrum of Ca^{2+}-free/Mg^{2+}-free GCAP5 frequently exhibited more than one resonance that could be assigned to a single residue, suggesting multiple structural forms of GCAP5 that is perhaps due to a mixture of myristoylated and non-myristoylated forms of the protein. To test whether incomplete myristoylation might be causing the spectral heterogeneity, the extent of myristoylation in the NMR sample was analyzed by liquid chromatography and mass spectroscopy (LC-MS) analysis on samples of myristoylated GCAP5 and unmyristoylated GCAP5 (lacking pBB131-NMT in plasmid DNA) in fig. 3.3.12. The LC-MS (MALDI) was measured by Dr. William T. Jewel at the Mass Spectrometry facility at the University of California Davis (UCD). The N-terminal myristoyl group is ~200 Da and the mass-to-charge (m/z) difference between the two samples observed a ~200 Da difference, indicative of the absence of the myristoyl group in the unmyristoylated GCAP5 (fig. 3.3.12, top). Fig. 3.3.12 shows myristoylated GCAP5 (bottom) had a calculated mass of 22.3 kDa while the unmyristoylated GCAP5 (top) had a calculated mass of 22.5 kDa. Peak broadening is observed in both samples as GCAP5 samples have a high

propensity of aggregation at high concentration. Moreover, the absence of the N-terminal myristoyl group (fig. 3.3.12) has been shown to destabilize the tertiary structure of GCAP5[40]. Therefore, the myristoylated protein samples used in the NMR studies do not appear to have detectable amounts of non-myristoylated protein, and the apparent NMR spectral heterogeneity is likely not caused by contamination of non-myristoylated protein.

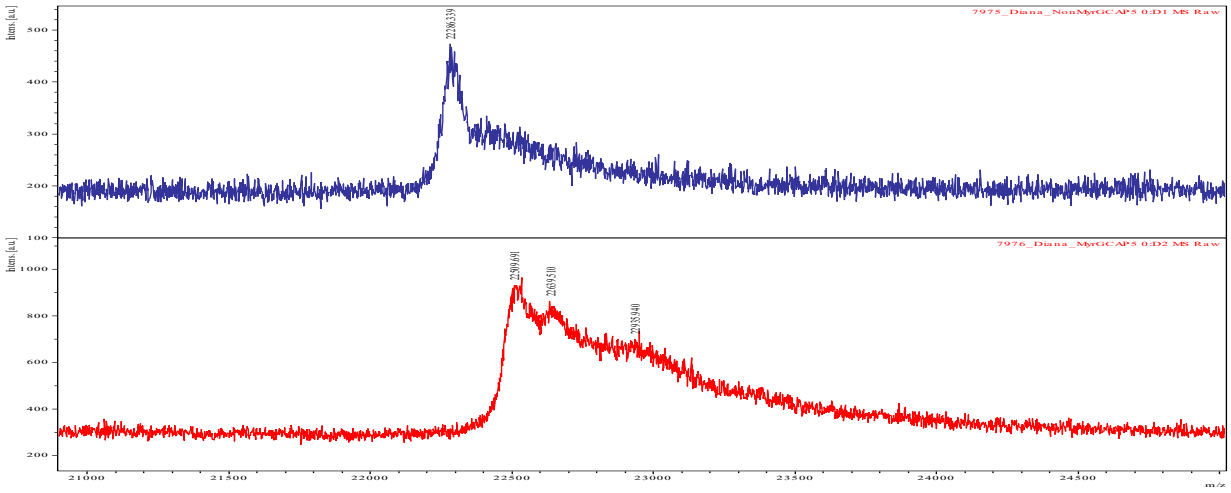

Fig. 3.3.12. Liquid-chromatography mass spectroscopy (LC-MS MALDI). Extent of myristoylation detected by LC-MS (C8 column) from unmyristoylated (top) and myristoylated (bottom) GCAP5 WT showing mass-to-charge (m/z) at 22,286.339 (unmyr-GCAP5) and 22,509.691 (myr-GCAP5).

To further test whether incomplete myristoylation caused NMR spectral heterogeneity, samples of myristoylated and unmyristoylated GCAP5 were separately analyzed by HSQC and showed characteristic spectral differences between these samples (fig. 3.3.13). The unmyristoylated HSQC spectrum (fig. 3.3.13A, blue) exhibited a smaller number of peaks, partly due to the absence of myristoyl group that may cause protein unfolding. The resonance assigned to A198 in non-myristoylated GCAP5 has a different amide proton chemical shift compared to that of myristoylated GCAP5 (Fig. 3.3.1.3D). Interestingly, the myristoylated HSQC spectrum (fig. 3.3.13B, red) showed a weaker resonance assigned to A198 (^{15}N 131.6 ppm, ^{1}H-N 8.00 ppm, fig. 3.3.13C) that had 100-fold weaker intensity compared to a separate and more intense peak

assigned to A198. The weaker resonance (^{15}N 131.6 ppm, ^{1}H-N 7.91 ppm, fig. 3.3.13C-D) corresponded to the unmyristoylated A198 resonance. Thus, the HSQC spectra overlay suggests that the myristoylated NMR sample contains less than 1% of the unmyristoylated protein (fig. 3.3.13). So, the observed NMR spectral heterogeneity of GCAP5 is not caused by incomplete myristoylation. Instead, the extra NMR peaks might be the result of protein dimerization and/or the presence of multiple conformational states of the myristoylated protein.

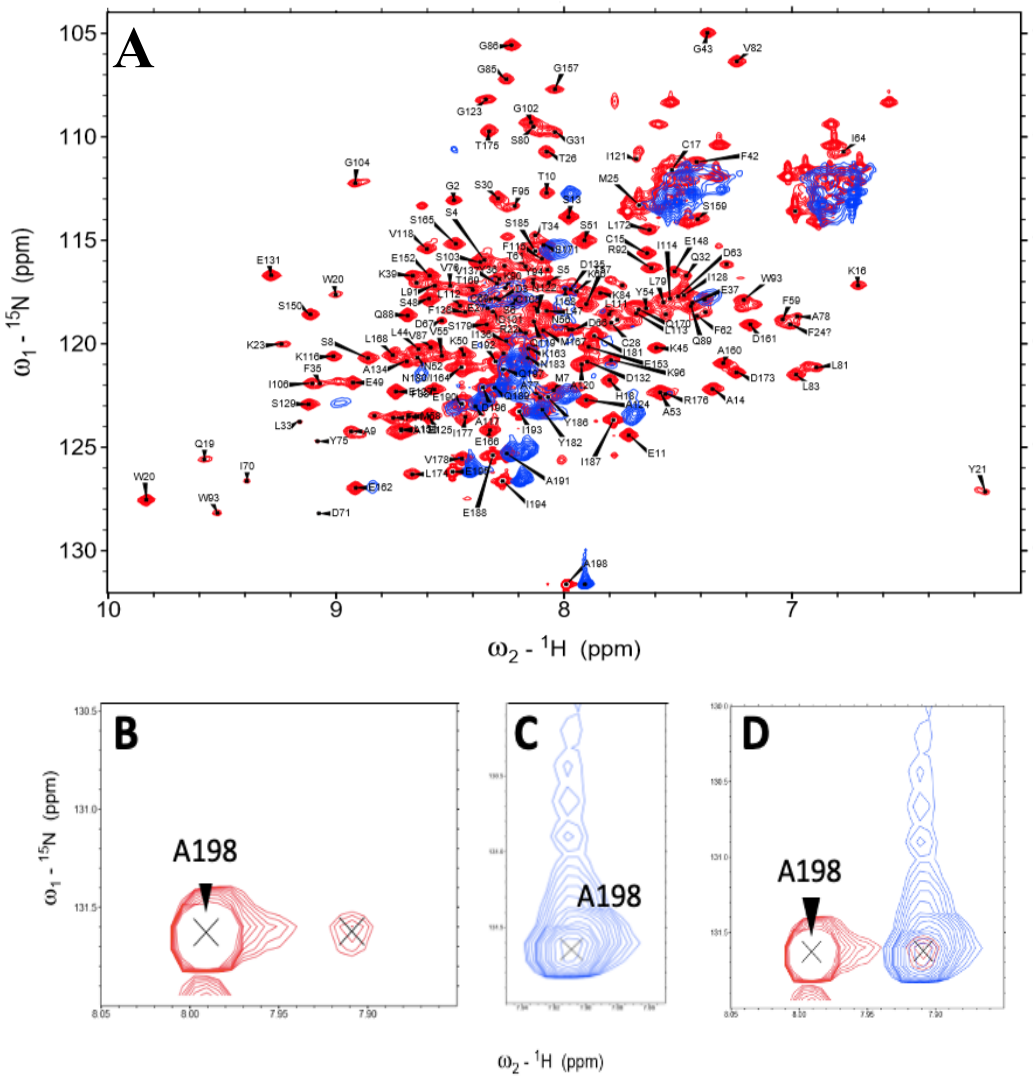

Fig. 3.3.13. ^{15}N-^{1}H HSQC spectra overlay. (A) 2-dimensional NMR spectra of Ca^{2+}-free/Mg^{2+}-bound myristoylated GCAP5 (co-expressed with pBB131-NMT) in red and Ca^{2+}-free/Mg^{2+}-bound non-myristoylated GCAP5 (lacking pBB131-NMT) in blue. (B-D) Expansion view of A198 resonance assignment in myristoylated (red) and non-myristoylated (blue) shows trace amount of

non-myristoylated protein in Ca^{2+}-free/Mg^{2+}-bound myristoylated GCAP5 (co-expressed with pBB131-NMT) sample.

Molecular Docking of GCAP5 Dimer Guided by EPR-DEER Restraints

GCAP5 was previously determined to be a pre-formed dimer in solution as reported (fig. 3.3.4.)[100, 101]. As was done previously for GCAP1[88], the structure of dimeric GCAP5 was calculated from intermolecular distances measured by electron paramagnetic resonance double electron-electron resonance (EPR-DEER) spectroscopy[62, 101]. Native Cys residues (C15, C17, C28, C69, C105) were first mutated to alanine (Ala, A) for a Cys-less background (hereafter termed $GCAP5^{CL}$) and then re-introduced a single cysteine (A $\rightarrow$ C mutation) for nitroxide spin labeling. Non-native residues (T26, N56, N139, E152, E156, S159) are exposed and more accessible for nitroxide spin labeling. These residues were each mutated to single Cys in $GCAP5^{CL}$ to do structural analysis like that of GCAP1[62, 101]. EPR-DEER measured the intermolecular distances observed in all single Cys mutants (fig. 3.3.14) and table 3.3.2 represents a total of 11 EPR-DEER intermolecular distance restraints used for protein-protein docking by HADDOCK [101, 113].

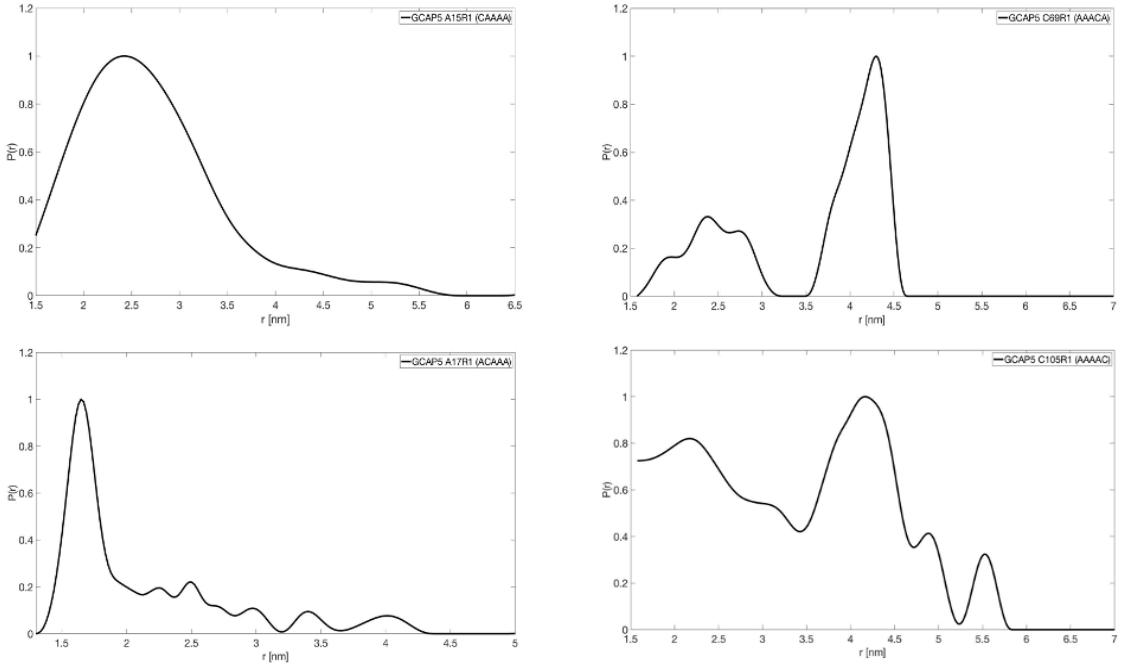

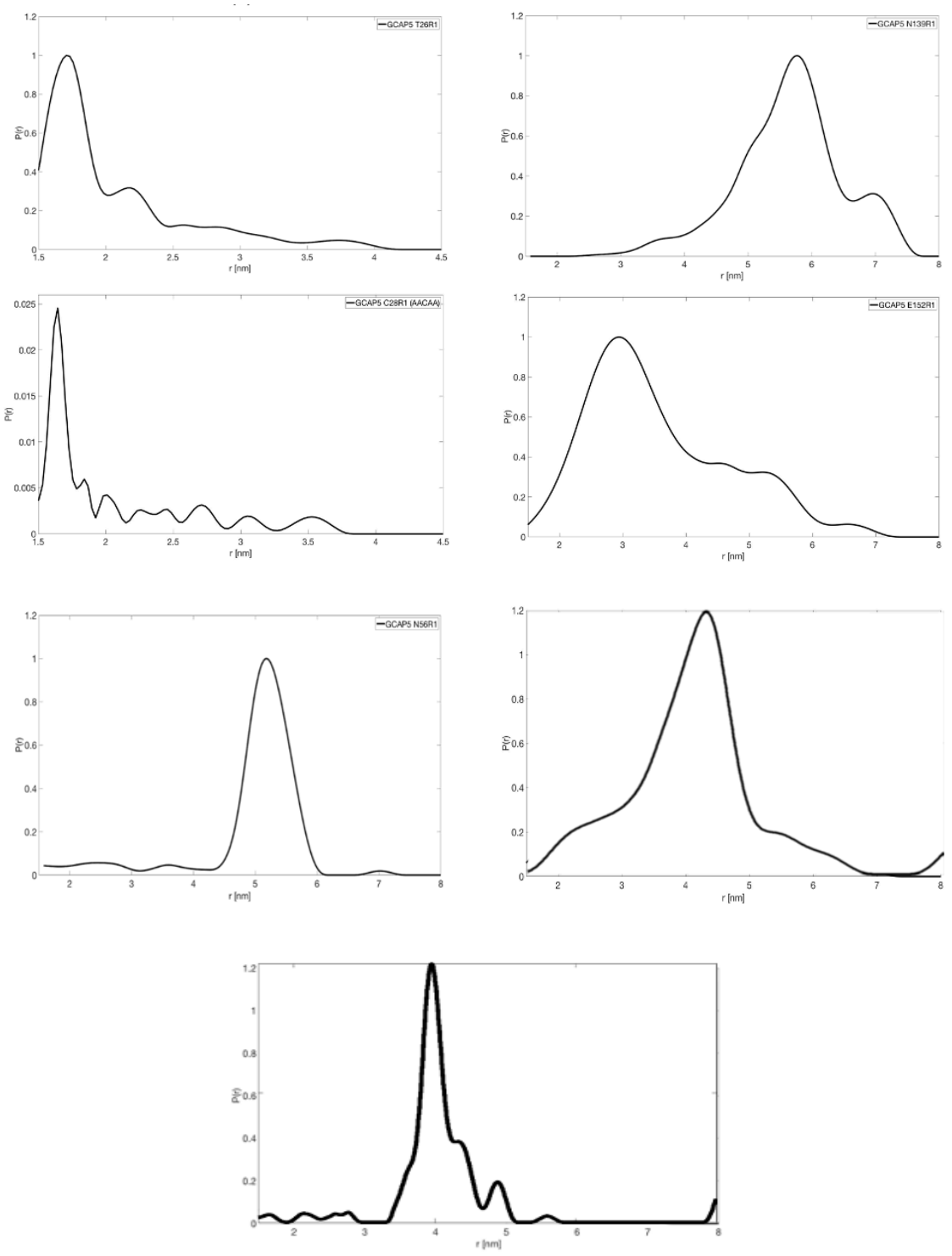

Fig. 3.3.14. Intermolecular distances of single Cys mutants measured by EPR-DEER. Probability plotted versus intermolecular distances (nm) in GCAP5^{CL} mutants (ordered from top to bottom per column: A15C, A17C, T26C, A28C, N56C, A69C, A105C, N139C, E152C, E156C, and S159C (bottom row)) [101].

Structural Model of a GCAP5 Dimer

The intermolecular DEER distances for each spin-label attached to GCAP5 (Fig. 3.3.14 and Table 3.3.2) were used as distance restraints within HADDOCK [113] to calculate the structure of the GCAP5 dimer as described in Methods. The measured DEER distances (Table 3.3.2) for the most part agree within experimental error with the calculated intermolecular distances in the GCAP5 dimer model (Fig. 3.3.16A). The apparent deviation between the calculated versus observed distances for Cys15 and Cys17 (important for Fe^{2+} binding [88]) might reflect the dynamic disorder for these residues in the absence of Fe^{2+}.

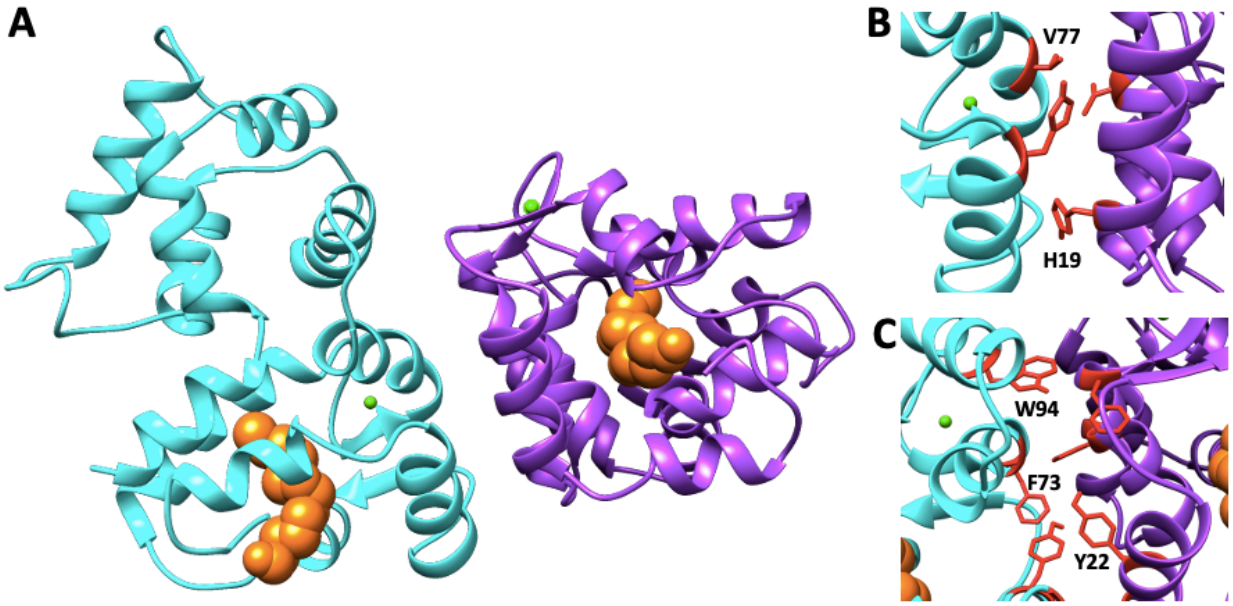

Fig. 3.3.15. Symmetric dimer structure of GCAP1. (A) Ribbon diagram of GCAP1 as a symmetric dimer based on the EPR-DEER intermolecular distances measured for nitroxide-spin labeled mutants as described[62]. (B-C) Expansion view of the dimeric interface with hydrophobic intermolecular contacts between resides in red (H19, Y22, F73, V77 and W94). Mutations at the dimeric interface in GCAP1 were shown to disrupt dimerization and weaken cyclase activation[62]. Figure modified from (Lim et al, 2018).

Similar to the symmetrical model of dimeric GCAP1 reported by *Lim et al*[62], the structure of the GCAP5 dimer (Fig. 3.3.16A) contains conserved intermolecular contacts between mostly

hydrophobic residues (H18, Y21, M25, F72, V76 and W93) at the dimer interface (Fig. 3.3.15B-C and Fig. 3.3.16A-B). The closest contacts are formed between the hydrophobic side chain atoms of H18, M25, F72, V76 and W93 (highlighted red in Fig. 3.3.16A). The intermolecular contacts with V76 are consistent with the previous observation that a V77E mutation abolished dimerization of GCAP1 [53]. The aromatic side chain atoms of H18, Y21 (not shown), F72 and W93 make intermolecular contacts with each other at the dimer interface (Fig. 3.3.16B). The GCAP5 dimer is also stabilized by an intermolecular salt bridge between the side chain atoms of R22 and D71 (Fig. 3.3.16C). The GCAP5 dimer (Fig. 3.3.16A) is structurally quite similar to the dimeric structural model reported recently for GCAP1 (Fig. 3.3.15A)[62].

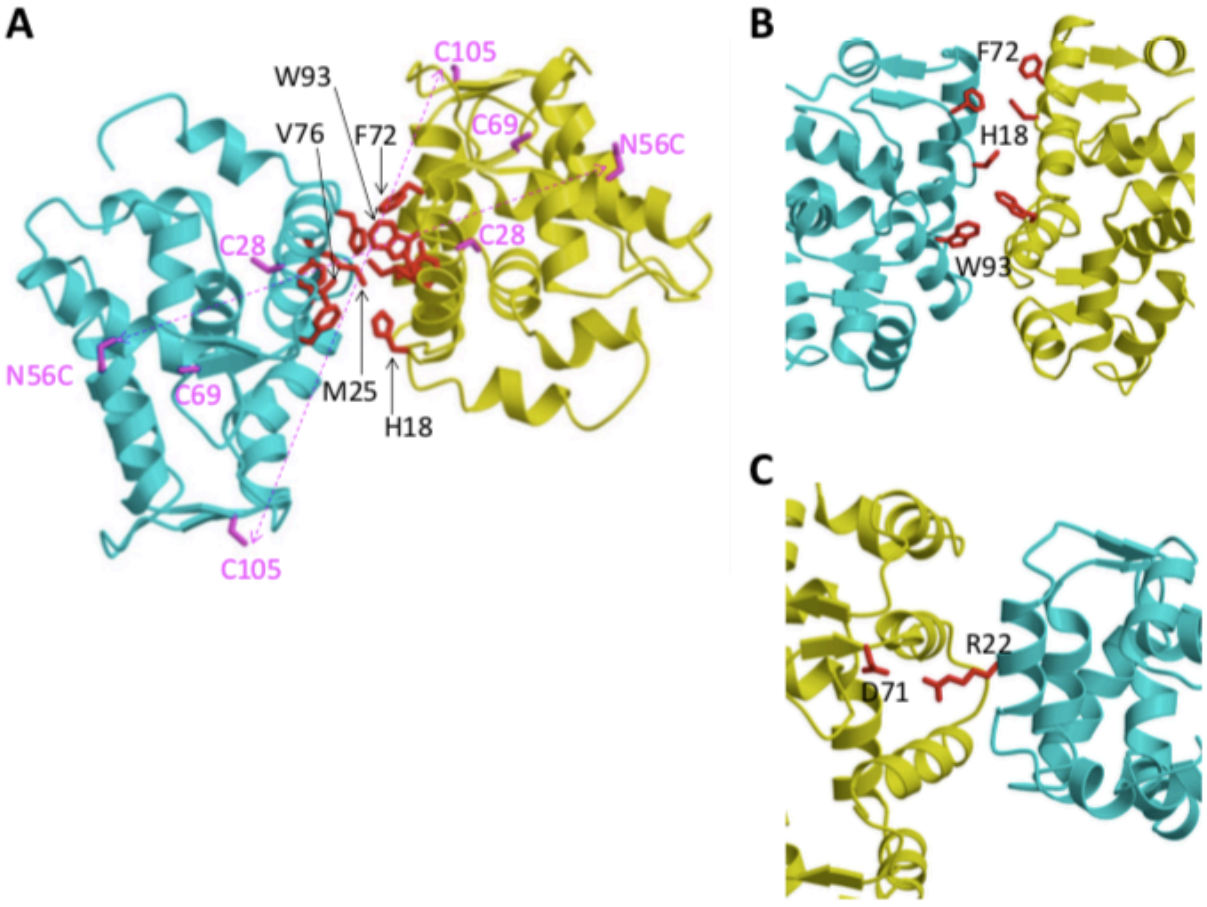

Fig. 3.3.16. Dimeric structure of GCAP5. (A) Ribbon diagram of dimeric GCAP5 calculated based on the EPR-DEER intermolecular distances in table 3.3.2. Monomeric units are colored in

cyan and yellow while representing EPR-DEER mutants in pink and dimerization site in red. (B) Expansion view of residues at the dimerization site (H18, F72 and W93) consistent with previously GCAP1 dimer (H19, F73 and W94). (C) Intermolecular salt bridge observed between in R22 and D71 in GCAP5 dimer [101].

Interestingly, Cys15 and Cys17 reported an intermolecular distance of 32 and 28 Å (Fig. 3.3.17), respectively, indicating these residues are not spatially close in the dimer, in contrast to what was reported for a previous structural model of the Fe^{2+}-bound GCAP5 dimer [88, 100]. This critical difference in the intermolecular distances for Cys15 and Cys17 suggests an Fe^{2+}-induced conformational change at the dimeric interface [101].

Table 3.3.2. Molecular docking statistics for GCAP5 by EPR-DEER

Residue (Sγ atom)	DEER distance (Å)	Calculated distance (Å)
C15	25 ± 6	32
C17	17 ± 2	28
T26C	17 ± 5	16
C28	16 ± 1	21
N56C	52 ± 3	52
C69	41 ± 3	39
C105	33 ± 5	41
N139C	55 ± 4	57
E152C	45 ± 5	42
E156C	43 ± 5	37
S159C	41 ± 3	42
HADDOCK Energy	-181.3 ± 5.8	-
RMSD (Å)	0.9 ± 0.6	-
Cluster size	10	-

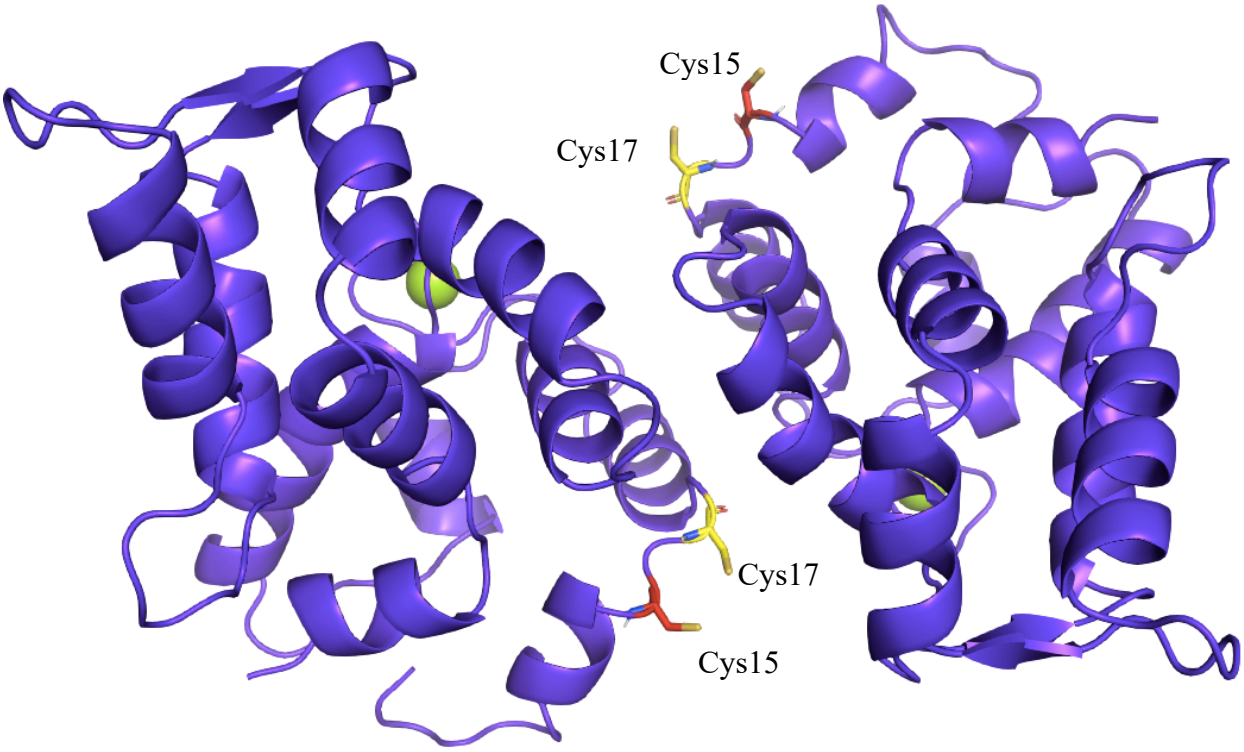

Fig. 3.3.17. Structural model of dimeric GCAP5 by EPR-DEER analysis. Main chain structure of Mg^{2+}-bound dimeric GCAP5 with C15 (red) and C17 (yellow) represented in sticks. Model shows large distance between C15 and C17 per monomer (32 and 28 Å, respectively) and is structurally different from reported GCAP5 homology dimer [88, 101].

Validation of Dimeric GCAP5 Structure by Site-directed Mutagenesis

The key residues at the dimeric interface (H18, Y21, R22, M25, D71, F72, V76, and W93) were mutated to validate the dimeric structure of GCAP5 to the following constructs: H18E, H18E/Y21E, R22D, D71A, F72E, V76E, and W93E [62, 101]. The corresponding residues in GCAP1 were conserved at the dimeric interface (Y22E, M26E, F73E, V77E, and W94E) and confirmed to weaken dimer stabilization and abolish cyclase activation (see fig. 3.3.8. and 3.3.16) [62, 101]. Fig. 3.3.18 shows that the GCAP5 dimerization site mutants (D71A, F72E, V76E, and W93E) were expressed as insoluble and aggregated protein (termed inclusion bodies) as shown in total lysate and supernatant lanes by SDS-PAGE screening. As a result, this low solubility of the select

dimerization mutants suggests that the mutations may have caused protein unfolding due to the destabilization the dimer interface in GCAP5 (fig. 3.3.18). However, GCAP5 dimerization site double mutant (H18E/Y21E) and single mutants (R22D and M25E) were more soluble than the rest (see fig. 3.3.18) and were used for validation of dimeric GCAP5 by SEC-MALS analysis [101].

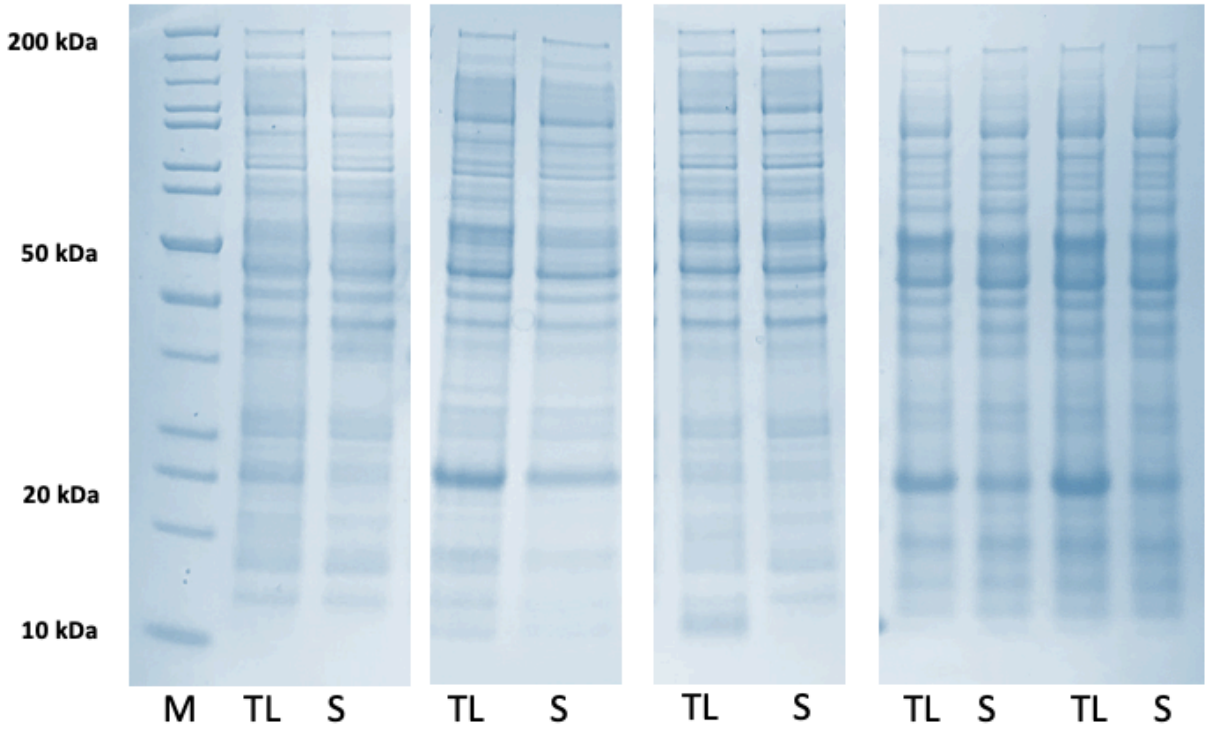

Fig. 3.3.18. SDS-PAGE of GCAP5 dimerization site mutants. Representative mutants were screened by SDS-PAGE for expression in the following: D71A, F72E, W93E, R22D, and M25E. For every mutant, TL is the total lysate and S is the supernatant after centrifugation. All mutants, except for R22D and M25E, were shown to form inclusion bodies while R22 and M25E are more soluble than other mutants.

Characterization of GCAP5 Dimerization Mutants

The more soluble GCAP5 dimerization mutants, H18E/Y21E, R22D and M25E, were overexpressed and purified as previously described [88, 100, 101]. These mutants were heterogenous throughout the purification, however, I was able to isolate and resolve a fraction of GCAP5

mutants used for NMR and SEC-MALS to validate the dimeric structure by determining the molecular weight via SEC-MALS analysis.

Purification of all soluble GCAP5 dimerization mutants were lower-yielding than wild-type and EPR-DEER mutants, which made it challenging to isolate a highly homogenous sample for NMR and SEC-MALS analyses. The double mutant (H18E/Y21E), as shown in fig. 3.3.19, shows heterogeneity seen on Q anion-exchange chromatogram, identifying two different GCAP5 species (fraction #12-13 and #15-18) unlike wild-type studies. Fig. 3.3.19 detected higher molecular weight impurities and/or stubborn aggregates by gel that was seen across all purification. In addition, GCAP5^{M25E} dimerization site exhibited similar purification results as the double mutant.

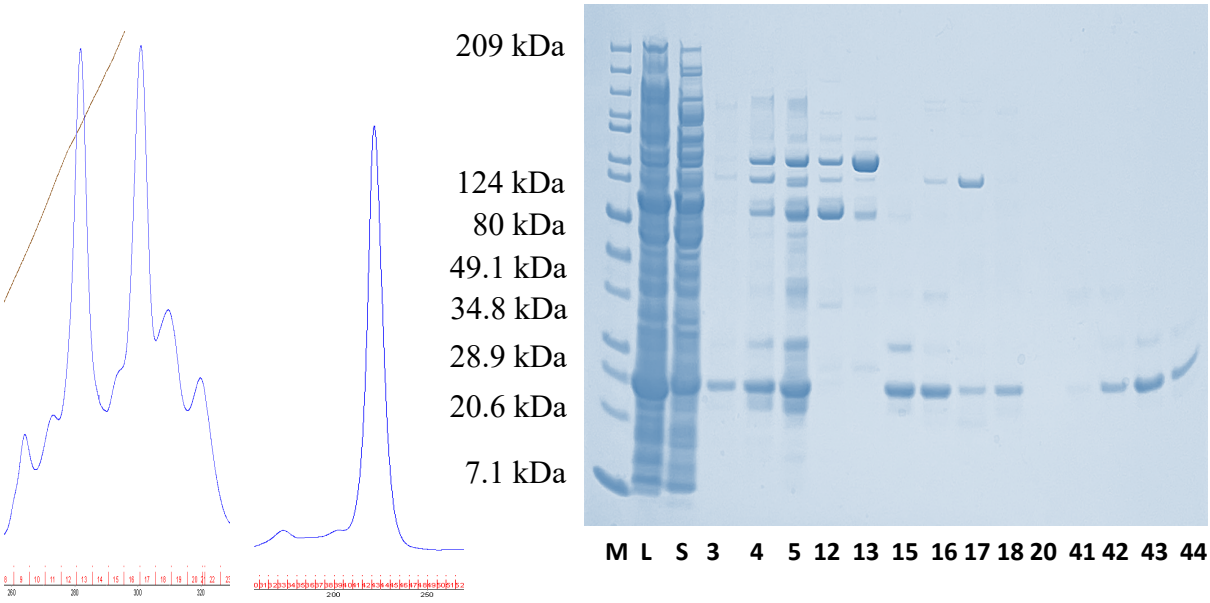

Fig. 3.3.19. GCAP5$^{H18E/Y21E}$ dimerization site mutant FPLC and SDS-PAGE. FPLC Chromatograms (Q IEC (*left*) and SEC (*right*)) as a monomer and gel profile showing heterogeneity in dimerization site mutant H18E/Y21E seen across purification. L is total lysate, S is supernatant after centrifugation, fractions #3-5 represent HIC, fractions #12-20 represent Q IEC, and fractions #41-44 represent SEC.

The dimerization mutant, GCAP5^{R22D}, involved in an intermolecular salt bridge between D71 unique to GCAP5 homolog is thought to also stabilize dimerization as well. Fig. 3.3.20 shows a more soluble mutant that yielded a highly purified and homogenous sample, which was also observed in SEC-MALS analysis.

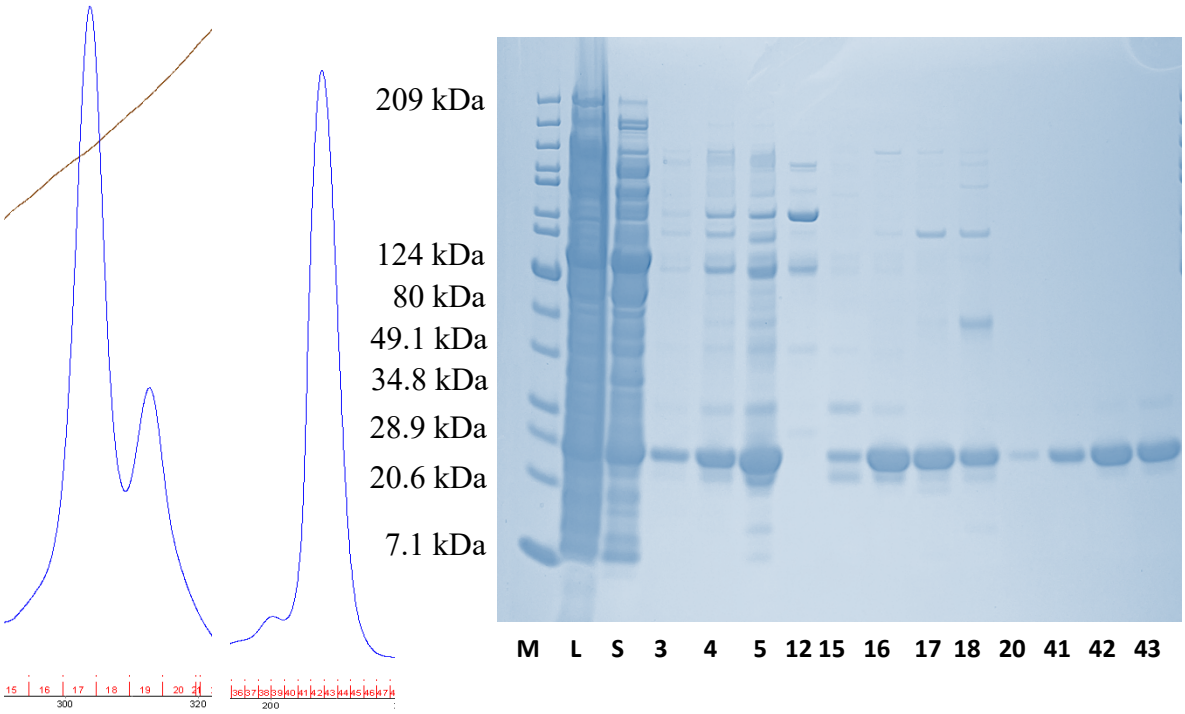

Fig. 3.3.20. Purification and SDS-PAGE of GCAP5^{R22D} dimerization site mutant. FPLC chromatograms (Q (*left)* and SEC (*right*)) as a monomer and gel profile shows well-resolved and high-yielding purification. L is total lysate, S is supernatant after centrifugation, fractions #3-5 represent HIC, fractions #12-20 represent Q IEC, and fractions #41-43 represent SEC.

^{15}N-labeled GCAP5^{M25E} and GCAP5$^{H18E/Y21E}$ samples were analyzed by NMR to detect any differences from wildtype studies. The HSQC of the ^{15}N-labeled GCAP5^{M25E} observed a similar HSQC spectrum, however, peak broadening was observed in residues at or near dimerization site and suggest the mutation might have weakened dimerization (fig. 3.3.21A) [101]. Moreover, the HSQC of GCAP5$^{H18E/Y21E}$ unveiled a mixture of oligomers of GCAP5 present in the sample (fig. 3.3.21B) [101]. The most downfield peak assigned to G68 (labeled and circled in fig.

3.3.20A/B) exhibited four other peaks, which confirmed the double mutant sample is heterogenous [101].

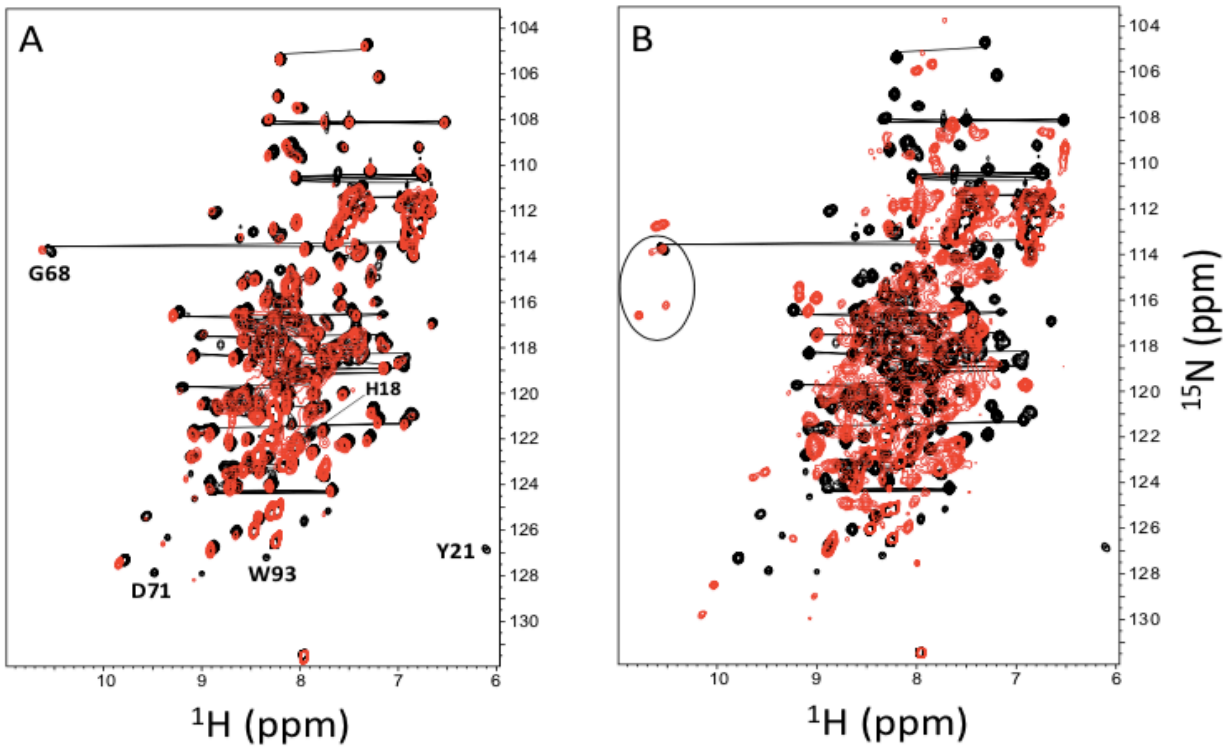

Fig. 3.3.21. ^{15}N HSQC spectra overlay of dimerization site mutants and wildtype GCAP5. (A) ^{15}N-labeled GCAP5^{M25E} (red) and (B) ^{15}N-labeled GCAP5$^{H18E/Y21E}$ (red) both overlaid with GCAP5 wildtype (black). Both mutants exhibit peak broadening at or near the dimeric site, and higher order oligomers observed in the double mutant sample (H18E/Y21E) [101].

In addition to the NMR analysis of the dimerization mutants, I also performed SEC-MALS analysis to quantify the absolute molar mass to determine whether these mutants affect the dimerization of GCAP5. Similar to previous GCAP1 studies, corresponding residues at the dimer interface (Y22E, M26E, F73E, V77E, and W94E) were proven to weaken the dimerization and abolish cyclase activation [62]. According to SEC-MALS, both mutants (H18E/Y21E and R22D) of GCAP5 were quantified to have a molar mass of around 23 kDa, which verifies that these mutants disrupted the dimeric structure of GCAP5 (fig. 3.3.22) [101].

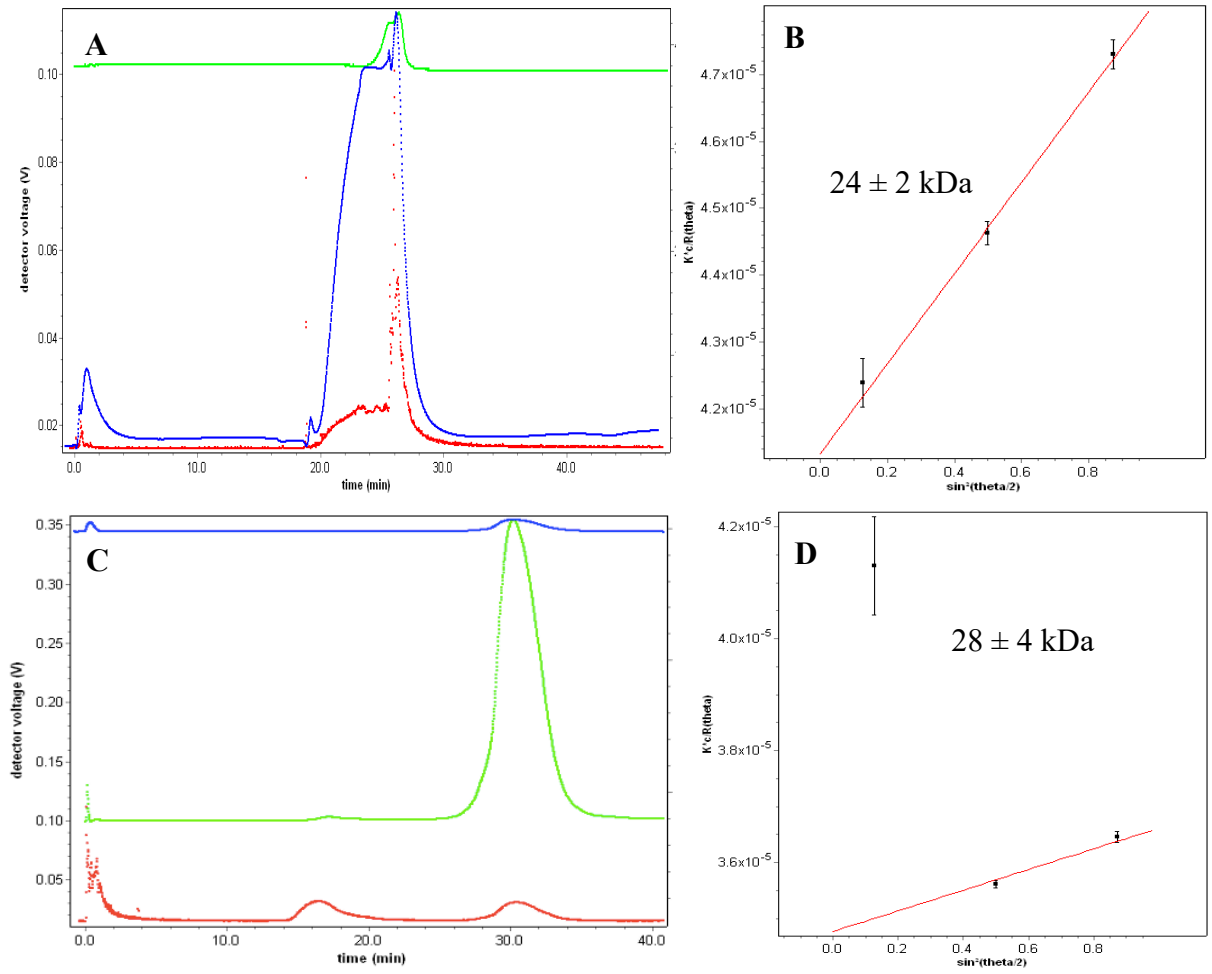

Fig. 3.3.22. Batch-mode and SEC-MALS analysis of GCAP5$^{H18E/Y21E}$ and GCAP5^{R22D}. Batch-mode MALS and Zimm plot of (A-B) the double mutant H18E/Y21E quantified as 24 ± 2 kDa and (C-D) SEC-MALS and Zimm plot of the R22D mutant quantified as 28 ± 4 kDa [101].

3.4 Discussion

Fe^{2+}-bound GCAP5 Inactivates RetGC in Zebrafish Phototransduction

Dr. Koch's *in vitro* functional studies on the cyclase regulation by GCAPs confirmed that Fe^{2+} binding to GCAP5 (ligated to non-conserved Cys15 and Cys17) caused a ten-fold decrease in cyclase activation (fig. 3.3.1) [88]. However, these experiments were done with recombinant mammalian cyclase (GC-E) that exhibited Fe^{2+}-induced inhibition by both bovine GCAP1 and zebrafish GCAP5 (fig. 3.3.1 and 3.4.1) [88]. The Fe^{2+}-induced inactivation of the cyclase in the

presence of Ca^{2+}-free GCAP1 is likely an artifact of Fe^{2+} binding to the EF-hands of GCAP1, because Fe^{2+} can mimic Ca^{2+} binding to the EF-hands. The Fe^{2+} binding to the EF-hands of GCAPs is most likely not physiologically important, because physiological Fe^{2+} levels are too low to enable the relatively low affinity Fe^{2+} binding to the EF-hands. By contrast, the potent 10-fold inhibition of the cyclase caused by Fe^{2+}-binding to GCAP5 is suggested to be physiologically relevant, because Fe^{2+} can bind to GCAP5 under physiological conditions in the nanomolar range. Surprisingly, wildtype GCAP5 did not exhibit a typical Ca^{2+}-sensitive regulation of the cyclase (fig. 3.3.1) in contrast to that of GCAP1 (Fig 3.4.1). This is in stark contrast to the GCAP5 double mutant (Cys15A/Cys17A), which restored the Ca^{2+}-dependent regulation of the cyclase. These results suggest that Fe^{2+} binding to GCAP5 may somehow prevent the Ca^{2+}-induced conformational changes in GCAPs that regulate the cyclase, and Fe^{2+} binding to GCAP5 may serve to constitutively inactivate the cyclase (fig. 3.3.1) [88]. Future studies are needed to determine the atomic level structure of GCAP5 with both Fe^{2+} and Ca^{2+} bound to better understand how Fe^{2+} binding might be allosterically coupled to Ca^{2+} binding.

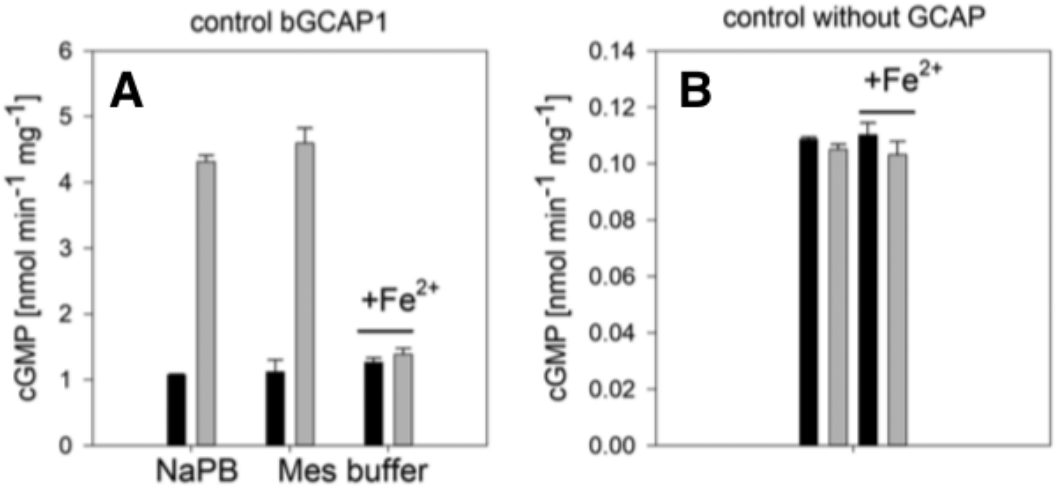

Fig. 3.4.1. Fe^{2+} induced inhibition observed in GCAP1. Gray bars indicated cyclase activity at low Ca^{2+} levels (10 nM). Black bars indicate cyclase activity at high Ca^{2+} levels (1.5 μM). Addition of Fe^{2+} in bovine GCAP1 caused a decrease in cyclase activation, which may suggest

Fe^{2+} binding to EF-hands to mimic Ca^{2+}-induced inhibition[88]. Figure previously published from (Lim et al, 2017) DOI:10.1021/acs.biochem.7b01029.

Structural Model of Fe^{2+}-bound GCAP5

A structural model of Fe^{2+}-bound GCAP5 dimer was proposed previously [88], which is hypothesized to form a [98] complex with a single bound Fe^{2+} ligated by the four sulfur atoms from Cys15 and Cys17 in a symmetric dimer (Fig. 3.4.2). A similar [98] structural motif was reported previously in the crystal structures of rubredoxin [98] and a two-iron superoxide reductase [117]. However, my SEC data on GCAP5 (Fig. 3.3.4) indicate that both Fe^{2+}-free and Fe^{2+}-bound GCAP5 exist as a dimer in solution, which indicates that GCAP5 dimerization does not require Fe^{2+} binding. A structural model of the Fe^{2+}-bound GCAP5 homology dimer[88] (Fig. 3.4.2) suggests intermolecular protein hydrophobic contacts (between His18 and Val76) as well as an intermolecular hydrogen bond (between Lys84 and Gln88) may also stabilize GCAP5 as a pre-formed protein dimer in the Fe^{2+}-free state. The intermolecular contact involving Val76 was also implicated in the dimerization of GCAP1, because mutating this Val residue to Glu abolishes dimerization of GCAP1[53].

The bound Fe^{2+} in GCAP5 is coordinated by four cysteinyl thiolate atoms that is quite similar to the structure of a bound Zn^{2+} in a Cys4 zinc finger motif (Fig. 3.4.2) [118]. This structural similarity suggests that Zn^{2+} might bind to GCAP5 in place of Fe^{2+} at the high affinity site. Zn^{2+} is transported into retinal photoreceptor cells and has been suggested to play a role in phototransduction [119]. Future studies are needed to probe whether Zn^{2+} can replace Fe^{2+} and bind with nanomolar affinity to GCAP5. If so, then it will be interesting to test whether Zn^{2+} binding to GCAP5 (like Fe^{2+} binding) can also regulate zGCs during visual phototransduction.

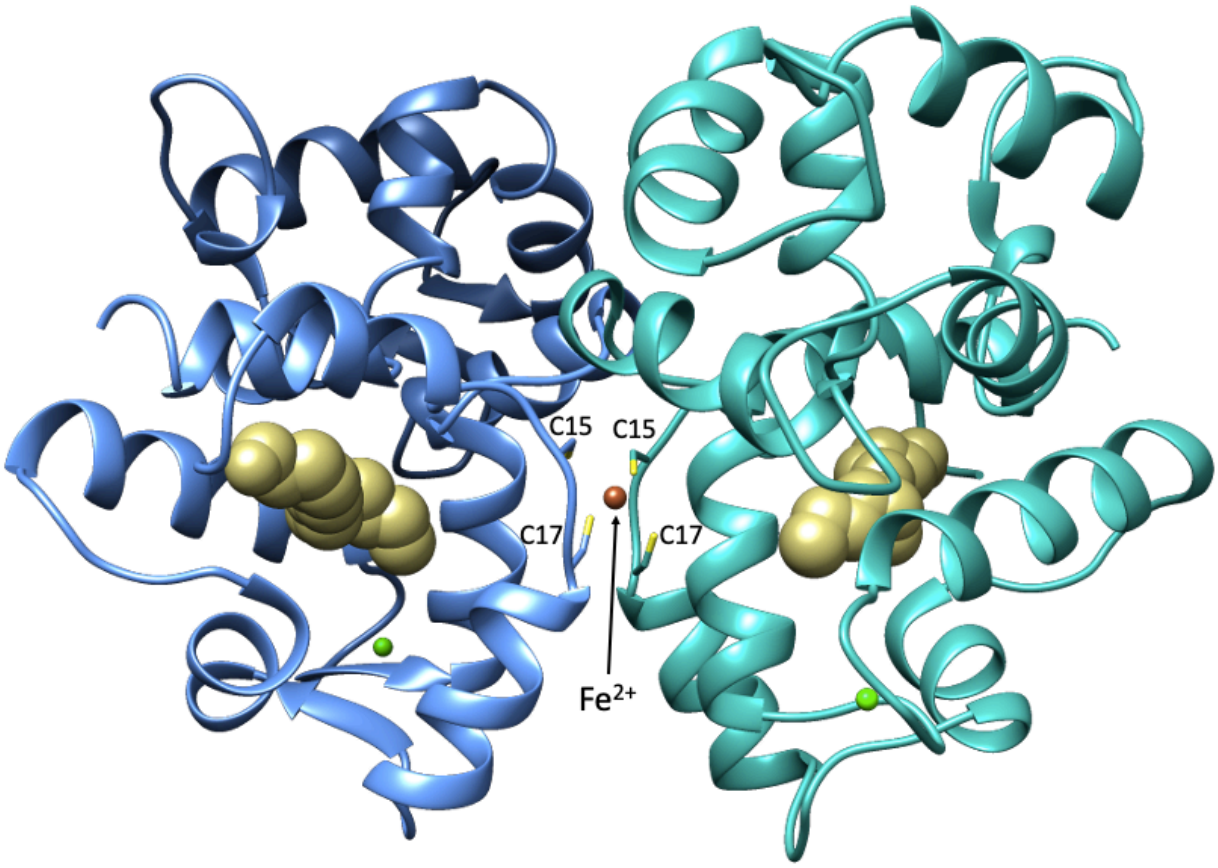

Fig. 3.4.2 Structural model of Fe^{2+}-bound GCAP5 dimer. Model of dimeric Fe^{2+}-bound GCAP5 based on the crystal structure of Ca^{2+}-bound GCAP1 (PDB ID: 2R2I) and iron-sulfur distances set to 2.35 ± 0.05 Å from rubredoxin (PDB ID: 1FHM) [88].

Fe^{2+}-induced Conformational Changes in GCAP5

The structure of the Ca^{2+}-free/Fe^{2+}-free/Mg^{2+}-bound GCAP5 dimer (Fig. 3.3.15 and 3.3.16) is quite different from a structural model of the Fe^{2+}-bound GCAP5 dimer proposed previously (Fig. 3.4.2) [88]. In the Fe^{2+}-bound GCAP5 dimer, a single Fe^{2+} is chelated by the sulfhydryl side chains of Cys15 and Cys17 from each subunit of the GCAP5 dimer so that the intermolecular distance of the sulfhydryl atoms for Cys15 is less than 8 Å apart (see double arrow in Fig. 3.4.3). By stark contrast, in the Fe^{2+}-free GCAP5 dimer, the intermolecular distance of nitroxide spin-label attached to Cys15 is 24 Å. The much larger intermolecular distance for Cys15 in the Fe^{2+}-

free GCAP5 dimer suggests that Fe^{2+} binding to the GCAP5 dimer may cause the two protein subunits within the dimer to rotate with respect to one another as illustrated in Fig. 3.4.3. This Fe^{2+}-induced rotation of the two protein subunits in the GCAP5 dimer dramatically alters the exposure of residues (P29, S30, G31 and M73 highlighted by red ovals in Fig. 3.4.3) that have been implicated in binding to guanylate cyclase [54]. I propose that the Fe^{2+}-dependent exposure of the cyclase binding site residues may explain how Fe^{2+}-binding to GCAP5 prevents its activation of guanylate cyclase. Future studies are needed to determine the atomic resolution structures of Fe^{2+}-bound GCAP5 and GCAP5 bound to guanylate cyclase to further test this model. In addition, a future experiment that combines NMR and small angle X-ray scattering (SAXS) analysis may allow us to confirm if there is indeed a Fe^{2+}-induced rotation at the dimeric interface of GCAP5 as I have proposed below (Fig. 3.4.3.).

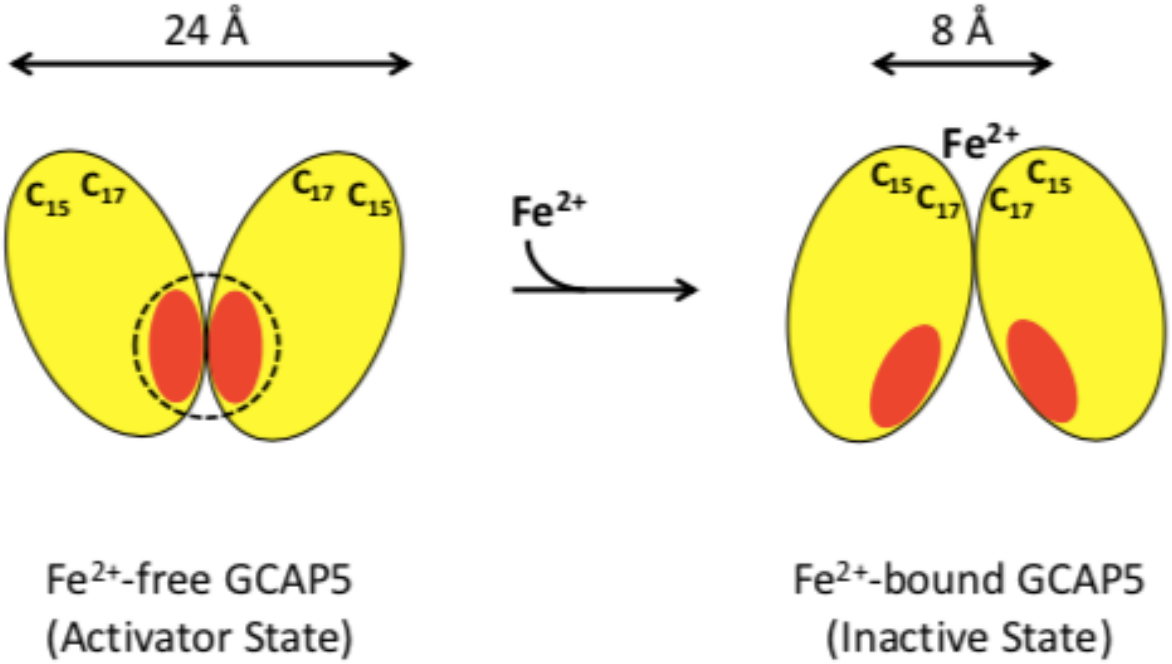

Fig. 3.4.3. Fe^{2+}-induced rotation at the dimeric interface in GCAP5. A representation of Fe^{2+}-induced conformational changes in GCAP5 that depicts the binding interactions of the dimeric site residues (H18, Y21, M25, F72, V76, and W93) represented by the red ovals and the current mapping of the cyclase binding site in GCAP5 (dashed circle) [101].

Functional Implications for the Dimerization of GCAP Proteins

RetGC is a functional dimer (Fig. 1.4.6) that is believed to form a 2:2 complex with dimeric GCAPs [62, 120, 121]. The GCAP proteins (GCAP1 and GCAP5) dimerize in solution in the absence of RetGC, and the dimerization of GCAPs is essential for their ability to activate RetGC [62]. The dimeric structures of GCAP1 [62] and GCAP5 (this study) both reveal exposed hydrophobic residues at the dimer interface (H19, Y22, F73, V77, and W94) that are essential for dimerization. In particular, the V77E mutant in GCAP1 abolishes dimerization and the structure of the monomeric V77E mutant was solved by NMR [53, 62]. The dimeric structures of GCAP1 and GCAP5 are overall quite similar and contain the same hydrophobic residues at the dimerization site (H18, Y21, M25, F72, V76 and W93) as seen in fig. 3.3.15A/B [62, 101]. The dimerization site mutations (H19E, Y22E, M26E, F73E, V77E and W94E) in GCAP1 were shown previously to weaken dimerization and abolish activation of the cyclase [62]. The corresponding mutations in GCAP5 (H18E, Y21E, M25E, F72E, V76E and W93E) were also proven to weaken protein dimerization (Fig. 3.3.21). The F72E, V76E and W93E mutants in GCAP5 were insoluble (fig. 3.3.17) and suggest that these mutations may have caused protein unfolding by destabilizing the GCAP5 dimerization. Of the GCAP5 dimerization site mutants I created, there were only three that were soluble enough to move forward with analysis: H18E/Y21E, R22D and M25E [101]. These soluble mutants were quantified to be monomeric (23-kDa) by SEC-MALS (fig. 3.3.21) as compared to the dimeric wild type GCAP5 (42-kDa) [88, 101]. Additionally, the ^{1}H-^{15}N HSQC spectra of the double mutant (H18E/Y21E) and M25E exhibited selective NMR peak broadening of residues in the dimerization site (shown in fig. 3.3.20), which could be due to a weakening of the dimerization [101].

An important structural difference between the dimeric forms of GCAP1 and GCAP5 is that the GCAP5 dimer is stabilized by an intermolecular salt bridge between R22 and D71 (Fig.

3.3.15C) that is not seen in the GCAP1 dimer structure, perhaps because R22 in GCAP5 is replaced with a lysine in GCAP1. Slight differences in the quaternary structures of dimeric GCAP1 and GCAP5 may explain the 3 Å increase in the intermolecular distance between K22 and D71 in GCAP1[62] compared to the much shorter salt bridge distance in GCAP5 (Fig. 3.3.15C). We suggest that this difference in quaternary structure for GCAP1 and GCAP5 might explain why GCAP1 is 3-fold more potent at activating guanylate cyclase [88].

The dimerization site mutants in GCAP1 (H19E, Y22E, M26E, F73E, V77E and W94E) weaken dimerization and disrupt functional contacts to the cyclase. Intriguingly, the point mutation H19Y in human GCAP1 was discovered in patients who suffer from *retinitis pigmentosa (RP)* [101, 122]. RP is a group of rare, inherited diseases associated to progressive retinal degeneration and may cause impairment in peripheral and night vision [123]. Abbas et al discovered that the H19Y point mutation in GCAP1 causes a disruption in the Ca^{2+} binding of GCAP1 and in turn changes the dimerization and overall cyclase activation [101, 122]. Hence, the H19Y point mutation in GCAP1 and any mutations at the dimeric interface in GCAP1 and GCAP5 are hot spot residues that could provide insights into designing drugs to target these retinal degenerative diseases.

Appendix

Buffer Recipe

Listed below are common buffers and solutions I have used for protein sample preparations (expression, purification, etc.). All growth media are autoclaved and buffers are filtered before use.

Luria Broth (LB): 25 g/1 L MQ-H_2O
Minimal 9 (M9): Buffer prepared in two-part process

Part I:	12.66 g Na_2HPO_4•$7H_2O$	0.50 g Nacl
	3.00 g KH_2PO_4	1.00 g NH_4Cl (unlabeled or ^{15}N-labeled)
Part II:	1 mL of 1M $MgSO_4$ stock	50 µL of 1M $CaCl_2$
	20 mL glucose (3-4 g/20 mL)*	1000x antibiotics
	1 mL trace metals*	

1. Prepare part I with ~980 mL MQ-H_2O and autoclave.
2. Part II stock solutions must be filtered before adding to part I.
3. If glucose is unlabeled, dissolve 4 g in 20 mL MQ-H_2O. If glucose is ^{13}C-labeled, dissolve 3 g in 20 mL MQ-H_2O

KCl/lysis buffer: 20 mM Tris-HCl (pH 8.3), 0.1 M KCl, 0.35 M $(NH_4)_2SO_4$, 2 mM EGTA, 1 mM DTT, 10% glycerol, 0.1 mM PMSF

TEM/lysis buffer: 10 mM Tris-HCl (pH 8.3), 0.5 mM EDTA, 14 mM BME

TEM/8 M urea buffer: 10 mM Tris-HCl (pH 8.3), 2 mM EDTA, 14 mM BME, 8M urea

NMR tris/D_2O buffer (pH 7.4): 10 mM Tris-d_{11}, 3 mM DTT-d_{10}, 50 µM EDTA-d_{12}, 0.04% w/v NaN_3, and 93% H_2O/7% D_2O

NMR MES buffer (pH 6.5): 5 mM MES, 3 mM dithiothreitol-d_{10} (DTT-d_{10}), 2 mM $MgCl_2$, 0.04% w/v NaN_3, and 93% H_2O/7% D_2O

1000x Ampicillin stock: 100 mg/mL MQ-H_2O
1000x Kanamycin stock: 50 mg/mL MQ-H_2O
1M DTT: 1.542 g/10 mL MQ-H_2O *(MW = 154.253 g/mol)*
1M IPTG: 2.3831 g/10 mL MQ-H_2O *(MW = 238.31 g/mol)*
Myristic acid: 10 mg/1 mL pure ethanol
5M NaCl: 292.2 g/1 L MQ-H_2O *(MW = 58.44 g/mol)*
3M KCl: 223.653 g per 1 L MQ-H_2O *(MW = 74.551 g/mol)*
8M Urea: 480.48 g per 1 L MQ-H_2O *(MW = 60.06 g/mol)*
4M $(NH_4)_2SO_4$ (pH X): 528.56 g per 1 L MQ-H_2O *(MW = 132.14 g/mol)*
0.5 M EGTA (pH 8.0): 190.18 g per 1 L MQ-H_2O *(MW = 380.35 g/mol)*

Single or Double Transformation (DH5α or BL21(DE3))

1. Thaw bacteria competent cells (50 µL) and plasmid DNA on ice for ~10-30 minutes.
2. Add 1-5 µL plasmid DNA (up to ~100 ng) into competent cells and mix gently by flicking bottom of the tube.
3. Incubate transformation tube on ice for 30 minutes.
4. Heat shock by placing transformation tube in a 42°C dry bath for 45 seconds (do not go over 60 seconds).
5. Let it cool on ice for 2 minutes.
6. Add 150-400 µL SOC or LB media (without antibiotic) to the transformation tube and incubate in 37°C shaking incubator for 1 hour minimum.
7. Plate 100-250 µL transformed cells onto LB agar plate with appropriate antibiotic(s).
8. Incubate plate at 37°C overnight (12-18 hours).

Preparation of Glycerol Stocks

General Protocol for GCAPs *E. coli* glycerol stocks for GCAP5 Protein Expression

1. Choose an isolated colony on LB-agar/antibiotics plate. Inoculate in a 2 mL autoclaved LB and 1000x filtered antibiotic(s). (GCAPs require NMT – ampicillin and kanamycin needed). Incubate the pre-/starter culture at 37°C in a shaking incubator until OD_{600} is 1.0.
2. Inoculate the preculture into a 10 mL autoclaved LB with filtered 1000x antibiotics and incubate the expansion/main culture at 37°C in a shaking incubator until OD_{600} is 1.2.
3. Stop incubation and add 2 mL 80% glycerol to main culture (glycerol is a cryoprotectant). **Bacteria can be stored in 15-25% glycerol.**
4. Aliquot to 1mL stocks in labeled cryogenic tubes and flash freeze with liquid N_2 before storing in -80°C freezer.

Fast Protein Liquid Chromatography

After cells have been lysed and protein of interest is isolated by ultracentrifugation, protein is purified using AKTA FPLC systems. Below is a general protocol on how to wash and equilibrate FPLC for protein purification.

1. Turn purge ON for pumps A and B. Click end when finished (flow = 0.0 mL/min).
2. Wash lines with filtered MQ-H_2O with the following parameters:
    a. **Flow** = 2.0 mL/min
    b. **Column position** = 8
    c. **End timer (volume)** = 2 CV
3. Attach the desired column at previously washed line (from step 2) and wash again with column attached with the same parameters from step 2.
4. Manually wash sample inlet/line by removing tube from injection valve. Attach plastic syringe with MQ-H_2O and flow through. Re-attach tube to injection valve before removing syringe.
5. Directload_960 (1-2 mL/min, ~10-20 mL) with MQ-H_2O and then buffer A.
6. Transfer pumps A and B to running and elution buffers, respectively. Turn purge ON for pumps A and B. Click end when finished.
7. Click RUN to start. Select appropriate method for purification.

Regenerating FPLC Columns *on the lab bench*

To ensure no cross-contamination occurs between different protein purification(s), regenerating FPLC columns such as HIC and Q are highly recommended to preserve the column's efficiency and reliability during an extended period of time. After every FPLC run, column is assumed contaminated with trace amounts of impurities (salts, proteins, buffers, etc.) and hence, it is vital to regenerate columns before utilizing them with a new protein purification.

Although there are several protocols for regenerating columns that can be found online, this is what I have followed throughout my graduate research *(suggested CV below are my recommended minimum):*

HIC (~20 ml = 1 CV):
1. 2-4 CV MQ-H_2O
2. 2-3 CV 8 M urea (filtered)
3. 4-5 CV MQ-H_2O
4. 1-2 CV 20-50% ethanol
5. 3-4 CV MQ-H_2O

Q (~5 ml = 1 CV):

1. 2-4 CV MQ-H_2O
2. 2-3 CV 8 M urea + 1M NaCl (filtered)
3. 4-5 CV MQ-H_2O
4. 1-2 CV 20-50% ethanol
5. 3-4 CV MQ-H_2O

After every regeneration done on the lab bench, wash the column twice with (a) MQ-H_2O and (b) running buffer once attached to FPLC instrument (flow = 2 mL/min, ~2-3 CV).

For SEC column, wash the attached column with at least 2 CV MQ-H_2O overnight or at the day of use. Set equilibrate column value to 2-3 CV for equilibrating the column with elution buffer before sample run.

Multi-angle light scattering (MALS)

Light scattering is a precise method to determine the molecular weight of protein of interest. There are two modes couple MALS: size exclusion (SEC-MALS) and batch-mode MALS.

SEC-MALS General Protocol

1. Turn COMET (sonicator) ON overnight to clean the flow cell. Turn OFF before the experiment.
2. Turn laser ON 30 minutes to an hour before experiment.
3. Turn MALS purge ON and wash MALS sample cell by FPLC:
    a. **Flow rate:** 0.5 mL/min
    b. **Column position:** 3
    c. **Outlet position:** F7
    d. **End timer (volume):** 50 mL minimum
4. Equilibrate MALS by FPLC:
    a. **Flow rate:** 0.5 mL/min
    b. **Column position:** 3
    c. **Outlet position:** F7
    d. **End timer (volume):** 50 mL minimum
5. Set up new experiment run: file > new > from default
6. Before running experiment, turn purge OFF.

7. Set the following FPLC parameters after sample loaded:
    a. **Flow rate:** 0.5 mL/min
    b. **Column position:** 3
    c. **Outlet position:** F7
    d. **End timer (volume):** 50 mL minimum
8. Click start experiment. Switch FPLC injection valve to INJECT and then press OK on MALS to begin.

FPLC sample loading:

1. Wash sample loop (1-5 mL) with filtered MQ-H_2O.
2. Attach a 1 mL syringe on flow-out tube to close system.
3. Switch injection valve to INJECT before removing syringe containing MQ-H_2O.
4. Swap with 1 mL syringe with filtered protein sample. Switch injection valve back to LOAD.
5. Manually load/inject sample in sample loop slowly.

Batch-mode MALS

1. Repeat general protocol #1-2 (turn ON comet overnight and turn ON laser ½-1 h before experiment).
2. Attach outlet valve #7 (or FPLC outlet valve line connected to FPLC and MALS) with a 0.22 µM filter and syringe. Ensure MALS purge is ON.
3. Storage solution is 20% ethanol. Run 2-3 10 mL B-D syringe with filtered MQ-H_2O using syringe pump. Repeat washing with desired loading/blank buffer. Check miniDAWN for baseline stability. Stop washing when baseline stabilizes within ~0.015 V and noise is below 0.1 mV for good equilibrium.
    a. Set up syringe pump:
        i. Click on rate and use any of the arrows to change units (i.e. ml/min, µl/min, etc.). Then, use arrow to set rate (i.e. 0.5 ml/min). Wait for LED to stop blinking.
        ii. Click on diameter and set diameter of syringe in use (refer to the back page of syringe pump manual for diameter).

iii. To run water through MALS via syringe pump, click START. Press STOP when syringe is near empty.
iv. DO NOT LEAVE SYRINGE PUMP ON WHEN SYRINGE IS EMPTY.

4. Set up experiment on ASTRA: file > new > from default.
5. When baseline is flattened and/or < 0.015 mV noise, you may run experiment.
6. Click on run on ASTRA and start for injection. Then, click on START on syringe pump.
    a. Run 1 syringe of loading buffer before and after sample injection.
    b. You may stop syringe pump when needed (i.e. change buffer to sample, change syringe diameter and rate)
7. When finished, run MQ-H_2O 2-3 times to rinse instrument and then 20% ethanol for storage.

EPR-DEER sample preparations

If the protein of interest is predicted to be a dimer, EPR-DEER studies provide additional distance restraints to aid in calculating the dimeric structure via online structural analysis software (i.e. HADDOCK). EPR-DEER samples must contain only one cysteine per monomer and require 3-4 days of preparation, which includes multiple buffer exchanges/dialysis and reaction for the nitroxide-spin labeling.

Day I: Initial buffer exchange/dialysis

After final purification via FPLC (protein sample in SEC buffer: 20 mM Tris, 0.1 M NaCl, 1 mM DTT, pH 8.3), an initial buffer exchange is done overnight in EPR-DEER day I buffer at 4°C with stirring.

Day I Buffer:

Final concentration	**4 L**	**8 L**
20 mM Tris-HCl (pH 7.5)	80 mL	160 mL
TCEP	0.8 mL	1.6 mL

Day II-III: Nitroxide-spin labeling and > 24 hour dialysis

After a preliminary dialysis, day II-III focuses on attaching the nitroxide spin-label to the single cysteine protein and further dialysis to remove unwanted impurities, solvents, salts, etc.

1. Measure protein concentration at 280 nm.
2. Add 20-50x MTSSL (40 mM stock in DMSO) in reaction tube and let it sit on ice for 30 minutes.
3. Transfer nitroxide-spin labeled protein in fresh and hydrated dialysis membrane.
4. Perform 2 x 4L dialysis at 4°C with spinning: (a) 3-5 hours and (b) over > 24 hours.

Day II Buffer:

Final concentration	**4 L**	**8 L**
20 mM Tris-HCl (pH 7.5)	80 mL	160 mL

Day IV: Sample preparation

Before exchanging nitroxide-spin labeled protein into DEER buffer, excess spin must be removed. This is done by 5-10x buffer wash with day II buffer using a 15 mL Amicon spin concentrator (10 kDa cutoff).

Final concentration	**50 mL**
10 mM Tris-d11	66.1 mg
2 mM $MgCl_2$	0.1 mL (1M $MgCl_2$ in D_2O)
99.9% D_2O	49.85 mL

EPR-DEER sample is exchanged into a 99.9% D_2O/Tris-d11 buffer at a minimum of 2x5mL before sample is transferred to an Eppendorf tube for sendoff for EPR-DEER measurements. Sample must be at least 150 µL with 50-150 µM protein. **Ideally, I send ~1 mL of labeled protein (200 – 500 µM) and 1 mL DEER D_2O buffer without glycerol-d8 (collaborator adds cryoprotectant before freezing sample).**

xPlor-NIH

Refinement script used for GCAP5 is provided below. There were 6 input files needed to run GCAP5 refinement calculations: *mg2.par, myr.top, GCAP5-homology.pdb (can use structure from an annealment calculation), dihedral.tbl, NOEs.tbl, and RDCs.tbl.*

To run the refinement calculation, use command: **xplor -smp 2 -py -o refine.out refine.py**

refine.py

```
xplor.requireVersion("2.34")

#
# slow cooling protocol in torsion angle space for protein G. Uses
# NOE, RDC, J-coupling restraints.
#
# this version refines from a reasonable model structure.
#
# CDS 2005/05/10
#


(opts,args) = xplor.parseArguments(["slow"]) # check for command-line typos

quick=True
for opt in opts:
   if opt[0]=="slow":  #specify -slow for full calc
      quick=False
      pass
   pass


outFilename = "SCRIPT_STRUCTURE.sa"
numberOfStructures=100

if quick:
  numberOfStructures=100
  pass

# protocol module has many high-level helper functions.
#
import protocol
protocol.initRandomSeed(3421)   #explicitly set random seed
```

```
#
# annealing settingsl
#

command = xplor.command
protocol.initTopology("myr.top")
protocol.initParams("mg2.par")
protocol.initParams("protein")

import psfGen
psfGen.residueTypes['protein'].append('MYR')
psfGen.residueTypes['protein'].append('MGL')

# generate PSF data from sequence and initialize the correct parameters.
#
#from psfGen import seqToPSF
#seqToPSF('gcap5-deleted180-198.seq')
#protocol.initStruct("gcap5.psf") # - or from file

# generate a random extended structure with correct covalent geometry
#  saves the generated structure in the indicated file for faster startup
#  next time.
#
#protocol.genExtendedStructure("gb1_extended_%d.pdb" %
#                              protocol.initialRandomSeed())

# or read an existing model
#
protocol.loadPDB("myrH-mg-gcap5H-2r2iHomology-correctedG2_MYRC1-1to184.pdb")
xplor.simulation.deleteAtoms("not known")

protocol.fixupCovalentGeom(maxIters=100,useVDW=1)

#
# a PotList contains a list of potential terms. This is used to specify which
# terms are active during refinement.
#
from potList import PotList
potList = PotList()

# parameters to ramp up during the simulated annealing protocol
#
from simulationTools import MultRamp, StaticRamp, InitialParams

rampedParams=[]
```

```
highTempParams=[]

# compare atomic Cartesian rmsd with a reference structure
#  backbone and heavy atom RMSDs will be printed in the output
#  structure files
#
#from posDiffPotTools import create_PosDiffPot
#refRMSD = create_PosDiffPot("refRMSD","name CA or name C or name N",
#                      pdbFile='myrH-gcap5H-2r2iHomology-correctedG2_MYRC1.pdb',
#                      cmpSel="not name H*")

# orientation Tensor - used with the dipolar coupling term
#  one for each medium
#   For each medium, specify a name, and initial values of Da, Rh.
#
from varTensorTools import create_VarTensor
media={}
#                    medium  Da   rhombicity
for (medium,Da,Rh) in [124]:
   oTensor = create_VarTensor(medium)
   oTensor.setDa(Da)
   oTensor.setRh(Rh)
   media[medium] = oTensor
   pass


# dipolar coupling restraints for protein amide NH.
#
# collect all RDCs in the rdcs PotList
#
# RDC scaling. Three possible contributions.
#   1) gamma_A * gamma_B / r_AB^3 prefactor. So that the same Da can be used
#      for different expts. in the same medium. Sometimes the data is
#      prescaled so that this is not needed. scale_toNH() is used for this.
#      Note that if the expt. data has been prescaled, the values for rdc rmsd
#      reported in the output will relative to the scaled values- not the expt.
#      values.
#   2) expt. error scaling. Used here. A scale factor equal to 1/err^2
#      (relative to that for NH) is used.
#   3) sometimes the reciprocal of the Da^2 is used if there is a large
#      spread in Da values. Not used here.
#
from rdcPotTools import create_RDCPot, scale_toNH
rdcs = PotList('rdc')
for (medium,expt,file,                scale) in \
   [('phage','NH' ,'RDCs-mg-myr-gcap5-d3n-100819.tbl'       ,1)
```

```
    ]:
   rdc = create_RDCPot("%s_%s"%(medium,expt),file,media[medium])

    #1) scale prefactor relative to NH
    #   see python/rdcPotTools.py for exact calculation
    # scale_toNH(rdc) - not needed for these datasets -
    #                   but non-NH reported rmsd values will be wrong.
    #3) Da rescaling factor (separate multiplicative factor)
    # scale *= ( 1. / rdc.oTensor.Da(0) )**2
   rdc.setScale(scale)
   rdc.setShowAllRestraints(1) #all restraints are printed during analysis
   rdc.setThreshold(1.5)       # in Hz
   rdcs.append(rdc)
   pass
potList.append(rdcs)
rampedParams.append( MultRamp(0.05,5.0, "rdcs.setScale( VALUE )") )
#
# calc. initial tensor orientation
# and setup tensor calculation during simulated annealing
#
from varTensorTools import calcTensorOrientation, calcTensor
for medium in media.keys():
    calcTensorOrientation(media[medium])
    rampedParams.append( StaticRamp("calcTensor(media['%s'])" % medium) )
    pass

# set up NOE potential
noe=PotList('noe')
potList.append(noe)
from noePotTools import create_NOEPot
for (name,scale,file) in [('all',1,"gcap5-noes-101019-ames.tbl"),
                    #add entries for additional tables
                    ]:
    pot = create_NOEPot(name,file)
    #pot.setPotType("soft") - #if you think there may be bad NOEs
    pot.setScale(scale)
    noe.append(pot)
rampedParams.append( MultRamp(2,30, "noe.setScale( VALUE )") )

# set up J coupling - with Karplus coefficients
#from jCoupPotTools import create_JCoupPot
#jCoup = create_JCoupPot("jcoup","jna_coup.tbl",
#                    A=6.98,B=-1.38,C=1.72,phase=-60.0)
#potList.append(jCoup)

# Set up dihedral angles
```

```
from xplorPot import XplorPot
protocol.initDihedrals("gcap5dihedral_041219-edited061919.tbl",
                useDefaults=False  # by default, symmetric sidechain
                                   # restraints are included
                )
potList.append( XplorPot('CDIH') )
highTempParams.append( StaticRamp("potList['CDIH'].setScale(10)") )
rampedParams.append( StaticRamp("potList['CDIH'].setScale(200)") )
#set custom values of threshold values for violation calculation

potList['CDIH'].setThreshold( 5 ) #5 degrees is the default value, though



# gyration volume term
#
# gyration volume term
#
from gyrPotTools import create_GyrPot
gyr = create_GyrPot("Vgyr",
                "resid 1:181") # selection should exclude disordered tails
potList.append(gyr)
rampedParams.append( MultRamp(.002,1,"gyr.setScale(VALUE)") )

# hbda - distance/angle bb hbond term
#
#protocol.initHBDA('hbda_all.tbl')
#potList.append( XplorPot('HBDA') )

#New torsion angle database potential
#
from torsionDBPotTools import create_TorsionDBPot
torsionDB = create_TorsionDBPot('torsionDB')
potList.append( torsionDB )
rampedParams.append( MultRamp(.002,2,"torsionDB.setScale(VALUE)") )

#
# setup parameters for atom-atom repulsive term. (van der Waals-like term)
#
potList.append( XplorPot('VDW') )
rampedParams.append( StaticRamp("protocol.initNBond()") )
rampedParams.append( MultRamp(0.9,0.8,
                        "command('param nbonds repel VALUE end end')") )
rampedParams.append( MultRamp(.004,4,
                        "command('param nbonds rcon VALUE end end')") )
# nonbonded interaction only between CA atoms
```

```
highTempParams.append( StaticRamp("""protocol.initNBond(cutnb=100,
                                    rcon=0.004,
                                    tolerance=45,
                                    repel=1.2,
                                    onlyCA=1)""") )


potList.append( XplorPot("BOND") )
potList.append( XplorPot("ANGL") )
potList['ANGL'].setThreshold( 5 )
rampedParams.append( MultRamp(0.4,1,"potList['ANGL'].setScale(VALUE)") )
potList.append( XplorPot("IMPR") )
potList['IMPR'].setThreshold( 5 )
rampedParams.append( MultRamp(0.1,1,"potList['IMPR'].setScale(VALUE)") )



# Give atoms uniform weights, except for the anisotropy axis
#
protocol.massSetup()


# IVM setup
#   the IVM is used for performing dynamics and minimization in torsion-angle
#   space, and in Cartesian space.
#
from ivm import IVM
dyn = IVM()

# initially minimize in Cartesian space with only the covalent constraints.
#   Note that bonds, angles and many impropers can't change with the
#   internal torsion-angle dynamics
#   breaks bonds topologically - doesn't change force field
#
#dyn.potList().add( XplorPot("BOND") )
#dyn.potList().add( XplorPot("ANGL") )
#dyn.potList().add( XplorPot("IMPR") )
#
#dyn.breakAllBondsIn("not resname ANI")
#import varTensorTools
#for m in media.values():
#    m.setFreedom("fix")              #fix tensor parameters
#    varTensorTools.topologySetup(dyn,m) #setup tensor topology
#
#protocol.initMinimize(dyn,numSteps=1000)
#dyn.run()
```

```
# reset ivm topology for torsion-angle dynamics
#
dyn.reset()

#for m in media.values():
#   m.setFreedom("fixDa, fixRh")        #fix tensor Rh, Da, vary orientation
#   m.setFreedom("varyDa, varyRh")      #vary tensor Rh, Da, vary orientation
protocol.torsionTopology(dyn)

# minc used for final cartesian minimization
#
minc = IVM()
protocol.initMinimize(minc)

#for m in media.values():
#   m.setFreedom("varyDa, varyRh")    #allow all tensor parameters float here
#   pass
protocol.cartesianTopology(minc)



# object which performs simulated annealing
#
from simulationTools import AnnealIVM
init_t  = 1000.     # Need high temp and slow annealing to converge          ###  DEFAULT IS
3000
cool = AnnealIVM(initTemp =init_t,
                 finalTemp=25,
                 tempStep =12.5,
                 ivm=dyn,
                 rampedParams = rampedParams)

def accept(potList):
   """
   return True if current structure meets acceptance criteria
   """
   if potList['noe'].violations()>0:
      return False
   if potList['rdc'].rms()>1.2: #this might be tightened some
      return False
   if potList['CDIH'].violations()>0:
      return False
   if potList['BOND'].violations()>0:
      return False
   if potList['ANGL'].violations()>0:
```

```
        return False
    if potList['IMPR'].violations()>1:
        return False

    return True

def calcOneStructure(loopInfo):
    """ this function calculates a single structure, performs analysis on the
    structure, and then writes out a pdb file, with remarks.
    """

    # initialize parameters for high temp dynamics.
    InitialParams( rampedParams )
    # high-temp dynamics setup - only need to specify parameters which
    #   differfrom initial values in rampedParams
    InitialParams( highTempParams )

    # high temp dynamics
    #
    protocol.initDynamics(dyn,
                          potList=potList, # potential terms to use
                          bathTemp=init_t,
                          initVelocities=1,
                          finalTime=10,    # stops at 10ps or 5000 steps
                          numSteps=5000,   # whichever comes first
                          printInterval=100)

    dyn.setETolerance( init_t/100 )  #used to det. stepsize. default: t/1000
    dyn.run()

    # initialize parameters for cooling loop
    InitialParams( rampedParams )


    # initialize integrator for simulated annealing
    #
    protocol.initDynamics(dyn,
                          potList=potList,
                          numSteps=100,       #at each temp: 100 steps or
                          finalTime=.2 ,       # .2ps, whichever is less
                          printInterval=100)

    # perform simulated annealing
    #
    cool.run()
```

```
   # final torsion angle minimization
   #
   protocol.initMinimize(dyn,
                         printInterval=50)
   dyn.run()

   # final all- atom minimization
   #
   protocol.initMinimize(minc,
                         potList=potList,
                         dEPred=10)
   minc.run()

   #do analysis and write structure when this function returns
   pass



from simulationTools import StructureLoop, FinalParams
StructureLoop(numStructures=numberOfStructures,
              doWriteStructures=True,
              pdbTemplate=outFilename,
              structLoopAction=calcOneStructure,
              genViolationStats=True,
              averagePotList=potList,
              averageSortPots=[potList['BOND'],potList['ANGL'],potList['IMPR'],
                               noe],
#              averageCrossTerms=refRMSD,
              averageTopFraction=0.1, #report only on best 10% of structs
              averageAccept=accept,   #only use structures which pass accept()
              averageContext=FinalParams(rampedParams),
              averageFilename="SCRIPT_ave.pdb",    #generate regularized ave structure
              averageFitSel="(resid 10:42 or resid 50:81 or resid 90:119) and (name CA or name C or
name N)",
              averageCompSel="(resid 10:42 or resid 50:81 or resid 90:119) and (not resname ANI
and not name H*)"     ).run()
```

HADDOCK

In order to be able to access HADDOCK webserver, you must create an account. Once an account is created, you will have access to the easy interface. You must email HADDOCK to have access for the expert interface (used for protein-protein or protein-ligand docking).

Calculation results are deleted after a week, so must save tar file to access results. PDB files are uploaded in the first and second molecule. Distance restraints (EPR, RDC, etc.) are uploaded under distance restraints → "unambiguous restraints." The table must follow the correct HADDOCK syntax to prevent calculation(s) from crashing. Below is the general syntax for HADDOCK distance restraints:

```
! NEW EPRDEER on July 10, 2020
assign (segid A and resid   26 and name HG  )(segid B and resid    26 and name HG  )    17.0    10.0   10.0
assign (segid A and resid  139 and name HG  )(segid B and resid   139 and name HG  )    57.6    10.0   10.0
                                                                                          A       B      C
```

segid: segment ID ("first molecule" PDB uploaded)
resid: residue number
name: residue atom name (i.e., HA, CA, etc.)

A: predicted distance restraint
B: A + B (error)
C: A – C (error)

References

1. Stryer, L., Molecular basis of visual excitation. *Cold Spring Harb Symp Quant Biol* **1988,** *53 Pt 1*, 283-94.
2. Hoon, M.; Okawa, H.; Della Santina, L.; Wong, R. O., Functional architecture of the retina: development and disease. *Prog Retin Eye Res* **2014,** *42*, 44-84.
3. Baden, T.; Osorio, D., The Retinal Basis of Vertebrate Color Vision. *Annu Rev Vis Sci* **2019,** *5*, 177-200.
4. Ames, J. B.; Tanaka, T.; Stryer, L.; Ikura, M., Portrait of a myristoyl switch protein. *Curr Opin Struct Biol* **1996,** *6* (4), 432-8.
5. Palczewski, K.; Polans, A. S.; Baehr, W.; Ames, J. B., Ca(2+)-binding proteins in the retina: structure, function, and the etiology of human visual diseases. *Bioessays* **2000,** *22* (4), 337-50.
6. Baehr, W.; Palczewski, K., Guanylate cyclase-activating proteins and retina disease. *Subcell Biochem* **2007,** *45*, 71-91.
7. Peshenko, I. V.; Dizhoor, A. M., Activation and inhibition of photoreceptor guanylyl cyclase by guanylyl cyclase activating protein 1 (GCAP-1): the functional role of Mg2+/Ca2+ exchange in EF-hand domains. *J Biol Chem* **2007,** *282* (30), 21645-52.
8. Olshevskaya, E. V.; Peshenko, I. V.; Savchenko, A. B.; Dizhoor, A. M., Retinal guanylyl cyclase isozyme 1 is the preferential in vivo target for constitutively active GCAP1 mutants causing congenital degeneration of photoreceptors. *J Neurosci* **2012,** *32* (21), 7208-17.
9. Ames, J. B.; Ishima, R.; Tanaka, T.; Gordon, J. I.; Stryer, L.; Ikura, M., Molecular mechanics of calcium-myristoyl switches. *Nature* **1997,** *389* (6647), 198-202.
10. Woodruff, M. L.; Janisch, K. M.; Peshenko, I. V.; Dizhoor, A. M.; Tsang, S. H.; Fain, G. L., Modulation of phosphodiesterase6 turnoff during background illumination in mouse rod photoreceptors. *J Neurosci* **2008,** *28* (9), 2064-74.
11. Peshenko, I. V.; Dizhoor, A. M., Guanylyl cyclase-activating proteins (GCAPs) are Ca2+/Mg2+ sensors: implications for photoreceptor guanylyl cyclase (RetGC) regulation in mammalian photoreceptors. *J Biol Chem* **2004,** *279* (17), 16903-6.
12. Peshenko, I. V.; Olshevskaya, E. V.; Yao, S.; Ezzeldin, H. H.; Pittler, S. J.; Dizhoor, A. M., Activation of retinal guanylyl cyclase RetGC1 by GCAP1: stoichiometry of binding and effect of new LCA-related mutations. *Biochemistry* **2010,** *49* (4), 709-17.
13. Ames, J. B.; Lim, S.; Ikura, M., Molecular structure and target recognition of neuronal calcium sensor proteins. *Front Mol Neurosci* **2012,** *5*, 10.
14. Lim, S.; Peshenko, I. V.; Dizhoor, A. M.; Ames, J. B., Structural insights for activation of retinal guanylate cyclase by GCAP1. *PLoS One* **2013,** *8* (11), e81822.
15. Xu, J.; Morris, L.; Thapa, A.; Ma, H.; Michalakis, S.; Biel, M.; Baehr, W.; Peshenko, I. V.; Dizhoor, A. M.; Ding, X. Q., cGMP accumulation causes photoreceptor degeneration in CNG channel deficiency: evidence of cGMP cytotoxicity independently of enhanced CNG channel function. *J Neurosci* **2013,** *33* (37), 14939-48.
16. Ames, J. B.; Porumb, T.; Tanaka, T.; Ikura, M.; Stryer, L., Amino-terminal myristoylation induces cooperative calcium binding to recoverin. *J Biol Chem* **1995,** *270* (9), 4526-33.
17. Ikura, M.; Osawa, M.; Ames, J. B., The role of calcium-binding proteins in the control of transcription: structure to function. *Bioessays* **2002,** *24* (7), 625-36.

18. Osawa, M.; Dace, A.; Tong, K. I.; Valiveti, A.; Ikura, M.; Ames, J. B., Mg2+ and Ca2+ differentially regulate DNA binding and dimerization of DREAM. *J Biol Chem* **2005,** *280* (18), 18008-14.
19. Cook, N. J.; Zeilinger, C.; Koch, K. W.; Kaupp, U. B., Solubilization and functional reconstitution of the cGMP-dependent cation channel from bovine rod outer segments. *J Biol Chem* **1986,** *261* (36), 17033-9.
20. Koch, K. W.; Cook, N. J.; Kaupp, U. B., The cGMP-dependent channel of vertebrate rod photoreceptors exists in two forms of different cGMP sensitivity and pharmacological behavior. *J Biol Chem* **1987,** *262* (30), 14415-21.
21. Kaupp, U. B.; Koch, K. W., Role of cGMP and Ca2+ in vertebrate photoreceptor excitation and adaptation. *Annu Rev Physiol* **1992,** *54*, 153-75.
22. Koch, K. W., Biochemical mechanism of light adaptation in vertebrate photoreceptors. *Trends Biochem Sci* **1992,** *17* (8), 307-11.
23. Koch, K. W., Control of photoreceptor proteins by Ca2+. *Cell Calcium* **1995,** *18* (4), 314-21.
24. Ikura, M.; Kay, L. E.; Bax, A., A novel approach for sequential assignment of 1H, 13C, and 15N spectra of proteins: heteronuclear triple-resonance three-dimensional NMR spectroscopy. Application to calmodulin. *Biochemistry* **1990,** *29* (19), 4659-67.
25. Ikura, M.; Krinks, M.; Torchia, D. A.; Bax, A., An efficient NMR approach for obtaining sequence-specific resonance assignments of larger proteins based on multiple isotopic labeling. *FEBS Lett* **1990,** *266* (1-2), 155-8.
26. Koch, K. W., Purification and identification of photoreceptor guanylate cyclase. *J Biol Chem* **1991,** *266* (13), 8634-7.
27. Arshavsky VYu; Bownds, M. D., Regulation of deactivation of photoreceptor G protein by its target enzyme and cGMP. *Nature* **1992,** *357* (6377), 416-7.
28. Duda, T.; Venkataraman, V.; Jankowska, A.; Lange, C.; Koch, K. W.; Sharma, R. K., Impairment of the rod outer segment membrane guanylate cyclase dimerization in a cone-rod dystrophy results in defective calcium signaling. *Biochemistry* **2000,** *39* (41), 12522-33.
29. Dell'Orco, D.; Koch, K. W., Systems biochemistry approaches to vertebrate phototransduction: towards a molecular understanding of disease. *Biochem Soc Trans* **2010,** *38* (5), 1275-80.
30. Jiang, L.; Baehr, W., GCAP1 mutations associated with autosomal dominant cone dystrophy. *Adv Exp Med Biol* **2010,** *664*, 273-82.
31. Jacobson, S. G.; Cideciyan, A. V.; Peshenko, I. V.; Sumaroka, A.; Olshevskaya, E. V.; Cao, L.; Schwartz, S. B.; Roman, A. J.; Olivares, M. B.; Sadigh, S.; Yau, K. W.; Heon, E.; Stone, E. M.; Dizhoor, A. M., Determining consequences of retinal membrane guanylyl cyclase (RetGC1) deficiency in human Leber congenital amaurosis en route to therapy: residual cone-photoreceptor vision correlates with biochemical properties of the mutants. *Hum Mol Genet* **2013,** *22* (1), 168-83.
32. Duda, T.; Krishnan, A.; Venkataraman, V.; Lange, C.; Koch, K. W.; Sharma, R. K., Mutations in the rod outer segment membrane guanylate cyclase in a cone-rod dystrophy cause defects in calcium signaling. *Biochemistry* **1999,** *38* (42), 13912-9.
33. Hwang, J. Y.; Koch, K. W., Calcium- and myristoyl-dependent properties of guanylate cyclase-activating protein-1 and protein-2. *Biochemistry* **2002,** *41* (43), 13021-8.
34. Hwang, J. Y.; Koch, K. W., The myristoylation of the neuronal Ca2+ -sensors guanylate cyclase-activating protein 1 and 2. *Biochim Biophys Acta* **2002,** *1600* (1-2), 111-7.

35. Koch, K. W., Target recognition of guanylate cyclase by guanylate cyclase-activating proteins. *Adv Exp Med Biol* **2002,** *514*, 349-60.
36. Koch, K. W.; Duda, T.; Sharma, R. K., Photoreceptor specific guanylate cyclases in vertebrate phototransduction. *Mol Cell Biochem* **2002,** *230* (1-2), 97-106.
37. Yap, K. L.; Ames, J. B.; Swindells, M. B.; Ikura, M., Diversity of conformational states and changes within the EF-hand protein superfamily. *Proteins* **1999,** *37* (3), 499-507.
38. Hwang, J. Y.; Schlesinger, R.; Koch, K. W., Calcium-dependent cysteine reactivities in the neuronal calcium sensor guanylate cyclase-activating protein 1. *FEBS Lett* **2001,** *508* (3), 355-9.
39. Gifford, J. L.; Walsh, M. P.; Vogel, H. J., Structures and metal-ion-binding properties of the Ca2+-binding helix-loop-helix EF-hand motifs. *Biochem J* **2007,** *405* (2), 199-221.
40. Lim, S.; Peshenko, I.; Dizhoor, A.; Ames, J. B., Effects of Ca2+, Mg2+, and myristoylation on guanylyl cyclase activating protein 1 structure and stability. *Biochemistry* **2009,** *48* (5), 850-62.
41. Dizhoor, A. M.; Hurley, J. B., Inactivation of EF-hands makes GCAP-2 (p24) a constitutive activator of photoreceptor guanylyl cyclase by preventing a Ca2+-induced "activator-to-inhibitor" transition. *J Biol Chem* **1996,** *271* (32), 19346-50.
42. Lim, S.; Dizhoor, A. M.; Ames, J. B., Structural diversity of neuronal calcium sensor proteins and insights for activation of retinal guanylyl cyclase by GCAP1. *Front Mol Neurosci* **2014,** *7*, 19.
43. Ames, J. B., Dimerization of Neuronal Calcium Sensor Proteins. *Front Mol Neurosci* **2018,** *11*, 397.
44. Peshenko, I. V.; Dizhoor, A. M., Ca2+ and Mg2+ binding properties of GCAP-1. Evidence that Mg2+-bound form is the physiological activator of photoreceptor guanylyl cyclase. *J Biol Chem* **2006,** *281* (33), 23830-41.
45. Peshenko, I. V.; Olshevskaya, E. V.; Dizhoor, A. M., Binding of guanylyl cyclase activating protein 1 (GCAP1) to retinal guanylyl cyclase (RetGC1). The role of individual EF-hands. *J Biol Chem* **2008,** *283* (31), 21747-57.
46. Dizhoor, A. M.; Olshevskaya, E. V.; Peshenko, I. V., Mg2+/Ca2+ cation binding cycle of guanylyl cyclase activating proteins (GCAPs): role in regulation of photoreceptor guanylyl cyclase. *Mol Cell Biochem* **2010,** *334* (1-2), 117-24.
47. Li, C.; Pan, W.; Braunewell, K. H.; Ames, J. B., Structural analysis of Mg2+ and Ca2+ binding, myristoylation, and dimerization of the neuronal calcium sensor and visinin-like protein 1 (VILIP-1). *J Biol Chem* **2011,** *286* (8), 6354-66.
48. Olshevskaya, E. V.; Hughes, R. E.; Hurley, J. B.; Dizhoor, A. M., Calcium binding, but not a calcium-myristoyl switch, controls the ability of guanylyl cyclase-activating protein GCAP-2 to regulate photoreceptor guanylyl cyclase. *J Biol Chem* **1997,** *272* (22), 14327-33.
49. Hughes, R. E.; Brzovic, P. S.; Dizhoor, A. M.; Klevit, R. E.; Hurley, J. B., Ca2+-dependent conformational changes in bovine GCAP-2. *Protein Sci* **1998,** *7* (12), 2675-80.
50. Burgoyne, R. D., Neuronal calcium sensor proteins: generating diversity in neuronal Ca2+ signalling. *Nat Rev Neurosci* **2007,** *8* (3), 182-93.
51. Hwang, J. Y.; Schlesinger, R.; Koch, K. W., Irregular dimerization of guanylate cyclase-activating protein 1 mutants causes loss of target activation. *Eur J Biochem* **2004,** *271* (18), 3785-93.

52. Sulmann, S.; Vocke, F.; Scholten, A.; Koch, K. W., Retina specific GCAPs in zebrafish acquire functional selectivity in Ca2+-sensing by myristoylation and Mg2+-binding. *Sci Rep* **2015,** *5*, 11228.
53. Lim, S.; Peshenko, I. V.; Olshevskaya, E. V.; Dizhoor, A. M.; Ames, J. B., Structure of Guanylyl Cyclase Activator Protein 1 (GCAP1) Mutant V77E in a Ca2+-free/Mg2+-bound Activator State. *J Biol Chem* **2016,** *291* (9), 4429-41.
54. Peshenko, I. V.; Olshevskaya, E. V.; Lim, S.; Ames, J. B.; Dizhoor, A. M., Identification of target binding site in photoreceptor guanylyl cyclase-activating protein 1 (GCAP1). *J Biol Chem* **2014,** *289* (14), 10140-54.
55. Peshenko, I. V.; Olshevskaya, E. V.; Dizhoor, A. M., Dimerization Domain of Retinal Membrane Guanylyl Cyclase 1 (RetGC1) Is an Essential Part of Guanylyl Cyclase-activating Protein (GCAP) Binding Interface. *J Biol Chem* **2015,** *290* (32), 19584-96.
56. Peshenko, I. V.; Olshevskaya, E. V.; Dizhoor, A. M., Evaluating the role of retinal membrane guanylyl cyclase 1 (RetGC1) domains in binding guanylyl cyclase-activating proteins (GCAPs). *J Biol Chem* **2015,** *290* (11), 6913-24.
57. Dell'Orco, D.; Behnen, P.; Linse, S.; Koch, K. W., Calcium binding, structural stability and guanylate cyclase activation in GCAP1 variants associated with human cone dystrophy. *Cell Mol Life Sci* **2010,** *67* (6), 973-84.
58. Dizhoor, A. M.; Chen, C. K.; Olshevskaya, E.; Sinelnikova, V. V.; Phillipov, P.; Hurley, J. B., Role of the acylated amino terminus of recoverin in Ca(2+)-dependent membrane interaction. *Science* **1993,** *259* (5096), 829-32.
59. Stephen, R.; Bereta, G.; Golczak, M.; Palczewski, K.; Sousa, M. C., Stabilizing function for myristoyl group revealed by the crystal structure of a neuronal calcium sensor, guanylate cyclase-activating protein 1. *Structure* **2007,** *15* (11), 1392-402.
60. Payne, A. M.; Downes, S. M.; Bessant, D. A.; Taylor, R.; Holder, G. E.; Warren, M. J.; Bird, A. C.; Bhattacharya, S. S., A mutation in guanylate cyclase activator 1A (GUCA1A) in an autosomal dominant cone dystrophy pedigree mapping to a new locus on chromosome 6p21.1. *Hum Mol Genet* **1998,** *7* (2), 273-7.
61. Lim, S.; Peshenko, I. V.; Dizhoor, A. M.; Ames, J. B., Backbone (1)H, (13)C, and (15)N resonance assignments of guanylyl cyclase activating protein-1, GCAP1. *Biomol NMR Assign* **2013,** *7* (1), 39-42.
62. Lim, S.; Roseman, G.; Peshenko, I.; Manchala, G.; Cudia, D.; Dizhoor, A. M.; Millhauser, G.; Ames, J. B., Retinal guanylyl cyclase activating protein 1 forms a functional dimer. *PLoS One* **2018,** *13* (3), e0193947.
63. Peshenko, I. V.; Olshevskaya, E. V.; Azadi, S.; Molday, L. L.; Molday, R. S.; Dizhoor, A. M., Retinal degeneration 3 (RD3) protein inhibits catalytic activity of retinal membrane guanylyl cyclase (RetGC) and its stimulation by activating proteins. *Biochemistry* **2011,** *50* (44), 9511-9.
64. Azadi, S., RD3: a challenge and a promise. *JSM Biotechnol Biomed Eng* **2013,** *1* (3).
65. Aravindan, S.; Somasundaram, D. B.; Kam, K. L.; Subramanian, K.; Yu, Z.; Herman, T. S.; Fung, K. M.; Aravindan, N., Retinal Degeneration Protein 3 (RD3) in normal human tissues: Novel insights. *Sci Rep* **2017,** *7* (1), 13154.
66. Chang, B.; Hawes, N. L.; Hurd, R. E.; Davisson, M. T.; Nusinowitz, S.; Heckenlively, J. R., Retinal degeneration mutants in the mouse. *Vision Res* **2002,** *42* (4), 517-25.

67. Azadi, S.; Molday, L. L.; Molday, R. S., RD3, the protein associated with Leber congenital amaurosis type 12, is required for guanylate cyclase trafficking in photoreceptor cells. *Proc Natl Acad Sci U S A* **2010,** *107* (49), 21158-63.
68. Molday, L. L.; Djajadi, H.; Yan, P.; Szczygiel, L.; Boye, S. L.; Chiodo, V. A.; Gregory-Evans, K.; Sarunic, M. V.; Hauswirth, W. W.; Molday, R. S., RD3 gene delivery restores guanylate cyclase localization and rescues photoreceptors in the Rd3 mouse model of Leber congenital amaurosis 12. *Hum Mol Genet* **2013,** *22* (19), 3894-905.
69. Sokal, I.; Li, N.; Surgucheva, I.; Warren, M. J.; Payne, A. M.; Bhattacharya, S. S.; Baehr, W.; Palczewski, K., GCAP1 (Y99C) mutant is constitutively active in autosomal dominant cone dystrophy. *Mol Cell* **1998,** *2* (1), 129-33.
70. Duda, T.; Venkataraman, V.; Goraczniak, R.; Lange, C.; Koch, K. W.; Sharma, R. K., Functional consequences of a rod outer segment membrane guanylate cyclase (ROS-GC1) gene mutation linked with Leber's congenital amaurosis. *Biochemistry* **1999,** *38* (2), 509-15.
71. Friedman, J. S.; Chang, B.; Kannabiran, C.; Chakarova, C.; Singh, H. P.; Jalali, S.; Hawes, N. L.; Branham, K.; Othman, M.; Filippova, E.; Thompson, D. A.; Webster, A. R.; Andréasson, S.; Jacobson, S. G.; Bhattacharya, S. S.; Heckenlively, J. R.; Swaroop, A., Premature truncation of a novel protein, RD3, exhibiting subnuclear localization is associated with retinal degeneration. *Am J Hum Genet* **2006,** *79* (6), 1059-70.
72. Olshevskaya, E. V.; Calvert, P. D.; Woodruff, M. L.; Peshenko, I. V.; Savchenko, A. B.; Makino, C. L.; Ho, Y. S.; Fain, G. L.; Dizhoor, A. M., The Y99C mutation in guanylyl cyclase-activating protein 1 increases intracellular Ca2+ and causes photoreceptor degeneration in transgenic mice. *J Neurosci* **2004,** *24* (27), 6078-85.
73. Zulliger, R.; Naash, M. I.; Rajala, R. V.; Molday, R. S.; Azadi, S., Impaired association of retinal degeneration-3 with guanylate cyclase-1 and guanylate cyclase-activating protein-1 leads to leber congenital amaurosis-1. *J Biol Chem* **2015,** *290* (6), 3488-99.
74. Peshenko, I. V.; Olshevskaya, E. V.; Dizhoor, A. M., Functional Study and Mapping Sites for Interaction with the Target Enzyme in Retinal Degeneration 3 (RD3) Protein. *J Biol Chem* **2016,** *291* (37), 19713-23.
75. Peshenko, I. V.; Yu, Q.; Lim, S.; Cudia, D.; Dizhoor, A. M.; Ames, J. B., Retinal degeneration 3 (RD3) protein, a retinal guanylyl cyclase regulator, forms a monomeric and elongated four-helix bundle. *J Biol Chem* **2019,** *294* (7), 2318-2328.
76. Chang, B., Mouse Models as Tools to Identify Genetic Pathways for Retinal Degeneration, as Exemplified by Leber's Congenital Amaurosis. *Methods Mol Biol* **2016,** *1438*, 417-30.
77. Peshenko, I. V.; Olshevskaya, E. V.; Dizhoor, A. M., mutations in retinal guanylyl cyclase 1 provide biochemical reasons for dominant cone-rod dystrophy but not for stationary night blindness. *J Biol Chem* **2020,** *295* (52), 18301-18315.
78. Plana-Bonamaisó, A.; López-Begines, S.; Andilla, J.; Fidalgo, M. J.; Loza-Alvarez, P.; Estanyol, J. M.; Villa, P.; Méndez, A., GCAP neuronal calcium sensor proteins mediate photoreceptor cell death in the rd3 mouse model of LCA12 congenital blindness by involving endoplasmic reticulum stress. *Cell Death Dis* **2020,** *11* (1), 62.
79. Dizhoor, A. M.; Olshevskaya, E. V.; Peshenko, I. V., The R838S Mutation in Retinal Guanylyl Cyclase 1 (RetGC1) Alters Calcium Sensitivity of cGMP Synthesis in the Retina and Causes Blindness in Transgenic Mice. *J Biol Chem* **2016,** *291* (47), 24504-24516.

80. Baehr, W.; Karan, S.; Maeda, T.; Luo, D. G.; Li, S.; Bronson, J. D.; Watt, C. B.; Yau, K. W.; Frederick, J. M.; Palczewski, K., The function of guanylate cyclase 1 and guanylate cyclase 2 in rod and cone photoreceptors. *J Biol Chem* **2007,** *282* (12), 8837-47.
81. Nishiguchi, K. M.; Sokal, I.; Yang, L.; Roychowdhury, N.; Palczewski, K.; Berson, E. L.; Dryja, T. P.; Baehr, W., A novel mutation (I143NT) in guanylate cyclase-activating protein 1 (GCAP1) associated with autosomal dominant cone degeneration. *Invest Ophthalmol Vis Sci* **2004,** *45* (11), 3863-70.
82. Wilkie, S. E.; Li, Y.; Deery, E. C.; Newbold, R. J.; Garibaldi, D.; Bateman, J. B.; Zhang, H.; Lin, W.; Zack, D. J.; Bhattacharya, S. S.; Warren, M. J.; Hunt, D. M.; Zhang, K., Identification and functional consequences of a new mutation (E155G) in the gene for GCAP1 that causes autosomal dominant cone dystrophy. *Am J Hum Genet* **2001,** *69* (3), 471-80.
83. Sokal, I.; Dupps, W. J.; Grassi, M. A.; Brown, J.; Affatigato, L. M.; Roychowdhury, N.; Yang, L.; Filipek, S.; Palczewski, K.; Stone, E. M.; Baehr, W., A novel GCAP1 missense mutation (L151F) in a large family with autosomal dominant cone-rod dystrophy (adCORD). *Invest Ophthalmol Vis Sci* **2005,** *46* (4), 1124-32.
84. Peshenko, I. V.; Moiseyev, G. P.; Olshevskaya, E. V.; Dizhoor, A. M., Factors that determine Ca2+ sensitivity of photoreceptor guanylyl cyclase. Kinetic analysis of the interaction between the Ca2+-bound and the Ca2+-free guanylyl cyclase activating proteins (GCAPs) and recombinant photoreceptor guanylyl cyclase 1 (RetGC-1). *Biochemistry* **2004,** *43* (43), 13796-804.
85. Dizhoor, A. M.; Boikov, S. G.; Olshevskaya, E. V., Constitutive activation of photoreceptor guanylate cyclase by Y99C mutant of GCAP-1. Possible role in causing human autosomal dominant cone degeneration. *J Biol Chem* **1998,** *273* (28), 17311-4.
86. Lim, S.; Cudia, D.; Yu, Q.; Peshenko, I.; Dizhoor, A. M.; Ames, J. B., Chemical shift assignments of retinal degeneration 3 protein (RD3). *Biomol NMR Assign* **2018,** *12* (1), 167-170.
87. Fu, Y.; Yau, K. W., Phototransduction in mouse rods and cones. *Pflugers Arch* **2007,** *454* (5), 805-19.
88. Lim, S.; Scholten, A.; Manchala, G.; Cudia, D.; Zlomke-Sell, S. K.; Koch, K. W.; Ames, J. B., Structural Characterization of Ferrous Ion Binding to Retinal Guanylate Cyclase Activator Protein 5 from Zebrafish Photoreceptors. *Biochemistry* **2017,** *56* (51), 6652-6661.
89. Delaglio, F.; Grzesiek, S.; Vuister, G. W.; Zhu, G.; Pfeifer, J.; Bax, A., NMRPipe: a multidimensional spectral processing system based on UNIX pipes. *J Biomol NMR* **1995,** *6* (3), 277-93.
90. Mutoh, R.; Muraki, N.; Shinmura, K.; Kubota-Kawai, H.; Lee, Y. H.; Nowaczyk, M. M.; Rögner, M.; Hase, T.; Ikegami, T.; Kurisu, G., X-ray Structure and Nuclear Magnetic Resonance Analysis of the Interaction Sites of the Ga-Substituted Cyanobacterial Ferredoxin. *Biochemistry* **2015,** *54* (39), 6052-61.
91. Shen, Y.; Delaglio, F.; Cornilescu, G.; Bax, A., TALOS+: a hybrid method for predicting protein backbone torsion angles from NMR chemical shifts. *J Biomol NMR* **2009,** *44* (4), 213-23.
92. Palczewski, K.; Jäger, S.; Buczyłko, J.; Crouch, R. K.; Bredberg, D. L.; Hofmann, K. P.; Asson-Batres, M. A.; Saari, J. C., Rod outer segment retinol dehydrogenase: substrate specificity and role in phototransduction. *Biochemistry* **1994,** *33* (46), 13741-50.
93. Imanishi, Y.; Yang, L.; Sokal, I.; Filipek, S.; Palczewski, K.; Baehr, W., Diversity of guanylate cyclase-activating proteins (GCAPs) in teleost fish: characterization of three novel

GCAPs (GCAP4, GCAP5, GCAP7) from zebrafish (Danio rerio) and prediction of eight GCAPs (GCAP1-8) in pufferfish (Fugu rubripes). *J Mol Evol* **2004,** *59* (2), 204-217.
94. Fries, R.; Scholten, A.; Säftel, W.; Koch, K. W., Operation profile of zebrafish guanylate cyclase-activating protein 3. *J Neurochem* **2012,** *121* (1), 54-65.
95. Koch, K. W., The guanylate cyclase signaling system in zebrafish photoreceptors. *FEBS Lett* **2013,** *587* (13), 2055-9.
96. Scholten, A.; Koch, K. W., Differential calcium signaling by cone specific guanylate cyclase-activating proteins from the zebrafish retina. *PLoS One* **2011,** *6* (8), e23117.
97. Crack, J. C.; Green, J.; Thomson, A. J.; Le Brun, N. E., Iron-sulfur clusters as biological sensors: the chemistry of reactions with molecular oxygen and nitric oxide. *Acc Chem Res* **2014,** *47* (10), 3196-205.
98. Min, T.; Ergenekan, C. E.; Eidsness, M. K.; Ichiye, T.; Kang, C., Leucine 41 is a gate for water entry in the reduction of Clostridium pasteurianum rubredoxin. *Protein Sci* **2001,** *10* (3), 613-21.
99. Sterling, J.; Guttha, S.; Song, Y.; Song, D.; Hadziahmetovic, M.; Dunaief, J. L., Iron importers Zip8 and Zip14 are expressed in retina and regulated by retinal iron levels. *Exp Eye Res* **2017,** *155*, 15-23.
100. Cudia, D.; Ames, J. B., Chemical shift assignments of retinal guanylyl cyclase activating protein 5 (GCAP5). *Biomol NMR Assign* **2019,** *13* (1), 201-205.
101. Cudia, D.; Roseman, G. P.; Assafa, T. E.; Scholten, A.; Zlomke-Sell, S.-K.; Yamada, H.; Koch, K.-W.; Milhauser, G.; Ames, J. B., NMR and EPR-DEER Structure of a Dimeric Guanylate Cyclase Activator Protein-5 from Zebrafish Photoreceptors. *Biochemistry* **2021, submitted**.
102. Wiseman, T.; Williston, S.; Brandts, J. F.; Lin, L. N., Rapid measurement of binding constants and heats of binding using a new titration calorimeter. *Anal Biochem* **1989,** *179* (1), 131-7.
103. Tjandra, N.; Bax, A., Direct measurement of distances and angles in biomolecules by NMR in a dilute liquid crystalline medium. *Science* **1997,** *278* (5340), 1111-4.
104. Ottiger, M.; Delaglio, F.; Bax, A., Measurement of J and dipolar couplings from simplified two-dimensional NMR spectra. *J Magn Reson* **1998,** *131* (2), 373-8.
105. Zweckstetter, M., NMR: prediction of molecular alignment from structure using the PALES software. *Nat Protoc* **2008,** *3* (4), 679-90.
106. Lee, W.; Tonelli, M.; Markley, J. L., NMRFAM-SPARKY: enhanced software for biomolecular NMR spectroscopy. *Bioinformatics* **2015,** *31* (8), 1325-7.
107. Bax, A.; Ikura, M., An efficient 3D NMR technique for correlating the proton and 15N backbone amide resonances with the alpha-carbon of the preceding residue in uniformly 15N/13C enriched proteins. *J Biomol NMR* **1991,** *1* (1), 99-104.
108. Bax, A.; Ikura, M.; Kay, L. E.; Barbato, G.; Spera, S., Multidimensional triple resonance NMR spectroscopy of isotopically uniformly enriched proteins: a powerful new strategy for structure determination. *Ciba Found Symp* **1991,** *161*, 108-19; discussion 119-35.
109. Ikura, M.; Kay, L. E.; Bax, A., Improved three-dimensional 1H-13C-1H correlation spectroscopy of a 13C-labeled protein using constant-time evolution. *J Biomol NMR* **1991,** *1* (3), 299-304.
110. Shen, Y.; Bax, A., Protein structural information derived from NMR chemical shift with the neural network program TALOS-N. *Methods Mol Biol* **2015,** *1260*, 17-32.

111. Schwieters, C. D.; Kuszewski, J. J.; Tjandra, N.; Clore, G. M., The Xplor-NIH NMR molecular structure determination package. *J Magn Reson* **2003,** *160* (1), 65-73.
112. Chen, V. B.; Arendall, W. B.; Headd, J. J.; Keedy, D. A.; Immormino, R. M.; Kapral, G. J.; Murray, L. W.; Richardson, J. S.; Richardson, D. C., MolProbity: all-atom structure validation for macromolecular crystallography. *Acta Crystallogr D Biol Crystallogr* **2010,** *66* (Pt 1), 12-21.
113. van Zundert, G. C. P.; Rodrigues, J. P. G. L.; Trellet, M.; Schmitz, C.; Kastritis, P. L.; Karaca, E.; Melquiond, A. S. J.; van Dijk, M.; de Vries, S. J.; Bonvin, A. M. J. J., The HADDOCK2.2 Web Server: User-Friendly Integrative Modeling of Biomolecular Complexes. *J Mol Biol* **2016,** *428* (4), 720-725.
114. Meyer, M.; Morgenstern, B., Characterization of gelatine and acid soluble collagen by size exclusion chromatography coupled with multi angle light scattering (SEC-MALS). *Biomacromolecules* **2003,** *4* (6), 1727-32.
115. Wyatt, P. J., Combined differential light scattering with various liquid chromatography separation techniques. *Biochem Soc Trans* **1991,** *19* (2), 485.
116. Huang, Q.; Hong, X.; Hao, Q., SNAP-25 is also an iron-sulfur protein. *FEBS Lett* **2008,** *582* (10), 1431-6.
117. deMaré, F.; Kurtz, D. M.; Nordlund, P., The structure of Desulfovibrio vulgaris rubrerythrin reveals a unique combination of rubredoxin-like FeS4 and ferritin-like diiron domains. *Nat Struct Biol* **1996,** *3* (6), 539-46.
118. Tang, Q.; Liu, Y. P.; Yan, X. X.; Liang, D. C., Structural and functional characterization of Cys4 zinc finger motif in the recombination mediator protein RecR. *DNA Repair (Amst)* **2014,** *24*, 10-14.
119. Redenti, S.; Ripps, H.; Chappell, R. L., Zinc release at the synaptic terminals of rod photoreceptors. *Exp Eye Res* **2007,** *85* (4), 580-4.
120. Ramamurthy, V.; Tucker, C.; Wilkie, S. E.; Daggett, V.; Hunt, D. M.; Hurley, J. B., Interactions within the coiled-coil domain of RetGC-1 guanylyl cyclase are optimized for regulation rather than for high affinity. *J Biol Chem* **2001,** *276* (28), 26218-29.
121. Liu, Y.; Ruoho, A. E.; Rao, V. D.; Hurley, J. H., Catalytic mechanism of the adenylyl and guanylyl cyclases: modeling and mutational analysis. *Proc Natl Acad Sci U S A* **1997,** *94* (25), 13414-9.
122. Abbas, S.; Marino, V.; Weisschuh, N.; Kieninger, S.; Solaki, M.; Dell'Orco, D.; Koch, K. W., Neuronal Calcium Sensor GCAP1 Encoded by. *ACS Chem Neurosci* **2020,** *11* (10), 1458-1470.
123. Ferrari, S.; Di Iorio, E.; Barbaro, V.; Ponzin, D.; Sorrentino, F. S.; Parmeggiani, F., Retinitis pigmentosa: genes and disease mechanisms. *Curr Genomics* **2011,** *12* (4), 238-49.
124. Peshenko, I. V.; Olshevskaya, E. V.; Dizhoor, A. M., Interaction of GCAP1 with retinal guanylyl cyclase and calcium: sensitivity to fatty acylation. *Front Mol Neurosci* **2012,** *5*, 19.